UNIVERSITY OF CALIFORNIA, SAN DIEGO

Biomechanics and Cortical Representation of Whisking in the
Rat Vibrissa System

A dissertation submitted in partial satisfaction of the requirements for the
degree Doctor of Philosophy
in
Neurosciences, Specialization in Computational Neuroscience

by

Daniel Nicholas Hill

Committee in charge:

Professor Emo Todorov, Chair
Professor Dan E. Feldman
Professor Harvey J. Karten
Professor David Kleinfeld
Professor Richard J. Krauzlis

2009

The Dissertation of Daniel N. Hill is approved, and it is acceptable in quality and form for publication on microfilm:

_____

_____

_____

_____

_____

Chair

University of California, San Diego

2009

Table of Contents

List of Figures

List of Tables

Acknowledgements

The material of Chapter 2 is a manuscript that is currently under preparation for submission and will include David Kleinfeld as second author. Part of this dissertation follows from work that is currently published in:

Hill DN, Bermejo R, Zeigler HP, Kleinfeld D. Biomechanics of the vibrissa motor plant in rat: Rhythmic whisking consists of triphasic neuromuscular activity. J Neurosci. 28(13):3438-55 (2008)

This material is included in Chapter 3 with the generous consent of all coauthors and permission of the journal. The content of chapter 4 is a manuscript that is currently under preparation for submission and will include John C. Curtis and David Kleinfeld as authors.

Vita

2001-2002	Research Assistant, Dr. Garrett Kenyon, Los Alamos National Laboratory
2002	B.S. Computer Science, Rochester Institute of Technology
2002-2005	NSF / IGERT Predoctoral Fellow
2003.2009	Research Assistant, Prof. David Kleinfeld, Department of Physics, University of California, San Diego
2006-2008	NIH / NRSA Predoctoral Fellow
2008	M.S., Electrical and Computer Engineering, University of California, San Diego
2009	Ph.D., Neurosciences, Computational Neuroscience Training Program, University of California, San Diego

Publications

Wolfe J, Hill DN, Pahlavan S, Drew PJ, Kleinfeld D, Feldman DE. Texture coding in the rat whisker system: slip-stick versus differential encoding. PLOS Biology. 6(8):1661-1677. (2008)

Hill DN, Bermejo R, Zeigler HP, Kleinfeld D. Biomechanics of the vibrissa motor plant in rat: Rhythmic whisking consists of triphasic neuromuscular activity. J Neurosci. 28(13):3438-55 (2008)

Hill DN, Kleinfeld D, Mehta SB. Spike Sorting. In Observed Brain Dynamics by P. P.Mitra and H. Bokil, Oxford Press. (2007)

Kenyon GT, Hill D, Theiler J, George JS, Marshak DW. A Theory Of The Benham Top Based On Center-Surround Interactions In The Parvocellular Pathway. Neural Networks. 17: 773.786. (2004)

Presentations

The cortical representation of muscle activation in the control of whisking. Barrels XXI, Baltimore, MD (2008)

Triphasic neuromuscular control of whisking. Functional Organization of Barrel Cortex Networks. Alicante, Spain (2008)

Biomechanics, behavior, and encoding in the rat vibrissa system. COSYNE, Park City, UT (2007)

Biomechanics of whisking: whisking consists of 3 phases of muscle activity. Barrels XIX, Atlanta, GA (2006)

Electromyography and kinematics of whisking: a preliminary analysis. Barrels XVII, San Diego, CA (2004)

ABSTRACT OF THE DISSERTATION

Biomechanics and Cortical Representation of Whisking in the

Rat Vibrissa System

by

Daniel Nicholas Hill

Doctor of Philosophy in Neurosciences,

Specialization in Computational Neuroscience

University of California, San Diego, 2009

Professor Emo Todorov, Chair

Sensory organs are not stationary in the world, and thus sensation can reflect motion of the organism equally as well as stimuli from the environment. Nervous systems must integrate signals of external and internal origin to disentangle a sense of self out of the total sensory input. To examine the representation of self-motion in the nervous system, we use rhythmic whisking behavior in the rat vibrissa system as a model for active sensing. First, we characterize the motor plant underlying this behavior through recordings of behavior and muscle activity. These data inform a biomechanical model that establishes the motor plant for whisking and its

physical constraints. Having thus defined the control problem of whisking behavior, we investigate its representation in the vibrissa region of primary motor cortex. We found that single units recorded in the behaving animal accurately represent the rhythmic component of the whisk cycle and that small populations of units accurately encode the amplitude and offset position of individual sweeps of the vibrissae. Finally, we compared this data to recordings in the vibrissa region of primary somatosensory cortex. We find that sensory cortex more reliably encodes the rhythmic component of whisking while motor cortex more reliably encodes slower kinetic parameters. These data are consistent with a model that sensory cortex encodes vibrissa position in a normalized coordinate system with the transformation into absolute coordinates requiring a motor copy signal. More generally, our results bear on what may likely be a more general segregation of representation within the nervous system.

Chapter 1 – Introduction

Biological sensors are typically subject to motor control by the organism. This ability allows for what is called *active sensing* where the animal uses behavioral strategies to acquire sensory information. Despite this advantage, moving sensors can also be problematic in that interpretation of the sensory signal is dependent on the motion of the sensor, which itself may be hard to disentangle from stimuli that arises from the external world. Theses issues are of general interest to neuroscience, yet little is understood about how sensory and motor signals interact in the mammalian nervous system.

Before investigating neural processing in a sensorimotor system, it is important to distinguish between different sensory and motor signals and their relation to intrinsic and extrinsic sources. The terminology of (von Holst, 1954) provides a useful vocabulary for discussing these signals (Fig. 1.1). *Afference* is a term for the general sensory input into the nervous system. It can be further subdivided into *ex-afference,* which is sensory input related to the external world, and *re*-afference, which is sensory input derived from the animal itself. Re-afferent signaling is said to be *proprioceptive* when the sensor specifically monitors the state of the animal, such as with muscle

spindles and golgi tendon organs. However, primary sensory neurons may not distinguish ex-afferent and re-afferent sources, and so may be intermixed. The general term for a motor command is *efference.* Motor commands must ultimately act on motor neurons to activate musculature, but the nervous system may also retain an internal representation of its motor command, termed *efference copy*. Note that efference copy and re-afferent signals may contain the same information though one is derived centrally and the other peripherally. Thus, the major perceptual issue in active sensing is how do organisms use efferent copy and re-afference to interpret ex-afferent signals? The major motor control issue is how does an organism use afferent signals to inform efference, or motor decisions, in sensory acquisition behaviors.

In the following dissertation, we use the rat vibrissa system to explore these questions. Rats use an array of pliable hairs on either side of their snout to explore their world. These vibrissae sweep back and forth rhythmically in a behavior called rhythmic whisking. This behavior offers an ideal model for the study of active sensing. The behavior has a single degree of freedom as motion of the vibrissae is largely bilaterally symmetric and restricted to the anterior-posterior axis of the animal (Bermejo et al., 2005). The behavioral repertoire of whisking is well characterized (Knutsen et al., 2008) and now we have a well-defined set of mechanical constraints on the motor plant that generates whisking (Hill et al., 2008). Anatomically, the

system is composed of a hierarchy of sensory-motor loops (Kleinfeld et al., 1999) that allow the investigation of sensory-motor transformations at many levels of neural processing. The muscles involved in rhythmic whisking lack spindles so that there is a single source of sensory feedback into the system via the infra-orbital branch of the trigeminal nerve (Rice and Arvidsson, 1991). There exist several whisking behavioral paradigms in rodents (Knutsen et al., 2006b; Mehta et al., 2007; Curtis and Kleinfeld, 2009) that are compatible with advanced opto-genetic physiology in awake, behaving animals (Aronoff and Petersen, 2006).

In the present thesis, we begin in chapter 2 with a review of the literature on the motor system that underlies rhythmic whisking behavior. In chapter 3, we present data that define the motor plant of whisking, *i.e.*, the muscles and elastic properties of the face that biomechanically constrain motor control. And finally, in chapter 4 we present electrophysiological data from the vibrissa region of primary motor cortex (vM1) that detail the fidelity with which vibrissa motion is encoded in single unit spike trains. Taken together, our findings grant insight into how organisms represent and control interacting sensory and motor processes.

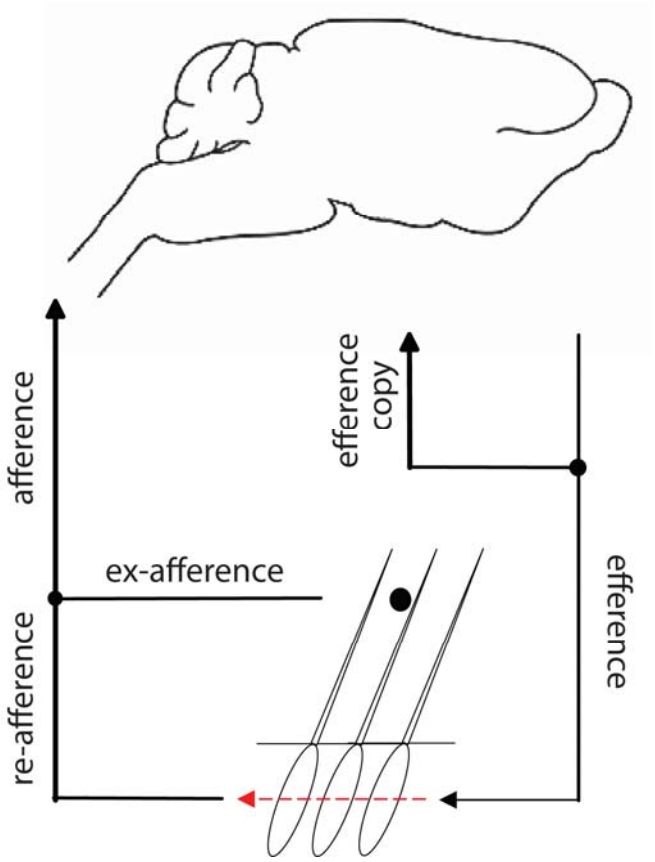

Figure 1.1: Cartoon of sensory and motor signals in rat vibrissa system.
Dashed red line emphasizes that in efferent re-afferent signals are derived from efferent signals through the motor plant. Black dot represents object in external world giving rise ex-afferent signal. Terminology is from (von Holst 1954).

Chapter 2 – Motor control in the rat vibrissa system

Much attention is given to sensory processing in the rat vibrissa system due in large part to the simplistic anatomical organization of barrel cortex where individual vibrissae are represented in a discrete somatotopic map. Less work has gone toward elucidating the motor pathways. This review focuses in on the most well-studied components of the motor system, namely the motor apparatus itself and the vibrissa region of primary motor cortex (vM1).

2.1 The motor plant for whisking

The vibrissae and their follicles define the sensorimotor problem for the animal. The vibrissae are arranged in a grid of approximately 30 hairs on either side of the face. Individual vibrissae are associated with *intrinsic* muscles that wrap around the base of each follicle. In contrast, a set of broad *extrinsic* muscles invades the mystacial pad as a whole (Dorfl, 1982; Wineski, 1985)(Fig. 2.1). The intrinsic and extrinsic muscles are innervated by the lateral and dorsal aspects of the facial nucleus, respectively (Klein and Rhoades, 1985). Muscles spindles have not been observed in the mystacial pad, so it is thought the principle source of re-afferent information is through

the tactile innervation of the follicles via the trigeminal nerve (Rice and Arvidsson, 1991). Consistently, electrophysiological studies of the trigeminal ganglion show that primary sensory neurons exhibit both re-afferent and ex-afferent signaling (Szwed et al., 2003b) (Leiser and Moxon, 2007; Khatri et al., 2009).

Behaviorally, rhythmic whisking can be described by a single degree of freedom as whisking is for the most part bilaterally symmetric motion along the anterior-posterior axis (Gao et al., 2001). The dorsal-ventral component of whisking is marginal (Bermejo et al., 2002), motion of the mystacial pad (Bermejo et al., 2005) and axial rotation (Knutsen et al., 2008) are coherent with the vibrissae, and divergent movement of vibrissae is only reported rarely (Sachdev et al., 2002). There are some asymmetric whisking behaviors associated with head movements (Towal and Hartmann, 2006) and contact with an object (Mitchinson et al., 2007), and the angle between adjacent vibrissae, *i.e.,* the spread, varies in a task-dependent manner (Grant et al., 2009). The frequency, amplitude, and offset of whisking trajectories extend over a wide range of values, though the whisking frequency maintains nearly perfect regularity over the course of a few seconds (Berg and Kleinfeld, 2003c). Finally, the precision of motor control is apparently limited to about a degree of resolution as this is the amplitude of a high-frequency tremor that vibrissae exhibit spontaneously in air (Wolfe et al., 2008). The

amplitude of this motion is consistent with shot-noise from individual muscle action potentials (Cramer and Keller, 2006a; Herfst and Brecht, 2008), and the high-frequency jitter is at least partially coherent with muscle activity (Wolfe et al., 2008).

2.2 Anatomical connections with motor cortex

One feature of vM1 that suggests its importance in sensorimotor integration is its highly organized, reciprocal connectivity with the vibrissa representation in ipsilateral S1, or barrel cortex (Fig. 2.1). Remarkably, this circuit can be maintained in a cortical slice experiment (Rocco and Brumberg, 2007).

Barrel cortex projects from layers 2/3, 5, and 6 to all layers of vM1 (Zhang and Deschenes, 1997; Hoffer et al., 2003; Alloway et al., 2004). The projections from the representation in S1 of a specific vibrissa project to an area of vM1 that evokes movement from that same vibrissa when electrically stimulated (Izraeli and Porter, 1995a). These connections originate preferentially from the septal columns of barrel cortex. Significantly, the septal columns receive input from posterior medial thalamus (PoM) which is hypothesized to relay re-afferent input from the follicles (Ahissar et al., 2000)

although this claim has been disputed (Masri et al., 2008) The reciprocal connections from vM1 to S1 originate in layer 5 and project to layer 5 of barrel columns and layers 1 and 5 in septal columns (Miyashita et al., 1994b; Veinante and Deschenes, 2003; Rocco and Brumberg, 2007).

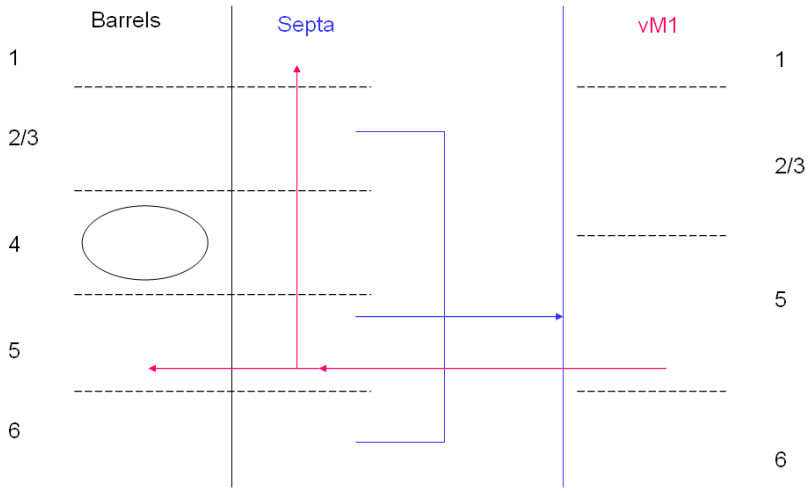

Figure 2.1 Schematic of layer-specific interconnectivity of S1 and ipsilateral vM1. Sources given in text.

The list of brain regions that have connectivity with vM1 is quite extensive (Hattox et al., 2002) (Fig. 2.2), and here we highlight only a few observations from the recent literature. Projections from S2 to vM1 are more extensive than vM1, so that the important sensorimotor interactions in cortex potentially do not take place in S1 (Izraeli and Porter, 1995a). The motor neurons of the facial nucleus that control the intrinsic muscles receive direct input from vM1. This situation is extremely rare outside of the motor neurons

that control primate hand movements(Grinevich et al., 2005) and suggests a highly specialized role for cortical control of vibrissa movement. Lastly, motor cortex projects to recurrent inhibitory neurons in Zona Incerta, causing a disinhibition of POm when vM1 is electrically excited (Urbain and Deschenes, 2007b). This result is consistent with the hypothesis that POm in relays re-afferent signals to cortex.

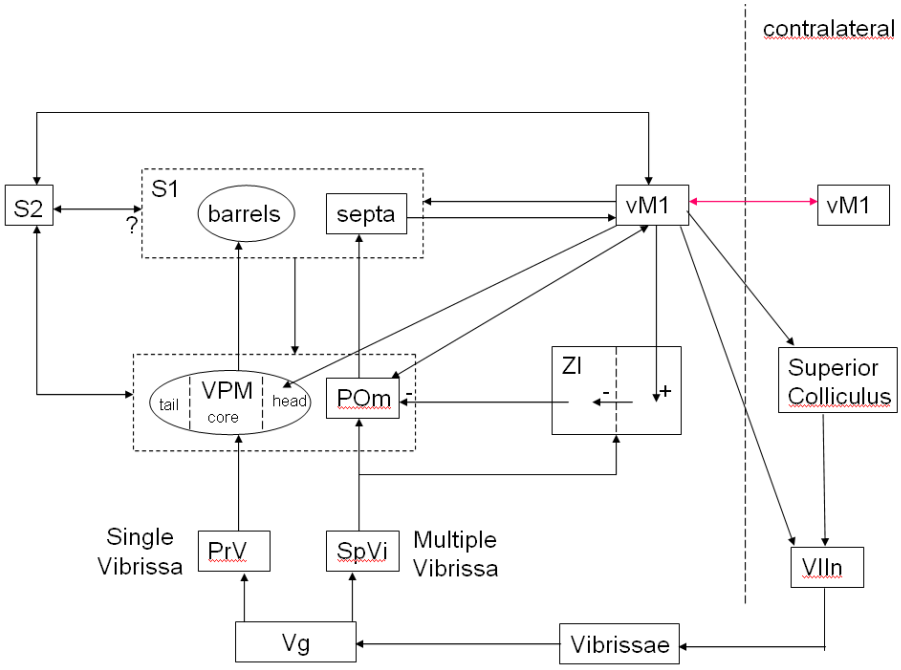

Figure 2.2: Diagram of vM1 connectivity with thalamus, cortex, and selected motor areas. Connectivity was compiled from (Miyashita et al., 1994b; Weiss and Keller, 1994; Izraeli and Porter, 1995a; Zhang and Deschenes, 1997; Hoffer and Alloway, 2001; Hoffer et al., 2003; Veinante and Deschenes, 2003; Alloway et al., 2004; Chakrabarti and Alloway, 2006; Alloway, 2007; Rocco and Brumberg, 2007; Urbain and Deschenes, 2007a, b).

2.3 Organization of vM1

There is an apparent contradiction in the motor cortex literature over whether vM1 is organized somatotopically or functionally. The somatotopic hypothesis is that the vibrissa representation is organized into an ordered map much like a coarse analog to barrel cortex. Evidence for this is three-fold. First, projects in a somatotopic manner to vM1 with different rows projecting to separate areas within vM1 (Izraeli and Porter, 1995a). Second, stimulation experiments where low threshold current evokes movement from a local group of one to three vibrissae have reported an organized map where posterior vibrissae are represented more posterior in vM1 and doral vibrissae are represented more medial (Hoffer et al., 2003; Brecht et al., 2004). Third, deflections of different vibrissae evoke activation of voltage-sensitive dye in an organized map in vM1 (Ferezou et al., 2007).

The alternate hypothesis, that vM1 is organized functionally, states that vM1 is divided into a posterior-medial protraction region and a larger anterior-lateral retraction region. The claim is that electrical stimulation leads to protraction or rhythmic movements of the vibrissae only in the protraction region (Haiss and Schwarz, 2005a; Cramer and Keller, 2006a). One clue that may resolve these disparate observations is that the action of the retractor

muscles can occlude activation of the protractor muscles. This phenomenon was shown in an anesthetized stimulation experiment where net retraction of the vibrissae was observed despite co-activation of protractor and retractor muscles (Berg and Kleinfeld, 2003b). Our hypothesis was that the protraction region extends throughout the retraction region but is occluded by the action of the retractor muscles. To this end, we stimulated vM1 in anesthetized rats before and after transection of the retractor muscles (Fig. 2.3). This action converted cortex that formerly only produced retraction movements into a somatotopic map of the vibrissae.

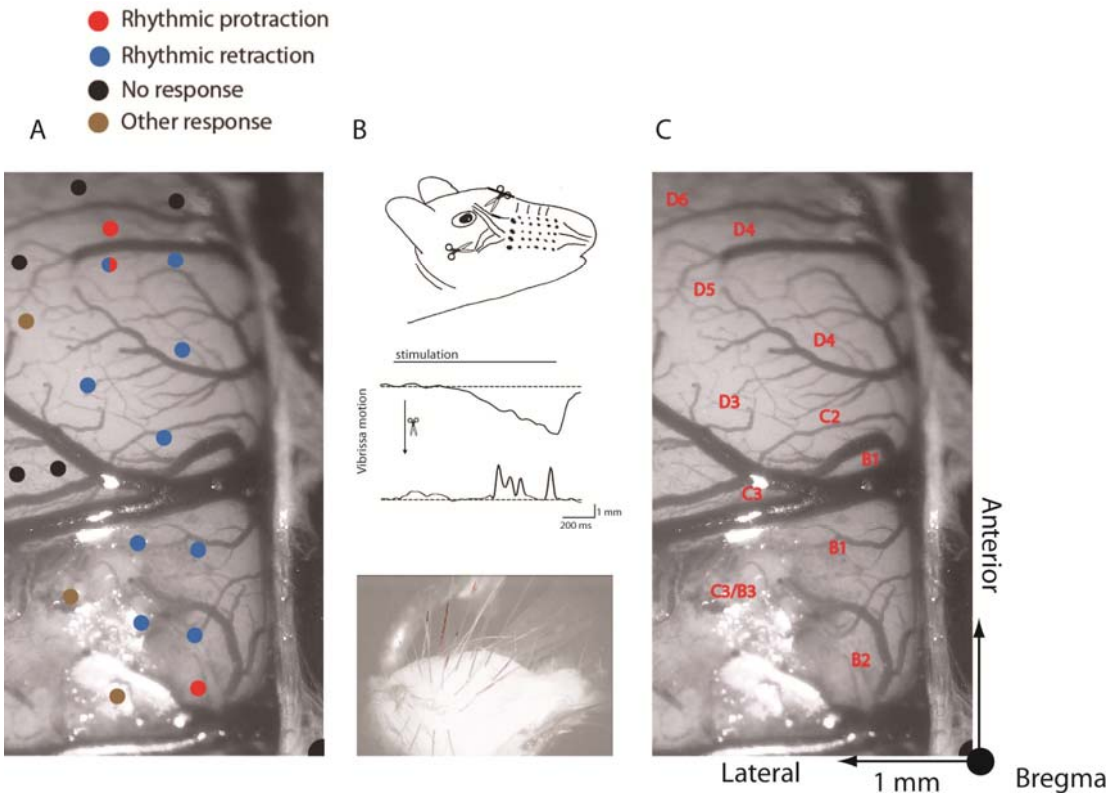

Figure 2.3: Protractor and retractor muscle representations are intermingled in vM1. **A.** Map of protraction and retraction region in vM1 of intact animal. Motor cortex was stimulated in anesthetized rat with a 1.5 megohm platinum-iridium electrode placed at a depth of 1.6 mm below cortical surface. Stimulation was a 1 s train of 200 μs pulses delivered at 60 Hz. Stimulation amplitude was typically between 5 and 25 μA.. **B.** Transection of retractor muscles. *Top panel.* Cartoon illustration of transaction of retractor muscles *m. nasolabialis* and *m. maxillilabialis*. *Middle panel.* Motion traces of evoked movement from the same location before and after transection. A location originally identified as retracting has become protracting. *Bottom panel.* Difference image before and during cortical stimulation. Image is before stimulation and red is difference during stimulation. Near threshold stimuli could evoke movement localized to a single vibrissa. **C.** Vibrissa map of same animal after muscle transaction. Red letters indicate central vibrissa of evoked movement. Stimulation typically recruited a local cluster of 2-4 vibrissae. Scale bars are same in A and C.

2.4 Role of motor cortex in control

Rhythmic whisking persists in animals after decortication (Gao et al., 2003b), decerebration (Semba and Komisaruk, 1984a), and sensory

denervation (Gao et al., 2001), indicating that there is a subcortical central pattern generator that rhythmically drives the whisking motor neurons. The anatomical data reviewed above shows both direct and indirect connections between vM1 and facial motor neurons, suggesting that vM1 may be able to control whisking via the central pattern generator or to subsume control of whisking entirely. The stimulation experiments discussed above evoke either long-lasting rhythmic vibrissa movement or brief, short-latency pulsatile movements. Thus, the data are consistent with cortex controlling whisking behavior on both a fast and slow timescale. The few studies of behaving electrophysiology in vM1 also suggest dual roles for this area.

The one previous publication on spike train data from vM1 in awake, whisking rats found correlations between the amplitude of protractor muscle activity and neural firing rates (Carvell et al., 1996b). However, they did not observe any rhythmic locking of vibrissa movement to muscle activity, which is thought necessary for cycle-by-cycle control of whising. A study of local field potential (LFP) signals in vM1 found that the amplitude of the LFP signal increased in a period of a few hundred milliseconds prior to a whisking epoch implicating vM1 in the initiation but not necessarily the maintenance of a whisking epoch (Friedman et al., 2006b). However, a separate study found that LFP activity rhythmically locks to whisking, albeit weakly (Ahrens and Kleinfeld, 2004). This locking was found to persist after sensory denervation

indicating the source was efferent in nature. Because of the difficulty of disentangling efference, efferent copy, and re-afference, the role of vM1 in control of whisking is still wide open.

2.5 Prospects for the future

There remain several outstanding issues regarding motor control and whisking that impede progress in using this system to understand sensorimotor processing. First and foremost is the unidentified neural substrate of the central pattern generator for whisking. Several areas have been proposed as candidate sights including the reticular formation (Hattox et al., 2002) and the facial nucleus itself (Hattox et al., 2003a; Cramer et al., 2007). Evidence is inconclusive and the question will likely only be answered by systematic lesion of these areas or by recording from them in a behaving animal. The ability to evoke whisking in lightly anesthetized animals may expedite this process (Cramer and Keller, 2006a). The role of all other motor areas will likely be framed in terms of their ability to manipulate or subsume the central pattern generator.

Secondly, there is currently little information on behavioral deficits associated with lesions of vM1. Such data would shed light on the role of motor cortex in forming behavioral strategies or in shaping perception of

stimuli. The several behavioral paradigms listed above are all excellent candidates for testing cortical lesions.

Lastly, it is unknown whether efferent copy and re-afferent signals interact in S1 and vM1 and if so how. The data presented in chapter 4 of this thesis is a first step towards answering this question as it addresses the representation of self-motion in these two cortices. However, a complete characterization requires independent manipulation of efferent and re-afferent signals in order to observe their interaction. This independent manipulation could be effected through a combination of electrically stimulated whisking and reversible nerve block.

2.6 Acknowledgments

The content of this chapter is a manuscript that is currently under preparation for submission with David Kleinfeld as second author.

Chapter 3 - Biomechanics of the vibrissa motor plant in rats

The biomechanics of a motor plant constrain the behavioral strategies that an animal has available to extract information from its environment. We used the rat vibrissa system as a model for active sensing and determined the pattern of muscle activity that drives rhythmic exploratory whisking. Our approach made use of electromyography to measure the activation of all relevant muscles in both head-fixed and unrestrained rats and two-dimensional imaging to monitor the position of the vibrissae in head-fixed rats. Our essential finding is that the periodic motion of the vibrissae and mystacial pad during whisking results from three phases of muscle activity. First, the vibrissae are thrust forward as the rostral extrinsic muscle *m. nasalis* contracts to pull the pad and initiate protraction. Second, late in protraction the intrinsic muscles pivot the vibrissae further forward. Third, retraction involves the cessation of *m. nasalis* and intrinsic muscle activity, and the contraction of the caudal extrinsic muscles *m. nasolabialis* and *m. maxillolabialis* to pull the pad and the vibrissae backward. We developed a biomechanical model of the whisking motor plant that incorporates the measured muscular mechanics along with movement vectors observed from direct muscle stimulation in anesthetized rats. The results of simulations of

the model quantify how the combination of extrinsic and intrinsic muscle activity leads to an enhanced range of vibrissa motion than would be available from the intrinsic muscles alone.

3.1 Introduction

A ubiquitous feature of perception is that the movement of biological sensors is subject to active control. Sensory receptors are often embedded in a specialized mechanical apparatus, referred to as a motor plant, that affords the animal precise control over their position and orientation. Within mammalian vision, the eyes are controlled by extraocular muscles that allow for a wide range of motor behaviors that include saccades, pursuit, accommodation, and vergence (Haslwanter, 2002). Within human haptic perception, the highest density of tactile receptors are found on the hands, arguably our most complex motor apparatus (An et al., 1989). In rodent somatosensation, the vibrissae of the animal's snout are moved by a complex network of muscle fibers that comprise more than 50 individual muscles (Dorfl, 1982; Wineski, 1985).

The vibrissa system in rat provides an ideal model for the investigation of a motor plant that is central to active sensing (Kleinfeld et al., 1999; Kleinfeld et al., 2006). In a form of whisking called exploratory whisking, rats rhythmically

sweep their vibrissae at 4 to 12 Hz (Vincent, 1912; Welker, 1964). Trained animals typically whisk for bouts of one or more seconds during which the vibrissae move predominantly in the horizontal plane (Bermejo et al., 2002) with great temporal regularity (Berg and Kleinfeld, 2003a). Rhythmic whisking exhibits bilateral symmetry (Gao et al., 2001) in the absence of head movements (Towal and Hartmann, 2006) or contact with an object (Gao et al., 2001; Sachdev et al., 2003)) and thus may be described by three possibly interdependent control parameters: frequency, amplitude of movement, and anterior-posterior set-point.

The motor plant that underlies exploratory whisking consists of the vibrissae, the mystacial pad, and a network of intrinsic and extrinsic musculature (Dorfl, 1982; Wineski, 1985). The vibrissae form an ordered grid of tactile hairs, each held by a follicle that is embedded in the mystacial pad. The musculature of the pad can be divided into two groups (Dorfl, 1982; Wineski, 1985): (*i*) the intrinsic muscles, which are small sling-like muscles that wrap around the base of each follicle and attach to the superficial part of the next caudal vibrissa, and (*ii*) the extrinsic muscles, which have bony attachment points external to the pad and send fibers throughout the pad's extent without associating with individual vibrissae (Fig. 3.1). Electromyography has previously shown that intrinsic muscles activate rhythmically during vibrissa protraction (Carvell et al., 1991) and that one of

the extrinsic muscles, *m. nasolabialis*, activates during retraction (Berg and Kleinfeld, 2003a). Yet we currently lack a composite understanding of the complete muscular control of vibrissa motion, including passive contributions and geometric constraints.

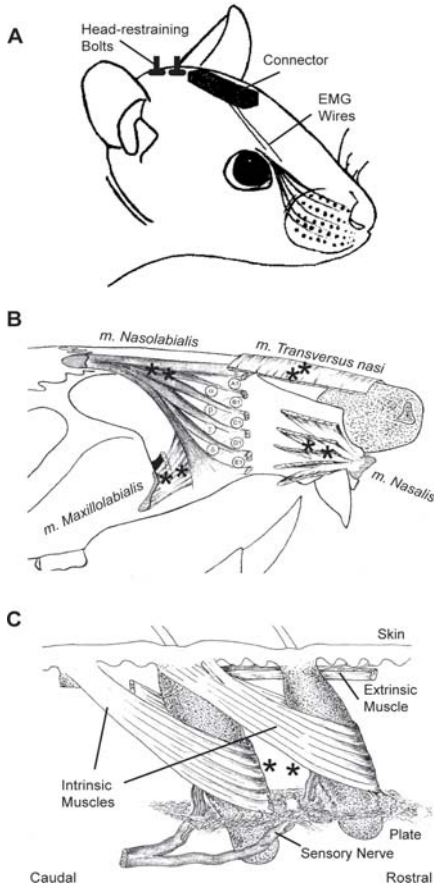

Figure 3.1: Intrinsic and extrinsic musculature of the mystacial pad.
(A) Drawing of the surgical preparation. Rats were implanted with EMG microwires and head-restraining bolts. EMG electrodes exited the skin through a catheter placed just caudal to the eyes at the midline and were soldered to a custom-made connector board. Head-restraining bolts were placed caudal to the connector at the midline. **(B)** Drawing of extrinsic musculature. Four extrinsic muscles invade the mystacial pad while maintaining external attachment points. *M. nasolabialis* attaches dorsal-caudal to the pad and runs superficially below the skin. *M. maxillolabialis* attaches ventral-caudal to the pad and fuses with the fibers of *m. nasolabialis* as they invade the pad. *M. nasalis* attaches rostral to the pad at the nasal septum and runs deep to the follicles as it extends caudally. *M. transversus nasi* lies transverse to the snout and runs superficially through the pad. The recording sites for each muscle are indicated by asterisks. **(C)** Drawing of intrinsic musculature and follicular anatomy. The intrinsic muscles join adjacent follicles of a single row. Each muscle attaches medially and laterally to the superior part of the caudal follicle while forming a sling around the lower third of the rostral follicle. The skin and other connective tissue, *e.g.*, the fibrous *plate*, provide a passive visco-elastic restoring force. Superficial extrinsic muscles run just below the skin. Asterisks indicate the approximate locations of the exposed tips of a pair of EMG microwires. The drawings in panels *B* and *C* were adapted from figures 1 and 3 in Dorfl (Dorfl, 1982; Dorfl, 1985); *m. nasolabialis* is also referred to as *m. levator labii superioris*. Note that in the convention of Wineski (Wineski, 1985) *m. transversus nasi* corresponds to *m. nasolabialis superficialis, m. nasalis* corresponds to *m. nasolabialis profundus*, and the intrinsic muscles are referred to as vibrissal capsular muscles.

Here we ask: (*i*) What is the complete pattern of muscle activity that underlies rhythmic vibrissa movement in rats? (*ii*) What are the detailed mechanical properties of the motor plant? (*iii*) Can we summarize the biomechanical properties in terms of an anatomically-based model of the whisking motor plant? (*iv*) What are the functional roles of the various physical components of the vibrissa system?

3.2 Methods

Subjects

We report data from 17 Long-Evans adult female rats, 250 to 350 g in mass. In 10 of these rats, pairs of microwires were implanted in the musculature of the mystacial pad to record the electromyogram (EMG), as described previously (Berg and Kleinfeld, 2003a) and appended as described below. Head-restraining bolts were embedded in the head-mount along the midline of the skull (Fig. 3.1A) as described (Bermejo et al., 1996). After recovery, these rats were trained to whisk while head-fixed for a chocolate drink reward using an operant conditioning paradigm designed to elicit large-amplitude whisks (Gao et al., 2003a). A subset of these rats were also trained to whisk unrestrained on a platform (Ganguly and Kleinfeld, 2004).

Four additional rats were used for muscle stimulation experiments that were performed under anesthesia. A final set of 3 rats was used for histological studies. The care and all aspects of experimental manipulation of our animals were in strict accord with guidelines from the National Institute of Health (NIH, 1985) and have been approved by Institutional Animal Care and Use Committees at Hunter College, City University of New York, and University of California, San Diego.

EMG surgery

All surgeries were performed under ketamine (90 mg per kg rat mass) and xylazine (10 mg per kg rat mass) anesthesia. Injections were made intraperitoneally with supplemental injections of ketamine (20 mg per kg rat mass) given every 2 hours as needed. Bupivicaine, a local anesthetic, was administered at the surgical incision to minimize post-operative pain.

Electrodes for muscle implantation were constructed from Teflon™-coated tungsten microwire (0.002” diameter, California Fine Wire, Grover Beach, CA). Microwires were stripped of 1 mm of insulation and implanted in pairs. The tips were separated by approximately 1 mm and oriented along the muscle fibers to obtain the maximum signal (Kamen and Caldwell, 1996). Two incisions were made to expose the musculature for implantation of EMG

electrodes: (*i*) a midline incision extending from the back of the skull to the end of the snout; and (*ii*) a lateral incision just caudal to the mystacial pad extending from the midline to the most ventral vibrissa row. The skin was deflected to reveal the two extrinsic muscles *m. nasolabialis* and *m. maxillolabialis* (Fig. 3.1B). The exposed tip of each electrode was pressed into the muscle tissue and secured at its entry point using Nylon™ sutures (no. 6-0, Ethicon, Johnson and Johnson, Piscataway, NJ). It was not practical to directly expose the intrinsic muscles because of their small size, nor *m. nasalis* because of its deep location within the pad (Figs. 3.1B and 3.1C). These muscles were implanted by threading the microwires through a 26-guage needle and shuttling the needle beneath the skin to its target (Berg and Kleinfeld, 2003a). Wire tips were bent back at the needle tip to anchor the wires to the surrounding tissue. These wires were sutured in place at the point where they exited the pad. Finally, a pair of reference wires were stripped of 4 mm of insulation and implanted in the dermis at the tip of the snout, beyond the extent of *m. transversus nasi.*

Electrodes to monitor activation of the intrinsic muscles were implanted in all rats, while electrodes to monitor up to three extrinsic muscles were implanted in specific rats (Table 3.1). Electrode positions were verified at the conclusion of surgery by passing current through the implanted microwires to stimulate the muscles and confirm the site of implantation. Each muscle has

a specific direction of action and produces a characteristic ratio of pad movement to vibrissa deflection as determined in a separate set of stimulation experiments (Fig. 3.7). These data were used to confirm that the movement stimulated via the microwires was typical for the implanted muscle. In the case of an intrinsic muscles implantation, the EMG electrodes were unlikely to be inside a specific intrinsic muscle. We determined an implantation to be successful if minimal stimulation deflected a localized group of 1 to 3 vibrissae without larger pad movement.

The raw EMG signals were processed as previously described (Fee et al., 1997; Ganguly and Kleinfeld, 2004). In brief, the electrical signals were bandpass filtered with a 16 Hz first-order high-pass filter and a 10 kHz, sixth-order Bessel low-pass filter and digitized at 25 kHz. We then numerically calculated the differential EMG signal across the pair of wires in each muscle, filtered these signals between 400 Hz and 3 kHz with a seventh-order Butterworth band-pass filter run sequentially in the forward and reverse directions, rectified the signals by taking their absolute value, and then smoothed the signals with a fourth-order Chebyshev low-pass filter run sequentially in the forward and reverse directions. The cut-off frequency of the final filter was varied for different analyses. The final rectified and smoothed differential EMG signals are denoted $|\nabla EMG|$.

Table 3.1: Slope of phase lag versus whisking frequency.

Animal		**Slope, $\Delta\phi/\Delta f$** (mean ± 2 SE) in π radians/Hz		
Number	**Condition**	**NL**	**NA**	**ML**
1	Freely exploring	-0.04 ± 0.03	0.04 ± 0.05 *	-
2	Freely exploring	-0.04 ± 0.03	0.03 ± 0.03 *	-
3	Freely exploring	-0.10 ± 0.08	-0.20 ± 0.08	-0.04 ± 0.04
4	Freely exploring	-0.00 ± 0.03*	-	-
5	Freely exploring	0.02 ± 0.02 *	-	-
6	Head-fixed	-0.09 ± 0.02	0.01 ± 0.01 *	-
7	Head-fixed	-0.03 ± 0.04 *	0.01 ± 0.06*	0.07 ± 0.03
8	Head-fixed	-0.04 ± 0.08 *	-0.09 ± 0.09*	-0.07 ± 0.09 *
9	Head-fixed	-	-0.02 ± 0.06 *	-
10	Head-fixed	-0.05 ± 0.04	-0.06 ± 0.04	-0.08 ± 0.04
Population Average		-0.04 ± 0.02	-0.02 ± 0.01	-0.01 ± 0.04 *

* Indicates that the null hypothesis of zero slope is satisfied ($p \leq 0.05$).

The raw EMG signals were processed as previously described (Fee et al., 1997; Ganguly and Kleinfeld, 2004). In brief, the electrical signals were bandpass filtered with a 16 Hz first-order high-pass filter and a 10 kHz, sixth-order Bessel low-pass filter and digitized at 25 kHz. We then numerically calculated the differential EMG signal across the pair of wires in each muscle,

filtered these signals between 400 Hz and 3 kHz with a seventh-order Butterworth band-pass filter run sequentially in the forward and reverse directions, rectified the signals by taking their absolute value, and then smoothed the signals with a fourth-order Chebyshev low-pass filter run sequentially in the forward and reverse directions. The cut-off frequency of the final filter was varied for different analyses. The final rectified and smoothed differential EMG signals are denoted |∇EMG|.

Behavioral Training

Animals were initially handled and gentled for five days, followed by at least one week of body-restraint training, during which the rat's body was enclosed in a snug cloth sack that left its head free. The animal was then either placed into its home cage or the rat holder of the behavioral apparatus (Fig. 3.2A, left panel) for twenty minutes each day until the animal acclimated to body restraint. Animals were then implanted with EMG microwires and given a minimum of 2 days to recover.

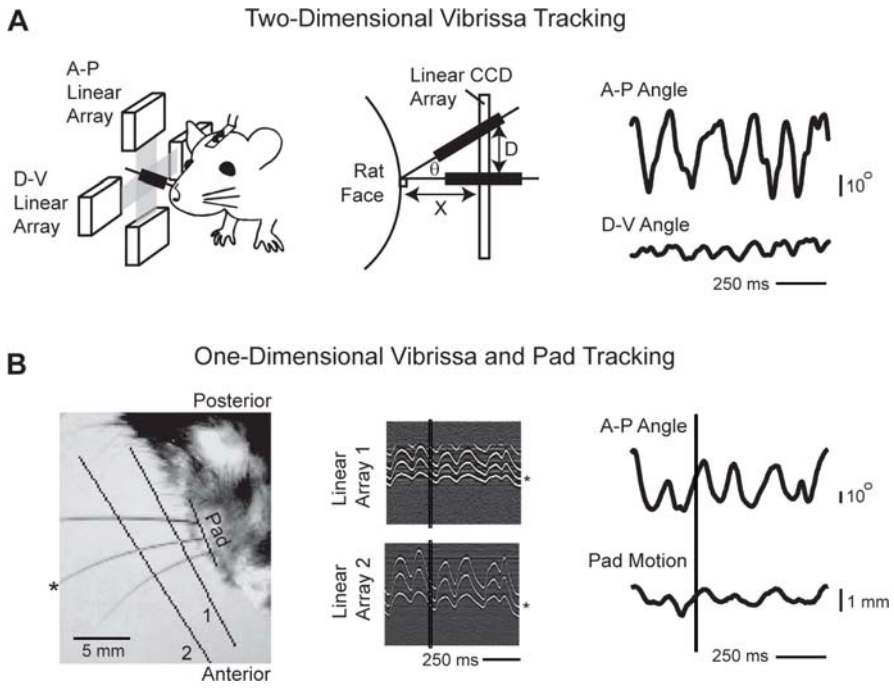

Figure 3.2: Tracking methods for vibrissa and pad movement in head-restrained rats. **(A left)** Drawing of apparatus used for A-P and D-V vibrissa tracking. Vibrissa C3 was marked with an adhesive strip of foam to enlarge its shadow on two perpendicularly-mounted linear CCD arrays. **(A center)** Schematic of method used to calculate the A-P and D-V angle of the marked vibrissa. A calibration point was chosen along the linear array by taking a line normal to the face at the base of the vibrissa and finding its intersection with the linear array. This position was defined as 90º. Given the distance between the calibration point and the face, X, and the distance between the calibration point and the vibrissa's shadow, D, the angle of the vibrissa, θ, was determined from the formula $\tan\theta = D/X$. **(A right)** Trace of vibrissa motion over time. Increases in angle correspond to anterior or dorsal movement of the vibrissae while decreases correspond to posterior or ventral movement. **(B left)** Image taken from set-up used to track A-P angle of vibrissa and A-P translation of mystacial pad. A 2-D CCD camera was mounted above the rat's head. Linear arrays were manually chosen from the image to track the vibrissa at multiple points. The pad was marked manually to determine the vibrissa angle and to find the point of intersection between the vibrissa and the face. For this method, vibrissae were clipped except for C1, C2, and C3. The vibrissa tracked in this example is marked with an asterisk. **(B center)** Output of the linear arrays as a function of time. The image has been filtered as described in *Methods* with intensity flipped so that the vibrissae appear white. The black vertical line marks the frame shown at *left* and the asterisk marks the tracked vibrissa. **(B right)** Trace of vibrissa and pad motion over time. Pad position was calculated by finding the intersection between the pad line and the line formed by the points tracked along the vibrissa. An increase in pad position corresponds to anterior translation. The vertical black bar represents the slice in time when the image at *left* was taken.

Electromyographic signals and vibrissa position were tracked during behavioral sessions that consisted of 30 trials, each of 60 s in duration. The animal was placed in a cloth sack and held in the head-fixing apparatus with its head bolts locked into place. Stable periods of whisking in air were generated using a Go/No-Go task in which the Go condition had a variable-interval for reward and the No-Go condition was unrewarded (Gao et al., 2003a). On Go trials the availability of reinforcement was signaled by the onset of a light and tone combination. Vibrissa movements were monitored in real time and rats were reinforced for protractions that were greater than 40° in amplitude and no more than once every 5 s.

Data in the head-fixed condition were compared with the whisking responses obtained from unrestrained rats tested on whisking in air while on a raised platform. To elicit whisking, the rat was repeatedly shown its home cage, and, after several whisking bouts, the animal was allowed to spend a few seconds in the cage before being returned to the platform (Ganguly and Kleinfeld, 2004). These sessions typically lasted 20 minutes. Finally, we note that neither the head-fixed nor unrestrained animals in this study performed foveal whisking behavior, *i.e.*, whisk frequency greater than15 hz.

Vibrissa Tracking

Vibrissae C1 to C3 move largely in the horizontal plane when the animal's head is restrained. Two complementary systems were used to track different aspects of this motion in head-fixed sessions. In the first, a pair of perpendicularly mounted optoelectronic devices were used to track vibrissa movement along the anterior-posterior (A-P) and dorsal-ventral (D-V) axes (Fig. 3.2A, left panel). Each device consisted of a linear CCD array opposite an infrared laser emitter (Alpha X07, Metralight, Santa Clara, CA). The system has a temporal resolution of 1 ms, a spatial resolution of 7 μm, and a spatial range of 28 mm. All vibrissae were intact and a foam marker of diameter 1 mm was attached to a single vibrissa to enlarge its shadow on the array. The angle of the vibrissa was calculated using the measured distance of the devices from the pad, typically 10 mm, and a calibration point taken to be normal to the face (Fig. 3.2A, center panel). This system allowed us to identify the action of extrinsic muscles that do not pull solely along the A-P axis.

A second system made use of a high-speed video camera (A602f, Basler Vision Technologies, Exton, PA), with temporal resolution of 2 ms at our frame size and spatial resolution of 100-200 μm, to simultaneously monitor translation of the mystacial pad and motion of the vibrissae (Fig. 3.2B*)*, along the A-P axis only. Only vibrissae along row C were left intact in

order to avoid images with overlapping vibrissae. Software was developed in MatLab™ to track movement in the high-speed video. In brief, 2 or 3 linear arrays were selected from the video window and the associated pixels were extracted from each frame (Fig. 3.2B). Each array was processed by a band-pass spatial filter with a bandwidth matched to the vibrissa. The center-of-mass about the point of maximum intensity was taken as the location of the vibrissa. An estimate of the vibrissa's current velocity was used to narrow the range of pixels that were searched in the subsequent frame. To track the insertion point of the vibrissa into the pad, multiple points were tracked along the length of the vibrissa and were fit with a line. The intersection of this line and a stationary line manually chosen along the pad was taken to be the location of the insertion point.

Analysis and simulations

All spectral power densities and phase differences were calculated using the multi-taper spectral estimation techniques of Thomson (Thomson, 1982; Percival and Walden, 1993) as implemented in the *Chronux* toolbox for MatLab™ (www.chronux.org). Simulations were performed in MatLab™ using Runge-Kutta integration techniques (Press et al., 1988).

Stimulation experiments

Direct stimulation of the facial musculature was used in anesthetized rats to determine the magnitude and direction of the action of each muscle on the pad and vibrissae. The surgical procedure was performed as described for EMG implantation, except that the animal was transferred to the vibrissa tracking apparatus while still anesthetized. India ink was used to mark locations on the pad to aid tracking. Muscles were excited with a concentric bipolar stimulation electrode (FHC, Bowdoin, ME). A train of biphasic current pulses, 200 μs in duration, was passed through the electrodes with the current varied between 50 and 500 μA in amplitude and the frequency varied between 100 and 250 Hz. Animals were sacrificed at the end of the experiment.

Histology

Saggital sections of the mystacial pad were obtained from three rats. Animals were anesthetized with ketamine/xylazine, as above, and the fur around the vibrissae was removed using a chemical depilatory (Nair; Church & Dwight, Co., Madera, CA). The vibrissae were positioned in either a protracted or retracted posture and glued into place with a cyanoacrylate. The rat was then deeply anesthetized with pentobarbital and perfused with

phosphate buffered saline (PBS; Sigma; St. Louis, MO), followed by 4 % (w/v) paraformaldehyde in PBS. The left and right mystacial pads were removed and post-fixed in 4 % paraformaldehyde. A 2 mm wide section about the C row of the vibrissae was blocked and embedded in paraffin wax and blocks were sectioned at a thickness of 5 μm (Pacific Pathology, San Diego, CA). Selected sections were processed with a trichrome stain (Masson; Sigma, St. Louis, MO) to contrast muscle fibers and connective tissue for microphotography under bright-field illumination at low magnification.

3.3 Results

We first present the $|\nabla EMG|$ recorded from the facial muscles of 10 rats during awake, behaving exploratory whisking. In 5 of these animals, measurements were taken in the freely exploring condition in which animals whisked while confined to a raised platform. In a separate set of 5 rats, data were taken in the head-fixed condition; this paradigm allowed us to perform automated vibrissa tracking. The spectral characteristics of head-fixed whisking are analyzed to identify the potential effect of this manipulation on behavior. Our focus then shifts to direct muscle stimulation in an anesthetized preparation. The combined data from these experiments is

used to inform a biomechanical model of the whisking motor plant that provides the link between motor neuron signals and vibrissa movement.

Intrinsic and Extrinsic |∇EMG| in Relation to Vibrissa Motion

We recorded |∇EMG| activity from the intrinsic and extrinsic muscles of freely exploring animals that were trained to whisk in air for their home cage. Our most striking observation is that all of the recorded muscles are rhythmically active through each whisking bout. In general, we observe that each muscle produces a burst of activity on each whisking cycle. While there is some overlap in the timing and duration of these bursts, they occur in a stereotypical sequence with the caudal extrinsic muscles *m. maxillolabialis* and *m. nasolabialis* contracting simultaneously, followed by the rostral extrinsic muscle *m. nasalis,* and finally the intrinsic muscles. Qualitative aspects of these observations are seen in the two example of figure 3.3A. This pattern is consistent with previous reports that the intrinsic muscles and *m. nasolabialis* contract in anti-phase (Berg and Kleinfeld, 2003a), but now we show that *m. nasalis* and *m. maxillolabialis* also contract rhythmically during exploratory whisking.

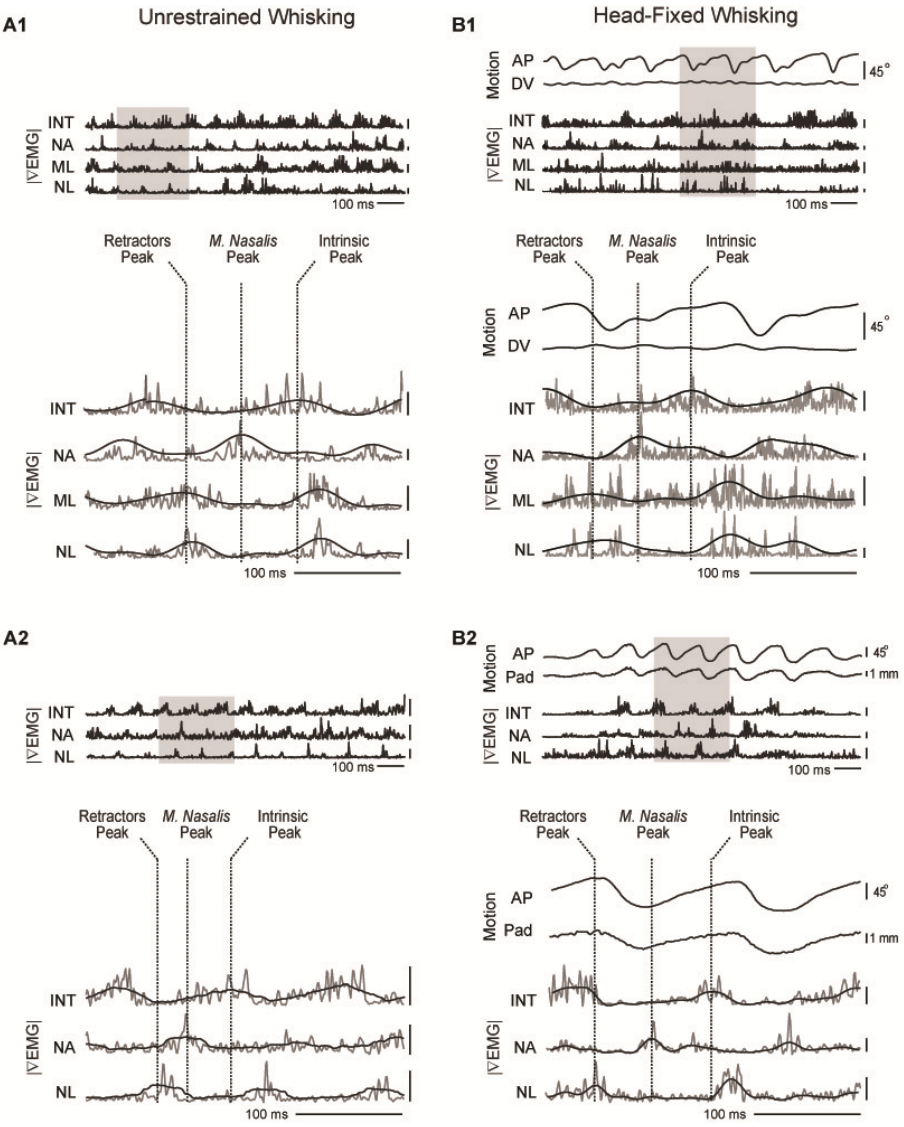

Figure 3.3: Muscle activity and vibrissa motion from head-restrained and unrestrained rats.

|∇EMG| signals are abbreviated as INT (intrinsic muscles), NA (*m. nasalis*), NL (*m. nasolabialis*), and ML (*m. maxillolabialis)*. Note that *m. maxillolabialis* was not recorded in every animal. Shaded area in upper panel is shown in detail in lower panel along with dashed vertical lines to indicate the three phases of muscle activity. |∇EMG| traces are low-pass filtered at 250 Hz except for black |∇EMG| traces in lowers panel which were low-pass filtered at 20 Hz. All voltage scale bars are 100 μV. **(A1, A2)** Examples of triphasic whisking from two unrestrained animals. **(B1)** Example of triphasic whisking from a head-fixed animal showing A-P and D-V vibrissa motion. **(B2)** Example of triphasic whisking from a second head-restrained animal where A-P pad movement was tracked.

Vibrissa motion and muscle activity during head-fixed whisking

Examination of whisking bouts from head-fixed animals confirms that intrinsic and extrinsic muscle activity maintains rhythmic contraction with a 3.phase sequence under head-restraint. Comparing the |∇EMG| to motion of the shaft along the A-P axis, we observe that the caudal extrinsic muscles *m. nasolabialis* and *m. maxillolabialis* reach their maximum activation during retraction, consistent with previous recordings of *m. nasolabialis* and shaft motion (Berg and Kleinfeld, 2003a). Maximal activation of the rostral extrinsic muscle *m. nasalis* occurs early during protraction while activity in the intrinsic muscles peaks near the end of protraction. Qualitative aspects of these observations are seen in the two examples of figure 3.3B.

Quantification of whisking

We calculated the average |∇EMG| and vibrissa trajectory during all whisking bouts as a means to quantify the sequence of muscle activation across whisking cycles. Direct averaging of whisk cycles was prohibited by the large variability in whisking frequency, ranging from 4 to 12 Hz. To compare cycles of different duration, we averaged across phase. Individual whisk cycles, with amplitude of 20^{o} or more, were taken to last a period of 2π radians and then the complete set of traces was averaged by phase. The result of averaging 1750 cycles in one head-fixed animal illustrates the

essential relative phase relationships (Fig. 3.4). First, the average |∇EMG| activity confirms the 3.phase nature of rhythmic whisking. The peak activities of *m. nasolabialis* and *m. maxillolabialis* nearly coincide and are distinct from the peak activity of *m. nasalis* and the intrinsic muscles. Secondly, the extreme positions of vibrissa motion are slightly preceded by the maximum activation of specific muscles. In particular, the caudal extrinsic muscles exhibit maximum activation just before the end of retraction and the intrinsic muscles peak just before the end of protraction. The activity of *m. nasalis* rises before retraction ends but reaches a peak after the onset of protraction. The relative phase relationship between maximum muscle activation and vibrissa motion were similar in all head-fixed animals.

While the dominant motion is along the A-P axis, the average shaft motion along the D-V axis exhibits a distinct albeit small peak during retraction (Bermejo et al., 2002). This suggests that whisking on average takes a highly eccentric “backstroke” path, seen as a counterclockwise loop motion when viewing the right side of the face. By examining the shape of the trajectory of individual whisks, we confirmed that in greater than 80% of whisks the shaft moved in a distinctly counter-clockwise direction (data not shown).

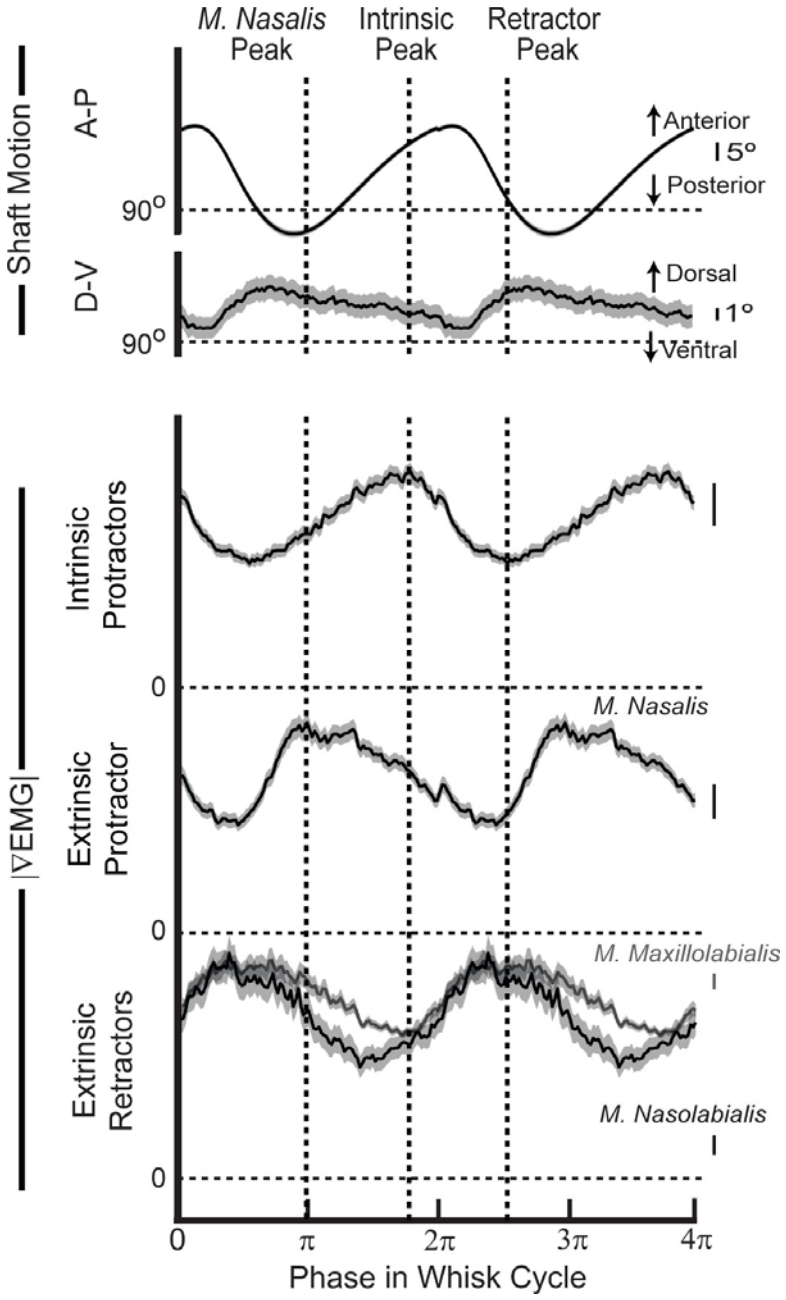

Figure 3.4: Average vibrissa motion and muscle activity from a head-restrained rat. Each whisk was linearly mapped from time onto the range of 0 to 2π radians so that the average is taken across phase. Average traces (1750 whisks) are repeated to display two cycles. Standard errors are shown as a gray boundary to each trace. |∇EMG| values were normalized by their maximum voltage. All voltage scale bars are 2 μV. The dashed vertical lines indicate the peaks of the three phases of average muscle activity. The peak for the extrinsic retractors was set midway between the individual peaks.

Phase lag of extrinsic muscle activity

The previous analysis rests on the assumption that individual whisks of different duration are comparable when rescaled in time. Moreover, the effect of whisking frequency on the pattern of muscle activity is of critical importance for characterizing the hypothetical central pattern generator(s) that underlie whisking (Welker, 1964; Semba and Komisaruk, 1984a; Gao et al., 2001; Berg and Kleinfeld, 2003a; Hattox et al., 2003b; Cramer and Keller, 2006b). Previously, *m. nasolabialis* was shown to activate at a constant phase lag with respect to the intrinsic muscles even as the frequency of whisking varied (Berg and Kleinfeld, 2003a). This is opposed to the hypothesis that muscle activity occurs at a constant time delay, which would result in a phase lag that increases with whisking frequency.

We test the hypothesis that the phase lag between all of the extrinsic muscles and the intrinsic muscles is constant as a function of whisking frequency, as illustrated across 200 bouts from a typical freely exploring animal (Fig. 3.5A). The peak of the activation of intrinsic muscles is defined as phase 0. First we examine the consistency of the average phase lags across animals (Figs. 3.5B to 3.5D). The phase lags of *m. nasolabialis* ($0.83\,\pi \pm 0.06\,\pi$ radians, mean ± S.E.) and *m. maxillolabialis* ($0.81\,\pi \pm 0.04\,\pi$ radians) were not significantly different, which supports the conclusion that these muscles operate concurrently. *M. nasalis* activated at a

relative phase of -0.71 π ± 0.06 π radians. For all three muscles, there was no significant difference for the mean phase of activation between freely exploring and head-fixed animals ($p > 0.05$). These data indicate that the relative phase shifts among muscle groups are preserved across animals, and that the three phases of whisking are approximately evenly spaced within the whisking cycle. Next we examined the phase lag of muscles of individual animals as a function of whisking frequency. In all 3 extrinsic muscles, the phase lag remained largely constant throughout the range of whisking frequencies (4 to 12 Hz across all animals). We quantified this observation by the slope of a line fit to the phase versus frequency plot for each animal (Table 3.1). For 2 of the 3 extrinsic muscles the mean slope was significantly different from zero albeit weakly so, *i.e.*, the change in phase lag over a range of 8 Hz would be less than 0.33 π radians compared to the separation of individual muscle phases of approximately 0.66 π radians.

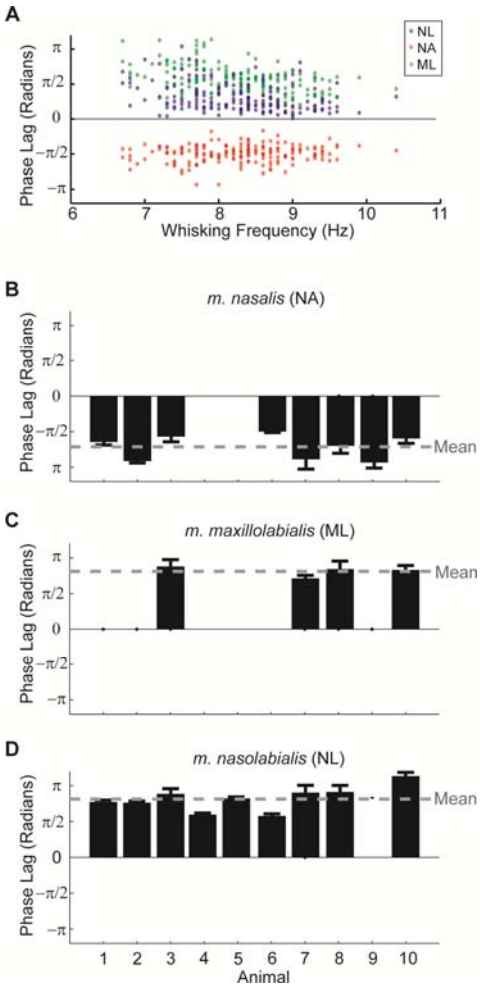

Figure 3.5: The phase relationship between intrinsic and extrinsic muscle |∇EMG| activity.
The phase was calculated with respect to the intrinsic muscles, which were defined as activating at phase zero. Positive phase values correspond to a phase lag relative to the intrinsic muscles while negative values correspond to a phase advance. **(A)** Phase lag of extrinsic muscles relative to the intrinsic muscles for a representative animal (n = 198 bouts). Each dot represents the phase lag of an individual extrinsic muscle for a single bout. The frequency of whisking was determined by the location of the peak in the power spectrum of the intrinsic muscle's |∇EMG|. Note the constant phase relationship of each muscle as a function of whisking frequency. (**B to D)** Summary of the mean phase lags for all muscles and animals used in this study. The number of whisking bouts is 250, 200, 198, 83, 125, 110, 125, 200, 180, and 351 for animals 1 through 10 respectively. Error bars indicate 2 standard errors, *i.e.*, 95.5 % confidence intervals. Columns with no bars correspond to animals where the particular extrinsic muscle was not implanted with EMG electrodes. The gray horizontal line is the mean phase across all animals.

Spectral Properties of Whisking

Previous studies have found that freely exploring rats whisk at a wide range of frequencies, but that the frequency of whisking during a single bout is exceedingly stable (O'Connor et al., 2002; Berg and Kleinfeld, 2003a). In our study we observed that individual whisking bouts of both restrained and unrestrained animals vary in frequency and rhythmicity (Figs. 3.6A and 3.6B). We now quantify the differences in the spectral characteristics of whisking behavior between freely exploring and head-fixed animals to determine the behavioral effect of restraint.

We determined the central frequency of whisking bouts from the peak of the power spectral density, f_{whisk} (insert, Fig. 3.6E) computed over the central 1.5 s interval from each bout. We then pooled the results for all rats in the same condition, either freely exploring or head-fixed, to find the probability distribution of whisking frequencies (Figs. 3.6C and 3.6D). Consistent with previous studies (Berg and Kleinfeld, 2003a), the frequency of whisking in unrestrained animals ranges between 6 and 12 Hz, with a mode at 9.3 Hz. In contrast, the histogram of head-fixed whisking bouts showed a distinct shift toward lower frequencies. Whisking ranged from 4 to 8 Hz, with a mode at 6.1 Hz. This difference in frequency did not result from our behavioral training paradigm as this lower frequency persisted in a rat that was not rewarded for large amplitude whisks (mean f_{whisk} = 6.3 Hz; n = 125 bouts).

Thus whisking in head-fixed animals was typically one-third slower than in freely exploring animals.

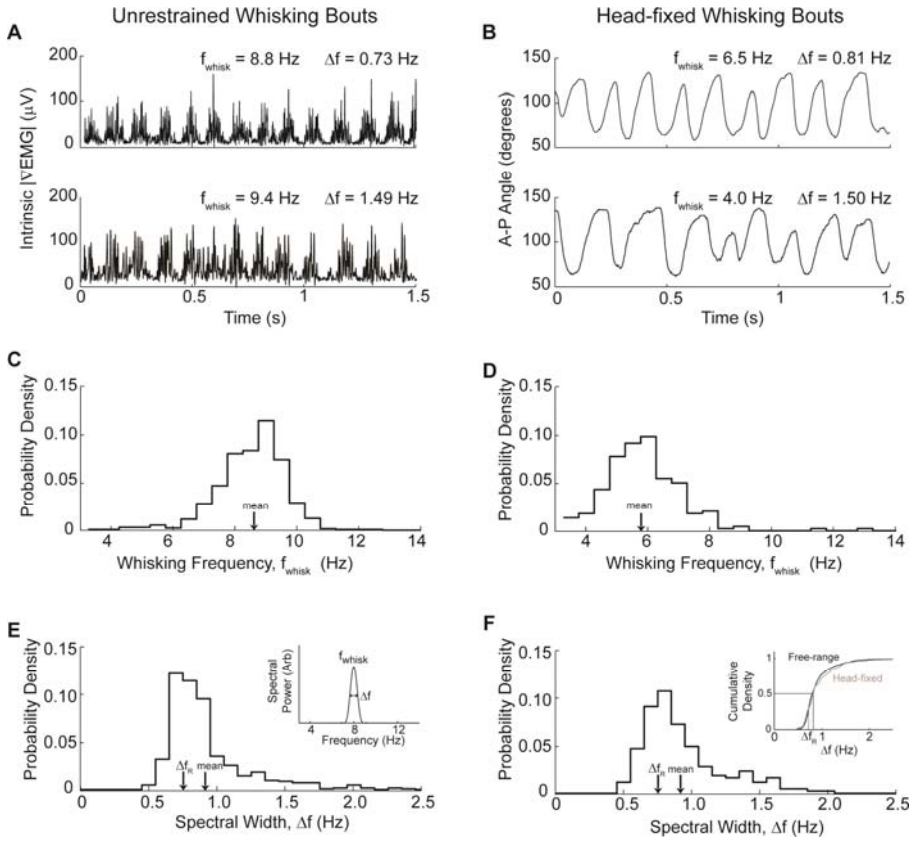

Figure 3.6: Spectral characteristics of freely exploring and head-fixed whisking.
(A and B) Examples of unrestrained (panel A) and head-fixed (panel B) whisking. |∇EMG| is shown for freely exploring animals while vibrissa angle along the A-P axis is shown for head-fixed animals. These bouts were chosen to demonstrate the variability in both frequency and regularity of whisking for animals in both conditions. **(C and D)** Probability distribution of whisking frequencies, $f_{whisk,}$ calculated from freely exploring (panel C, n = 566 bouts across 5 rats) and head-fixed (panel D, n = 195 bouts across 3 rats) animals. The frequency was calculated from the intrinsic |∇EMG| signal recorded during 1.5 second long whisking bouts and was defined as the frequency between 3 and 15 Hz with the greatest spectral power (inset in panel E). Bin size is 0.5 Hz. **(E and F)** Probability distribution of spectral width of whisking bouts calculated from freely exploring and head-fixed animals; data as in panels C and E. The spectral bandwidth Δf is defined as the full-width at half maximal amplitude of the spectral peak at f_{whisk}; this may be compared to the bandwidth of a pure sine wave, denoted by Δf_R = 0.73 Hz (insert in panel E). Bin size is 0.1 Hz. The mean spectral width was Δf = 0.93 Hz for freely exploring rats and Δf = 0.94 Hz for head-fixed rats. The cumulative probability distribution functions of the two widths are compared in the insert.

The regularity, or spectral purity, of a periodic signal is quantified by its spectral width Δf (insert, Fig. 3.6E). Highly regular, periodic behavior has a power spectrum with a narrow peak at the whisking frequency. The average width of this peak has a theoretical lower limit, called the Rayleigh limit, of Δf_R ~ (duration of bout)$^{-1}$. For our specific analysis, this limit is given by the full-width at half maximal amplitude of the power spectrum of a sine wave that is 1.5 s in duration, *i.e.*, Δf_R = 0.73 Hz. We found that the spectral width of the intrinsic muscle $|\nabla EMG|$ was typically near Δf_R in both freely exploring and head-fixed animals (Figs. 3.6E and 3.6F), which indicates that whisking was highly regular. Although the probability distributions of Δf appear to be similar in these two conditions, a statistical test on the cumulative probability density of spectral width shows that whisking in head-fixed animals is slightly less regular than that in freely exploring animals ($p = 0.04$; K-S test) (inset, Fig. 3.6F).

Movement Vectors From Direct Stimulation of Facial Muscles

The highly rhythmic nature of whisking makes correlation-based techniques, as employed above, ill-suited to disentangle the relationship between specific muscle activation and different aspects of vibrissa motion. To eliminate this confound, we directly stimulated intrinsic and extrinsic muscles in the anesthetized rat to determine the range of vibrissa motion each muscle can elicit, along with its direction of action and the time-course

of relaxation (Fig. 3.7). Since every muscle may both deflect vibrissae and translate the mystacial pad, we used frame-based imaging to simultaneously monitor both aspects of the motion.

We observed that each extrinsic muscle pulls the mystacial pad toward its respective attachment point (Fig. 3.7A and 7B). *M. nasalis* pulls the pad anterior, *m. maxillolabialis* pulls posterior-ventral, and *m. nasolabialis* pulls posterior-dorsal. Additionally, the muscle *m. transversus nasi* effects a strictly dorsal translation of the pad.

The concomitant activation of *m. nasolabialis* and *m. maxillolabialis* seen in the $|\nabla EMG|$ activity of awake animals (Figs. 3.4 and 3.5) suggests a cooperative role. In support of this, we found that a simultaneous and balanced stimulation of these two muscles produces a strictly posterior motion of the mystacial pad (Fig. 3.7B), even though the individual muscles have a strong D-V component. We conclude that active retraction along the A-P axis requires the simultaneous excitation of the two extrinsic retractor muscles.

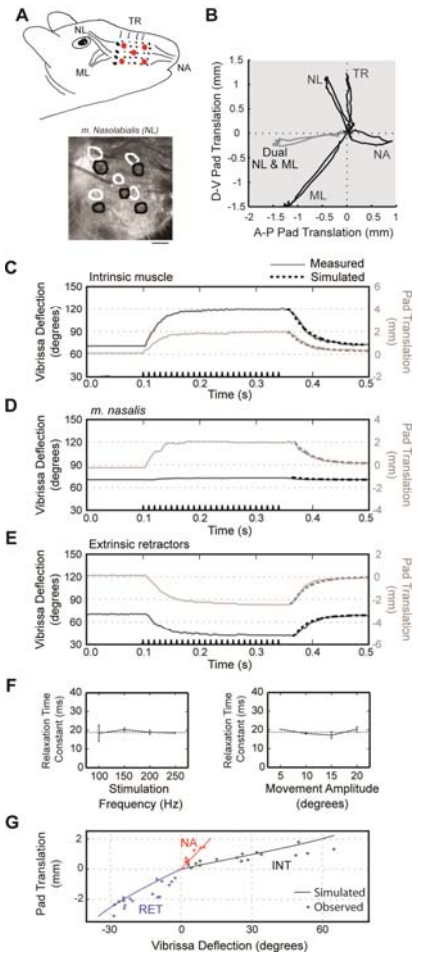

Figure 3.7: Trajectories of movement elicited by current stimulation of facial muscles in an anesthetized rat.
Motion is typical of results obtained from 4 rats. **(A)** *Upper panel.* Cartoon of extrinsic muscles indicating location of markers on pad (red dots). NL = *m. nasolabialis*, ML = *m. maxillolabialis*, NA = *m. nasalis*, TR = *M. Transversus nasi*. *Lower panel.* Image of mystacial pad with circles indicating location of the markers before stimulation (black) and during (white). **(B)** Pad motion during muscle stimulation. Each trace represents the path of the central marker on the mystacial pad during extrinsic muscle stimulation. Dual stimulation of *m. nasolabialis* and *m. maxillolabialis* in gray demonstrates the reduced D-V translation of the pad during simultaneous contraction of these muscles. **(C to E)** A-P vibrissa deflection and pad translation during muscle stimulation. The stimulus train is shown along the time axis. The dashed curve at the offset of stimulation is the estimated relaxation time course from the biomechanical model. **(F)** Relaxation time constant as a function of stimulus parameters. Both panels are from data obtained from intrinsic muscle stimulation in a single rat. Error bars are 1 S.E. Lack of error bar indicates only 1 data point was obtained. For movement amplitudes, trials were binned at the indicated value $\pm$ 5°. **(G)** Pad translation versus vibrissa deflection at peak movement during stimulus. Points represent all trials across 3 rats. Solid lines are estimated pad translation and vibrissa deflection from biomechanical model when only the indicated muscle is active.

We determined a time-constant for relaxation of the intrinsic muscles, *m. nasalis*, and the extrinsic retractors when stimulated together, following the offset of stimulation (Figs. 3.7C to 3.7E). The observed angular motion was fit with a decaying exponential, *i.e.*, $\theta = \theta_{rest} + \Delta\theta_{max}\exp(-t/\tau)$ where θ_{rest} is the position of the vibrissa in the absence of stimulation and $\Delta\theta_{max}$ is the steady-state amplitude of the stimulus induced motion. The time-constant for relaxation, τ, was found to lie between 18 and 26 ms (n = 4 for each muscle) across all muscle groups. As expected for a passive process, the relaxation time was independent of stimulus parameters (Fig. 3.7F). These results suggest that the relaxation force is a bulk property of the mystacial pad, rather than a property of a specific muscle. Lastly, we note that the rise time of vibrissa movement at the onset of stimulation varied with stimulus parameters. We did not fully investigate this phenomenon because extracellular stimulation of muscles recruits large rather than small individual fibers first, the reverse order of endogenous recruitment (Dorgan and O'Malley, 1997).

Finally, we determined the range of vibrissa and mystacial pad motion that can be elicited by each muscle (Fig. 3.7G). We use vibrissa C2 as a reference to compare our stimulation results to our behavioral data, though the range of motion may vary in different vibrissae. The range of vibrissa deflection about its rest angle is approximately 35° of retraction and 65° of

protraction, or a total range of approximately 100°. In our behavioral experiments, the full range of observed vibrissa angles was 108°. The total range of pad translation in stimulation experiments is approximately 5 mm in the A-P direction and 3 mm in the D-V direction. We note that each muscle exhibits a characteristic ratio of angular deflection to pad movement with the intrinsic muscles producing the largest deflections for a given amplitude of pad movement (Fig. 3.7G).

Electromechanical Model of Vibrissa and Mystacial Pad Motion

We now use the joint EMG and behavioral data (Fig. 3.4), with the stimulated movement data (Fig. 3.7), to develop an anatomically-based model of the motor plant (Fig. 3.8). The model serves to summarize, in a self-consistent manner, the relation between muscle activation and the movement of the vibrissae and mystacial pad. It consists of the equations of motion for the vibrissae as a function of the forces generated by the facial muscles, *i.e.*, intrinsics, *m. nasalis*, and the retractors taken together, and the visco-elastic properties of the mystacial pad. This yields a set of first-order nonlinear differential equations that we use to numerically simulate the A-P translation and rotation of the vibrissae. The full equations and initial conditions are given in the Appendix and Tables 3.4 to 3.7. Parameter values are given in Table 3.2. Our software implementation is included as Supplemental Information.

Table 3.2: Parameters used in biomechanical simulations.

Parameter	Value	Description
N	3	Number of vibrissae
l_h	40 mm	Length of hair
l_f	4 mm	Length of follicle
S	2 mm	Distance between vibrissae at rest
W	20 mm	Extent of mystacial pad
θ^{rest}	80°	Resting angle of vibrissae
M_h	0.5 mg	Mass of hair
M_f	10 mg	Mass of follicle
C	-1.43 mm	Center of mass of vibrissa as measured from base of hair
I	112 mg•mm	Moment of inertia of vibrissa unit about center of mass
$\tau^{relaxation}$	27 ms	Relaxation time-constant of the mystacial pad

† Each value represents the mean from across 3 rats.

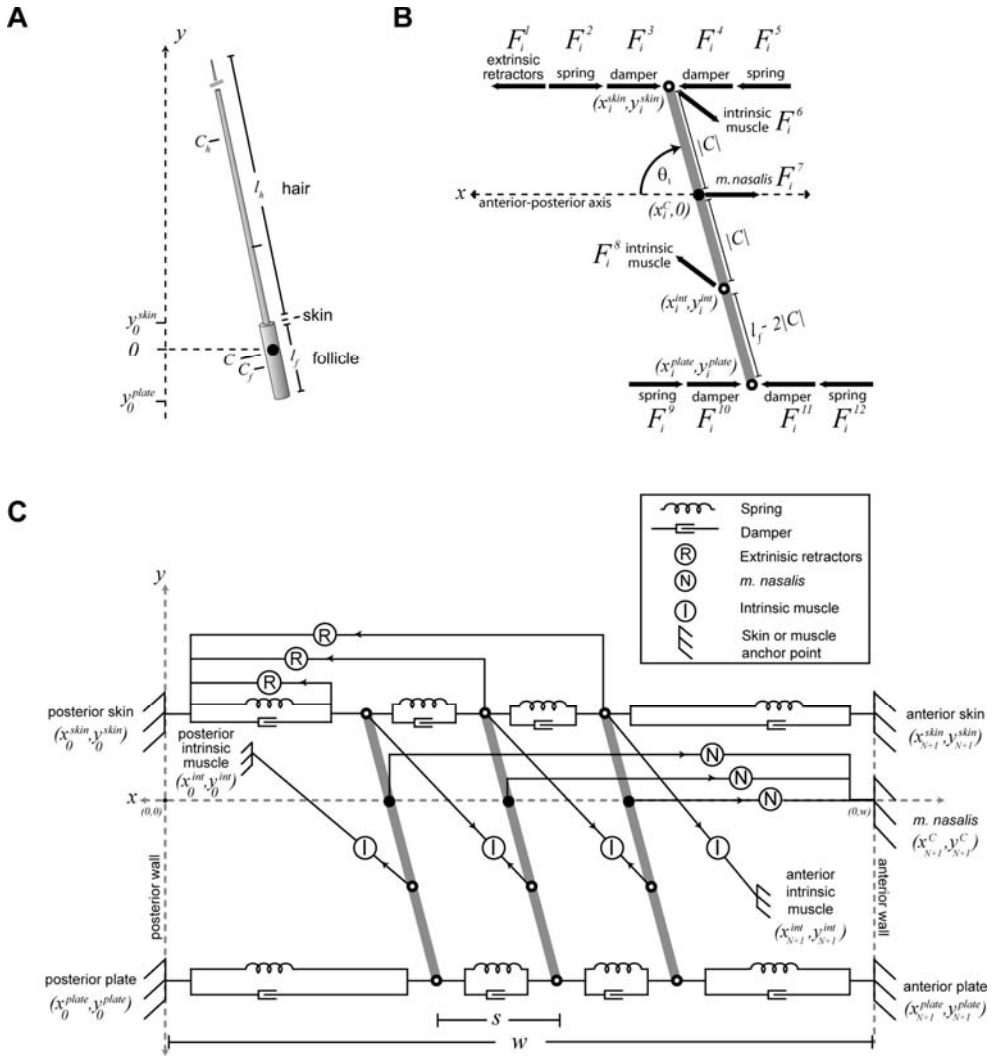

Figure 3.8: Biomechanical model of motor plant.
(A) Rigid body model of a vibrissa unit. The follicle is a rod of length l_f embedded below the skin, with center of mass located at C_f. The hair protrudes from the follicle as a cone of length l_h with center of mass at C_h; the hair is displayed truncated. The composite center of mass is at C and defines the location y = 0. **(B)** Diagram of forces (Table 3.6) and attachment points (Table 3.4) along the i^{th} follicle/vibrissa unit. Circles indicate the location of a muscle attachment point, with the closed circle corresponding to the center of mass. The arrows indicate the approximate direction of the labeled force. The distances between attachment points are given in terms of the depth from the center of mass, *i.e.*, y = 0, and the length of the follicle, l_f. The angle of the follicle/vibrissa unit, θ_i is taken with respect to the A-P axis. **(C)** Schematic of the full mechanical model of a row of 3 vibrissae (Appendix and Tables 3.2 to 3.7), shown in the rest state. The attachment points are illustrated for the springs, dampers, and muscles that correspond to the forces labeled in panel B. The approximate relationship between attachment points is conserved, but the figure is not drawn to scale. Arrows indicate the direction of muscle forces, which point away from the attachment points.

We consider a row of 3 rigid follicle/vibrissa units acted on by muscles and visco-elastic elements that represent the elasticity of the mystacial pad. We model the visco-elastic elements as overdamped springs (Eqn. 8 and 11) that connect the vibrissae to each other and to the ends of the pad. The intrinsic and extrinsic muscles are represented by force actuators whose output is proportional to their |∇EMG| activity with a length-dependent scaling term (Eqn. 17 to 19). We note that the relatively minor D-V component of whisking is ignored, and so we exclude *m. transversus nasi* from the model and take *m. nasolabialis* and *m. maxillolabialis* to act as a single force in the A-P direction. The direction of all force vectors is determined by the geometry of the mystacial pad, *i.e.*, how the various muscles, springs, and dampers are attached, which varies dynamically with the motion of the vibrissae.

Geometric parameters

Parameters related to the morphology of the mystacial pad were measured from dissections performed on 3 rats (Table 3.2). We obtained sagittal sections of the mystacial pad that reveal the spacing and orientation of the follicles (Fig. 3.9). The caudal vibrissae, *i.e.*, C1 to C3, have follicles of approximately l_f = 4 mm in length with a spacing of s = 2 mm. We note that the space between the capsules of adjacent follicles was as little as 200 μm.

This suggests that vibrissae along a single row are sterically constrained to move largely in unison during whisking.

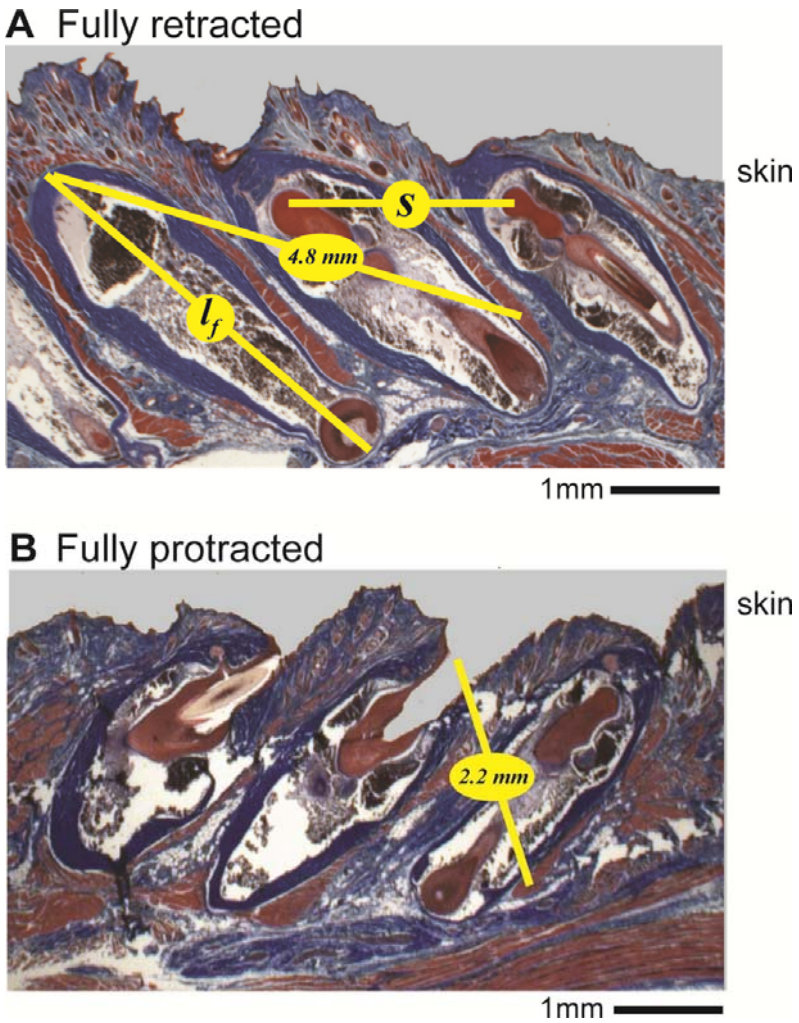

Figure 3.9: Sagittal sections of the follicles for vibrissae C1 through C3.
(A) Section with follicles fixated in a retracted position. Image is posterior to anterior from left to right. The trichrome stain highlights connective tissue in blue and muscle fibers in red. The length of the follicle is denoted l_f and the horizontal spacing of the follicles is denoted s. The 4.8 mm yellow line indicates the estimated path of an intrinsic muscle fiber in the fully retracted state. **(B)** Same as in panel A but with the follicles fixated in a protracted position. The 2.2 mm yellow line indicates the estimated path of an intrinsic muscle fiber in the fully protracted states.

The force generated by a muscle is a function of the deviation from its rest length. This change is expected to be greatest for the relatively short intrinsic muscles. We inferred the fractional change in length of these muscles from histological sections with the vibrissae in either a protracted or retracted position (Fig. 3.9). Note that the protracted and retracted vibrissae are positioned at 135° and 40°, respectively, which closely matches the physiological range of vibrissa motion (Fig. 3.7G). The length of the intrinsic muscle is estimated as twice the distance from the caudal follicle's apex to approximately 70 % of the depth on the rostral follicle's outer capsule, plus approximately 1.0 mm for the muscle to wrap around the follicle (Fig. 3.1C). We estimate a length of 10.5 mm in the retracted position and 5.5 mm in the protracted position (n = 3 rats), with a rest length given by the mean, or 8.0 mm. Therefore, an intrinsic muscle may contract or elongate by ± 30 %. We account for this change with a length-dependent scaling factor applied to all muscle forces (Eqn. 18).

Validation of geometry

We observed in our stimulation experiments that each muscle produces a characteristic ratio of pad movement to vibrissa deflection (Fig. 3.7G). We used our biomechanical model to estimate these ratios by exciting individual simulated muscles over a range of inputs. A constant input was passed into one muscle at a time and the total vibrissa deflection and pad

translation was recorded at steady state. The amplitude of the input was increased until movement exceeded the physiological range; this yielded the full curve of pad translation versus vibrissa deflection (Fig. 3.7G). For each muscle the theoretical curve passes through the cloud of data points obtained from stimulation experiments. This result is determined solely by the geometry of the pad and therefore serves as validation of our geometric parameters.

Relaxation time constant

Passive relaxation of the model vibrissae is determined by the time constant of a set of damped springs (Eqn. 8, 11, and 16). In order to determine this constant, we fit its value to the observed relaxation time course of each muscle from a rat used in the stimulation experiments (Fig. 3.7C to 3.7E). The model was initialized to the deflected vibrissa position from individual muscle stimulations. The model vibrissae were then allowed to passively relax back to their rest position, θ_{rest}, that was set to the observed angle of the vibrissa when unstimulated. The simulated motion of the middle vibrissa was compared to the measured movement of C2 to compute the root mean square (RMS) error (Eqn. 27) for particular values of the time constant which yielded an optimal value of 27 ms that compares favorably to the range of 18 to 26 ms for exponential fits of the relaxation time course (Fig. 3.7C to 3.7E).

Simulated vibrissa movement from EMG data

We validated the model on data from head-fixed experiments, for which we used the measured triphasic |∇EMG| data as input to the model. A set of 20 bouts of 1 s in duration were selected. Protraction of the vibrissae is largely synchronous (Sachdev et al., 2002), so the intrinsic |∇EMG| signal is interpreted as representative of the contraction of individual intrinsic muscles. The geometric parameters and spring time constants were fixed (Table 3.2). The rest position of the vibrissae were determined from epochs when the vibrissae were still. The free parameters were three gain factors, one for each type of muscle, that relate the force produced by a given muscle to the value of the respective |∇EMG| signal (Eqn. 19). These constants were fit to each bout to minimize the RMS error of the estimated vibrissa and pad motion, as illustrated by the 3 examples of figure 3.10. Only one set of parameters was found to minimize the error. The lack of systematic error in the estimated motion suggests that no other muscles play a significant role in driving the motion. Our model achieved an average RMS error of 8.1° for A-P angle and 0.31 mm for pad translation across all 20 bouts, compared to an average range of movement 61° and 1.6 mm for each bout.

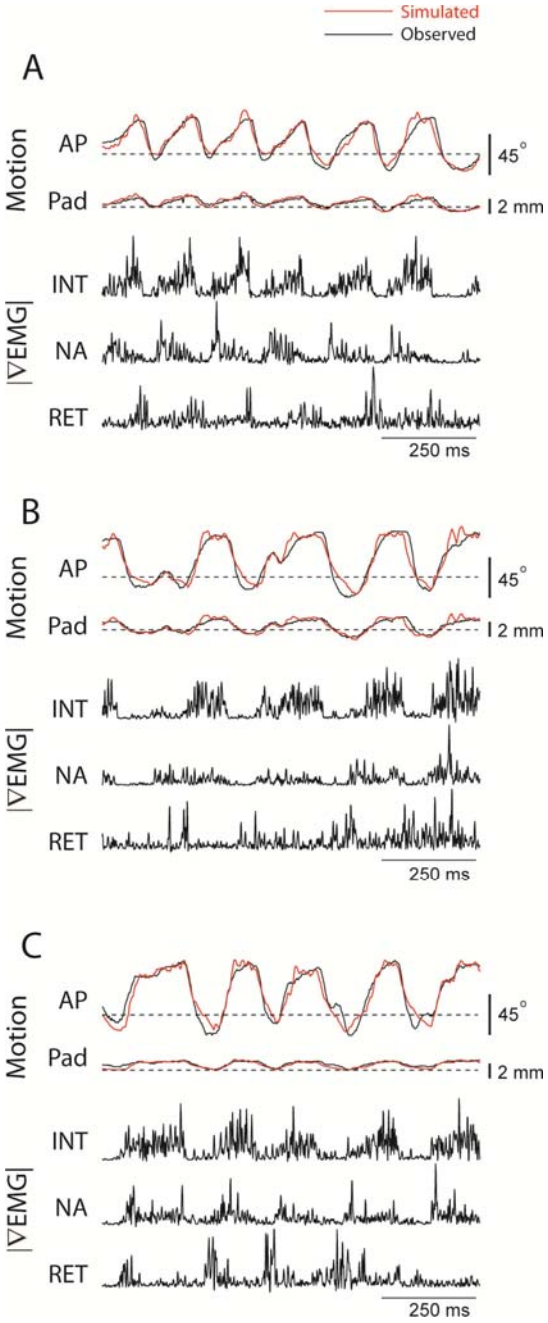

Figure 3.10: Estimation of vibrissa motion from |∇EMG| during head-fixed whisking. **(A to C) |**∇EMG| signals were used as input to the biomechanical model to generate the estimated motion shown in red. The |∇EMG| activity of *m. nasolabialis* was used as the extrinsic retractor signal. All parameters were taken from Table 3.2 except for the muscle gain factors which were fit to the motion data.

We estimated the relative significance of each muscle in driving the vibrissae by re-running each simulation with the optimal parameters but one of the muscles inactivated. We then recorded how much the amplitude of each whisk in the data set (n=102) was reduced by the absence of this muscle (Table 3.3). We find that the intrinsic muscles contribute 71 % of the amplitude of the whisk with the extrinsic retractors contributing 25 % and *m. nasalis* 4 %. We note that this variability is large compared to the variation of average force output for each muscle which only varied by a factor of 3 (Table 3.3). The fact that *m. nasalis* makes a negligible contribution to whisking amplitude is consistent with our stimulation data showing that this muscle produces a relatively small whisker deflection for a given amount of pad movement. Futhermore, by activating early in protraction *m. nasalis* may have less control over the maximum angle which occurs at the end of protraction.

Table 3.3: Sensitivity analysis of free parameters in biomechanical simulations.

Parameter	Mean Value	Mean Output	*Relative Angle Sensitivity	*Relative Pad Sensitivity	†Mean A-P Angle Contribution	†Mean A-P Pad Translation Contribution
g^{INT}	5.1 $N \cdot V^{-1}$	2.7 x 10^{-4} N	2.6	2.1	26.1°	1.0 mm
g^{NA}	0.7 $N \cdot V^{-1}$	0.9 x 10^{-4} N	0.2	0.9	1.4°	0.3 mm
g^{RET}	2.9 $N \cdot V^{-1}$	2.1 x 10^{-4} N	1.0	1.6	9.1°	0.6 mm

* Sensitivity is defined by Equations 28 and 29.

† Mean reduction in amplitude when muscle force is set to 0.

Sensitivity Analysis

We determined the sensitivity of motion of the vibrissae and mystacial pad to changes in the gain parameters g^{INT}, g^{NA}, and g^{RET} (Table 3.3). Our analysis used a measure that compares the normalized RMS error between the calculated and measured motion of the vibrissae and the mystacial pad (Eqs. 28 and 29). The sensitivity may be interpreted as the relative impact of a given muscle group on the motion. We find that the intrinsic muscles have the greatest impact on both motion of the vibrissae and the pad, while the retractor muscles have less effect on vibrissa motion but near equal effect on motion of the pad. The protractor *m. nasolabialis* has little impact on motion of the vibrissae but significant impact on motion of the pad.

Application of the Model: Constraints on Whisking Kinematics

Motivated by evidence that the range of whisking amplitudes is diminished for large offset-angles and high values of whisking frequency (Carvell and Simons, 1995; Berg and Kleinfeld, 2003a; Knutsen et al., 2006a), we analyzed the available range of whisk amplitudes and set-points, defined here as the point of maximal retraction, within the context of our model. Our strategy was to use all possible realistic patterns of muscle activity as input for the model in order to determine the bounds on its range of motion. The waveforms for the simulated neuromuscular input were derived from the average waveform of the |∇EMG| data for individual muscles used in figure 3.4. We re-computed the average waveform with each |∇EMG| signal aligned on its own peak rather than the peak of protraction. The latter method can overestimate the overlap in timing of different muscles. These waveforms were then scaled and given a baseline offset (Fig. 3.11A). All possible amplitudes and offsets were tested up to a bound set by the observed physiological movements (Fig. 3.7G), *i.e.*, a maximum of 40° for retraction, 140° for protraction, and 3.0 mm for anterior translation of the mystacial pad. The peaks of the waveforms for the different muscles were staggered to match the phase delay observed in behavior (Fig. 3.5). Different frequencies of input were tested by re-scaling the input signals in time. Simulations were run for 1 s and the range of motion was assessed from the final whisk cycle of each trial.

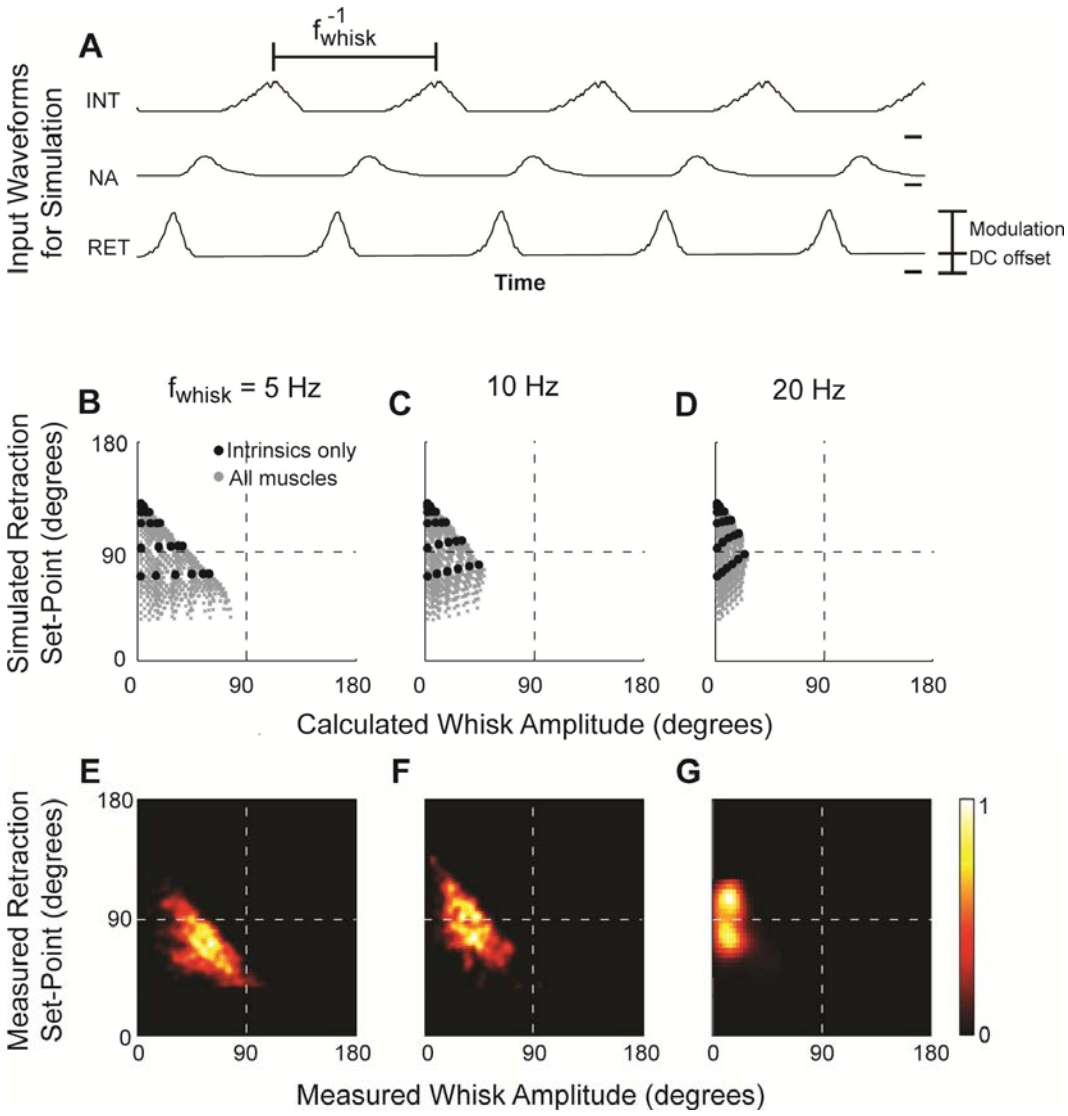

Figure 3.11: Biomechanical constraints on whisking kinematics compared to behavioral repertoire.
(A) Illustration of input signals. The modulation and constant offset of each muscle as well as the overall whisking frequency, f_{whisk} , were varied to determine the bounds on vibrissa motion. A horizontal bar indicates zero-point for each input waveform. **(B to D)** Scatter plot of kinematic parameters produced when each muscle received input at the indicated frequency. Black dots indicate runs where only the intrinsic muscles were active. **(E to G)** Map of kinematic parameters obtained from awake, behaving animals. The color bar represents the density of events. The dashed line in panels B through G represents the rest angle.

Our results show that the range of set-points available to the animal diminishes as the whisking amplitude increases (Figs. 3.11B to 3.11D).

Further, the largest available amplitudes decrease and the available set-points become more protracted as whisking frequency increases. Whisking at a protracted angle produces a stronger relaxation force and allows the intrinsic muscle to contract closer to their angle of maximum torque (Fig. 3.11B), so that only protracted set-points can produce large amplitude whisks at high frequencies.

The calculated range of kinematic parameters was compared with that found in behaving animals (*cf* Figs. 3.11E to 3.11G with 3.11B to 3.11D). We used data from a single head-fixed rat to plot the histogram of amplitude and set-points for whisk cycles with instantaneous frequencies near 5 Hz (n = 761) and 10 Hz (n = 326). Our head-fixed animals did not whisk in the foveal range (15 to 20Hz), so additional data points were obtained from two separate studies. The first data set involved unrestrained rats whisking in air (n = 20, Berg and Kleinfeld, 2003), and the second used unrestrained rats whisking in air during an object localization task (n = 150, unpublished observations by P. M. Knutsen, M. Pietr, and E. Ahissar, for methods see Knusten et al. 2005; 2006). The behavioral data have comparable boundaries to the estimated behavioral limits at all frequencies and exhibit the same trend toward smaller, protracted whisks at higher frequencies. These results support the hypothesis that whisking behavior is limited by mechanical constraints rather than behavioral choice.

An analysis of simulations of the model with the extrinsic muscles inactive shows that the range of set points and amplitudes is more limited. For example, we predict that a rat without extrinsic muscles can no longer whisk at retracted positions. Furthermore, the increase in whisk amplitude gained by using extrinsic muscle diminishes at higher whisking frequencies (Fig. 3.11D).

3.4 Discussion

We report the full pattern of rhythmic muscle activity that drives the A-P motion of the vibrissae and the mystacial pad during exploratory whisking by rat. Four separate muscle groups are observed to activate at three distinct phases during the whisking cycle (Fig. 3.3). *M. nasolabialis* and *m. maxillolabialis* activate during retraction, *m. nasalis* during the early part of protraction, and the intrinsic muscles during late protraction (Fig. 3.4). The precise phase relation is essentially independent of whisking frequency (Fig. 3.5). We further characterized the elastic properties of each muscle group via direct stimulation (Fig. 3.7), as well as the extension of the intrinsic muscle by anatomy (Fig. 3.9). These mechanical properties and the previously described geometry of the follicle and mystacial pad complex (Dorfl, 1982; Wineski, 1985) (Fig. 3.1) informed a mechanical model of the motor plant

(Fig. 3.8). The calculated transformation of motor input into mechanical output, *i.e.*, transformation of |∇EMG| input to motion of the vibrissae and mystacial pad, compares favorably with the measured output. In particular, the model accounts for the amplitude and time course of vibrissa motion during direct muscle stimulation (Fig. 3.7) and behavior (Fig. 3.10), and explains the lack of extrinsic retractor muscle activity during high frequency foveal whisking (Fig. 3.11). Our measurements and model link neuronal motor commands to sensor motion (Fig. 3.10). They emphasize that the biomechanical properties of an active sensory apparatus provide the ultimate constraints on sensory behaviors and thus underlie the interpretation of studies on sensorimotor control.

Whisking in head-fixed versus freely exploring animals

Head-restraint is a useful tool to facilitate vibrissa tracking and to create a controlled behavioral paradigm (Bermejo et al., 1996). As such, this procedure has enabled other difficult behavioral tasks (Gao et al., 2001; Bermejo et al., 2002; Gao et al., 2003c; Friedman et al., 2006a) and intracellular (Crochet and Petersen, 2006) and extracellular (Sachdev et al., 2000; Kleinfeld et al., 2002; Melzer et al., 2006) recording studies. Yet it has been heretofore undocumented how head-restraint may alter whisking behavior. We find that exploratory whisking for head-fixed versus freely exploring animals involves the same pattern of muscle activation (*cf*

Figs. 3.3A and 3.3B). However, the probability densities of whisking frequency for head-fixed versus freely exploring animals have little overlap (Figs. 3.6C and 3.6D). The mean frequency for whisking decreases from 9 Hz for the unrestrained case to 6 Hz for head-fixed animals. In both cases whisking was spectrally pure, *i.e.*, it is characterized by a sharp peak at the whisking frequency in the power spectrum of the $|\nabla EMG|$ (Figs. 3.6E and 3.6F). It remains unclear if the decrease in whisking frequency results from a change in whisking strategy or from the lack of head movements.

Biomechanical constraints on the behavioral repertoire of whisking

The intrinsic muscles are sufficient to produce rhythmic vibrissa motion. The contraction of these muscles, which form a sling around the base of each follicle (Fig. 3.1B), provide the major protraction of the vibrissae (Figs. 3.11A to 3.11D). In the absence of the extrinsic muscles, the concomitant retraction can be effected through passive relaxation of the elastic facial tissue (Figs. 3.11A to 3.11D). Of practical relevance, this form of retraction can be generated by electrically stimulating the facial nerve to induce protraction in anesthetized animals and is referred to as “artificial whisking” (Zucker and Welker, 1969; Brown and Waite, 1974; Szwed et al., 2003a; Arabzadeh et al., 2005; Szwed et al., 2006).

Our biomechanical model sheds light on the limitations of whisking by intrinsic muscles alone. First, the visco-elasticity in the mystacial pad is over-damped, so the vibrissae cannot passively retract beyond their rest angle. This is manifest as a region of parameter space for whisking kinematics that lies behind the rest angle that is accessible only when the model includes extrinsic muscles (Figs. 3.11B to 3.11D). Active retraction by *m. nasolabialis* and *m. maxillolabialis* enables larger amplitude whisks to occur. Secondly, passive relaxation sets an upper bound on the velocity of retraction. With only activation of the intrinsic muscles, the vibrissae must shift their set-point farther forward to increase the elastic tension on the vibrissae. This may explain why high-frequency foveal whisking, which does not involve active retraction (Berg and Kleinfeld, 2003a), has a protracted set-point.

Extrinsic retractor muscles cooperate to control dorsal-ventral motion

The extrinsic retractor muscles are ideally situated to counterbalance each other in the control of the D-V component of vibrissae and mystatial pad motion, with the fibers of *m. nasolabialis* running superficially and ventrally as they invade the pad and those of *m. maxillolabialis* entering deep and dorsally. Anatomically, the fibers intermingle and fuse as they run superficially between the vibrissae (Dorfl, 1982). Direct excitation of these muscles demonstrates that neither one is sufficient to produce a strictly

posterior movement (Figs. 3.7B). Only a balanced stimulation, resulting in a linear summation of their action, results in a purely posterior retraction. The concomitant activation of both muscles during whisking (Figs. 3.3 to 3.5) suggests that the animal employs such a summation.

Relation of the model of the motor plant to sensation

Our model considers motion of the follicle and vibrissa as a single unit. In fact, the vibrissa can move within the follicle, as will occur during contact of a vibrissa with an object (Rice et al., 1986). Such movement leads to activation of pressure sensitive trigeminal ganglion neurons that innervate the apical (skin) and the distal (plate) ends of the follicle (Fig. 3.1) (Zucker and Welker, 1969; Simons et al., 1990; Waite and Jacquin, 1992; Szwed et al., 2003a; Leiser and Moxon, 2006). In principle, differential activation of these two groups of receptors provides a means to code both the angle (Curtis and Kleinfeld, 2005) and radial distance (Solomon and Hartmann, 2006; Szwed et al., 2006) of the contact point. A second form of sensory signaling concerns the angular position of the follicle in the absence of vibrissa contact (Fee et al., 1997; Szwed et al., 2003a; Ganguly and Kleinfeld, 2004). This proprioceptive-like reference signal was shown to result from peripheral reafference (Fee et al., 1997). It may, in principle, be generated by periodic compression and distortion of the follicles during the whisk cycle. The model of the motor plant presented here provides the substrate for a full model that

incorporates the dynamics of the follicle/vibrissa complex (Mitchinson et al., 2004) and bending properties of the vibrissae (Hartmann et al., 2003; Andermann et al., 2004).

Motor control of exploratory whisking

The results of this study bear on the neural circuitry for pattern generation of whisking. Lesion studies have shown that whisking persists after sensory nerve transection (Welker, 1964; Gao et al., 2001; Berg and Kleinfeld, 2003a; Berg et al., 2006), contralateral motor cortex ablation (Gao et al., 2003c), and extensive decerebration (Welker, 1964). These results argue for a brainstem central pattern generator to drive rhythmic whisking. It was previously proposed that this central pattern generator consists of two coupled oscillators, consistent with a constant phase relationship between the intrinsic muscles and *m. nasolabiali*s across frequencies (Berg and Kleinfeld, 2003a). We now find that such a constant phase relation holds for all of the muscles involved in whisking (Fig. 3.5), and thus revise the original hypothesis to include three coupled oscillators that correspond to the three phases of muscle activity.

Many rhythmic behaviors in rat have been reported to alternately couple and decouple to whisking. These include sniffing and head movements (Welker, 1964), breathing (Welzl and Bures, 1977), and

mastication (Travers et al., 1997). This suggests that the brainstem contains multiple pattern generators, each for a different motor action. These oscillators may phase-lock or decouple in a dynamic fashion that depends on their synaptic interactions (Kopell and Ermentrout, 1986) and on the overall oral-facial task of the animal.

The present results further highlight the need to understand motor control in terms of the activation of individual muscle groups. In principle, retraction of the vibrissae may involve any combination of activation of *m. nasolabialis* and *m. maxillolabialis* along with passive relaxation of the mystacial pad. This confound is removed by recording the $|\nabla EMG|$ for each muscle. This approach is also crucial for interpreting the results of studies that make use of intracortical microstimulation of vibrissa motor cortex (vM1), which may evoke a non-behavioral pattern of muscle activation. Rhythmic stimulation of vM1 simultaneously activates *m. nasolabialis* and the intrinsic muscles, which normally activate in anti-phase, with the retractor muscle dominating the evoked movement (Berg and Kleinfeld, 2003a). Further, it remains to be shown whether rhythmic vibrissa motion produced by tonic stimulation of vM1 in anesthetized rats (Cramer and Keller, 2006b) or induced rhythmic activity in vM1 (Castro-Alamancos, 2006) produces the 3.phase pattern of muscle activation observed in awake, behaving rats (Figs. 3.3 and 3.4). A myotopic map of vM1 would clarify how the control of whisking is

segregated in cortex, *e.g.*, how do “rhythmic whisking” versus “retraction-facial” areas correspond to different patterns of intrinsic and extrinsic muscle activation (Haiss and Schwarz, 2005b)?

3.4 Acknowledgements

Part of this dissertation follows from work that is currently published in:

Hill DN, Bermejo R, Zeigler HP, Kleinfeld D. Biomechanics of the vibrissa motor plant in rat: Rhythmic whisking consists of triphasic neuromuscular activity. J Neurosci. 28(13):3438-55 (2008)

This material is included here with the generous consent of all coauthors and permission of the journal. We thank L. E. Wineski for instruction on the dissection of the facial muscles, R. Lieber for discussions on muscle physiology, V. Z. Lawson and J. B. Swartz for training the head-fixed animals, C. Granzella for assistance with the simulations, R. W. Berg for assistance with the analysis of data, L. E. Wineski, H. J. Karten and D. Golomb for critical comments on this work, and P. M. Knutsen, M. Pietr and E. Ahissar for sharing data on high-frequency whisking. This study was supported by grants from the Human Frontiers for Scientific Progress (RGP43/2004 to DK), the United States-Israeli Binational Science Foundation (2003222 to DK), and the National Institute of Neurological Disease and Stroke (NS37263 to HPZ and NS058668 to DK) and fellowships to DH through the National Science

Foundation Integrative Graduate Education and Research Traineeship and National Research Service Award programs.

3.5 Model Appendix

Here we define the equations that describe translation and rotation of the vibrissa along the A-P axis (Fig. 3.8). The D-V component of whisking, as well as movement along the length of the shaft, are ignored.

Follicle/Vibrissa Unit

A follicle/vibrissa unit consists of a hair that protrudes from a follicle. We take both components to be straight, rigid bodies (Fig. 3.8A). The tips of real vibrissae are curved and flexible, but our approximation is valid for motion at the base of the shaft. The follicle is modeled as a rod of length l_f and mass M_f that is embedded below the skin. The hair is modeled as a cone of length l_h and mass M_h with its base at the skin's surface. We approximate a follicle/vibrissa unit as infinitely thin, so we consider its moment of inertia about the A-P axis only. The unit has a center of mass, C, and moment of inertia with respect to the center of mass, I, that is derived from the

corresponding values for the hair and follicle alone, denoted by the subscripts *h* and *f*, respectively (Fig. 3.8A):

(1) $$C_h = \frac{1}{4} l_h$$

(2) $$I_h = \frac{3}{80} M_h l_h^2$$

(3) $$C_f = -\frac{1}{2} l_f$$

(4) $$I_f = \frac{1}{12} M_f l_f^2$$

The center of mass of the entire unit is the weighted average of C_h and C_f, *i.e.*:

(5) $$C = \frac{1}{M_f + M_h}\left(M_f C_f + M_h C_h\right)$$
$$\simeq -1.43 \text{ mm relative to the level of the skin}$$

where we substituted values from Table 3.2. By the parallel axis theorem, we can write the moment of inertia of the follicle/vibrissa unit as:

(6) $$I = I_f + M_f (C - C_f)^2 + I_h + M_h (C - C_h)^2$$
$$\simeq 112 \text{ mg} \cdot \text{mm}^2$$

The hair contributes negligibly to the mass of the vibrissa/follicle unit, but its length dominates the moment of inertia. With the hair removed, the moment of inertia of the follicle alone is 13.3 mg•mm^2.

Enumeration of forces that act on each vibrissa

The vibrissae are driven actively by the contraction of facial muscles and passively by the visco-elastic properties of the mystacial pad. We enumerate these forces and specify their attachment points along the follicle. The calculation of the magnitude and direction of each force requires a model for the geometry of the pad as a whole, so we defer these equations to a later section. In the discussion below, we denote the j^{th} force on the i^{th} follicle/vibrissa as F_i^j.

First we consider the visco-elastic properties of the mystacial pad. We observe that a deflected vibrissa passively returns to a rest position and rest angle without oscillation (Figs. 3.7C to 3.7E). The simplest model that generates this behavior consists of two sets of over-damped springs that return the top and bottom of the follicle to different A-P rest positions. At the level of the skin, there are two springs, with forces F_i^2 and F_i^5, and two dampers, with forces F_i^3 and F_i^4, that act on the point (x_i^{skin}, y_i^{skin}) (Fig. 3.8B). At the plate, there are two springs, with forces F_i^9 and F_i^{12}, and two dampers, with forces F_i^{10} and F_i^{11}, that act on the point (x_i^{skin}, y_i^{skin}).

We include 4 muscles that directly manipulate each vibrissa unit. First, we combine the retractor muscles *m. nasolabialis* and *m. maxillolabialis* into a

single force, denoted F_i^1. This is motivated by the observations that the two muscles activate concurrently (Figs. 3.4 and 3.5) and that only a balanced excitation leads to motion strictly along the A-P axis (Fig. 3.7B). The extrinsic retractor muscles run just below the skin. Their fibers do not necessarily attach directly to the follicle, but the force they produce on the vibrissae is directed at the level of the skin. We therefore place the attachment point for this muscle at the top of the follicle, at the point (x_i^{skin}, y_i^{skin}).

The fibers of *m. nasalis,* the caudal extrinsic muscle, run deep to the follicle. Yet the muscle produces a minimal angular deflection of the vibrissae when stimulated (Fig. 3.7G) which is consistent with the net force of *m. nasalis*, denoted F_i^7, acting at the center of mass of the follicle/vibrissa unit. We thus attach *m. nasalis* to the center of mass of the unit (Fig. 3.8C).

Each vibrissa is also actively driven by two intrinsic muscles that correspond to forces F_i^6 and F_i^8. Each intrinsic muscle spans two adjacent vibrissae, so the direction of force is expected to be oblique to the A-P axis (Fig. 3.1B). The more superficial attachment point is at the level of the skin, (x_i^{skin}, y_i^{skin}). We set the other attachment point to twice the depth of the center of mass, at the point $(x_i^{\text{int}}, y_i^{\text{int}})$. This is consistent with the anatomical location and implies that the intrinsic muscles exert an equal torque on the follicle.

In total, the 12 forces act on each follicle at 4 unique attachment points. Additionally, we constrain the center of mass of each vibrissa to move along the A-P axis so that $y_i^C = 0 \ \forall \ i$. The location, x_i^C, and speed, $\dot{x}_i^C$, of the centers of mass of each vibrissa and the angle, θ_i, and angular velocity, $\dot{\theta}_i$, of each vibrissa about its center of mass comprise the state of the model (Fig. 3.8B). The position and velocity of each of the four attachment points can be derived from these state variables (Table 3.4).

Table 3.4: Equations for position and velocity of follicle attachment points.

Attachment	Position		Velocity	
	A-P Axis	Depth	A-P Axis	Depth
(x^{skin}, y^{skin})	$x^C + C\cos(\theta)$	$-C\sin(\theta)$	$\dot{x}^C - C\sin(\theta)\dot{\theta}$	$-C\cos(\theta)\dot{\theta}$
$(x^{\text{int}}, y^{\text{int}})$	$x^C - C\cos(\theta)$	$C\sin(\theta)$	$\dot{x}^C + C\sin(\theta)\dot{\theta}$	$C\cos(\theta)\dot{\theta}$
(x^{plate}, y^{plate})	$x^C + (l_f + C)$ co	$-(C + l_f)\sin(\theta$	$\dot{x}^C - (C + l_f)\sin(\theta)$	$-(C + l_f)\cos(\theta)$

Geometry of the vibrissae in the mystacial pad

Each of the forces acts between two attachment points, whose locations determine the direction and scale the magnitude of the associated force. We define the attachment points associated with each force by

considering a row of *N* identical vibrissae (Fig. 3.8C) (Table 3.5), where the vibrissae are numbered from *1* (posterior) to *N* (anterior), and are separated by a distance s at rest. We illustrate the case when *N* = 3 as this is the minimum case that includes a vibrissa that is coupled to two neighboring vibrissae by connective tissue and intrinsic muscles along with two vibrissae that are coupled to anchors by connective tissue and intrinsic muscles. The attachment points $A^{i,j}$ and $B^{i,j}$ associated with the force F_i^j are listed in Table 3.6; the attachment point's coordinates are denoted by $(A_x^{i,j}, A_y^{i,j})$ and $(B_x^{i,j}, B_y^{i,j})$ and the force is directed toward the point $A^{i,j}$.

Table 3.5: Equations for position of anchor points.

Anchor point	A-P axis	Depth axis
(x_0^{skin}, y_0^{skin})	0	$-C\sin(\theta^{rest})$
$(x_0^{\text{int}}, y_0^{\text{int}})$	$x_1^{rest} + C\cos(\theta^{rest}) - 2s$	$-C\sin(\theta^{rest})$
$(x_0^{plate}, y_0^{plate})$	0	$-(C + l_f)\sin(\theta^{rest})$
$(x_{N+1}^{skin}, y_{N+1}^{skin})$	w	$-C\sin(\theta^{rest})$
$(x_{N+1}^{C}, y_{N+1}^{C})$	w	0
$(x_{N+1}^{\text{int}}, y_{N+1}^{\text{int}})$	$x_N^{rest} + (l_f + C)\cos(\theta^{rest}) + 2s$	$-(C + l_f)\sin(\theta^{rest})$
$(x_{N+1}^{plate}, y_{N+1}^{plate})$	w	$-(C + l_f)\sin(\theta^{rest})$

Table 3.6: Forces and attachment point for each force on the i^{th} vibrissa.

Force	Description	To $(A^{i,j})$	From $(B^{i,j})$
F_i^1	extrinsic retractor muscles	(x_i^{skin}, y_i^{skin})	(x_0^{skin}, y_0^{skin})
F_i^2	posterior skin spring	(x_i^{skin}, y_i^{skin})	$(x_{i-1}^{skin}, y_{i-1}^{skin})$
F_i^3	posterior skin damper	(x_i^{skin}, y_i^{skin})	$(x_{i-1}^{skin}, y_{i-1}^{skin})$
F_i^4	anterior skin damper	(x_i^{skin}, y_i^{skin})	$(x_{i+1}^{skin}, y_{i+1}^{skin})$
F_i^5	anterior skin spring	(x_i^{skin}, y_i^{skin})	$(x_{i+1}^{skin}, y_{i+1}^{skin})$
F_i^6	superficial intrinsic muscle	(x_i^{skin}, y_i^{skin}) *	$(x_{i+1}^{\text{int}}, y_{i+1}^{\text{int}})$
F_i^7	*m. nasalis*	(x_i^C, y_i^C)	(x_{i+1}^C, y_{i+1}^C)
F_i^8	deep intrinsic muscle	$(x_i^{\text{int}}, y_i^{\text{int}})$	$(x_{i-1}^{skin}, y_{i-1}^{skin})$
F_i^9	posterior plate spring	$(x_i^{plate}, y_i^{plate})$	$(x_{i-1}^{plate}, y_{i-1}^{plate})$
F_i^{10}	posterior plate damper	$(x_i^{plate}, y_i^{plate})$	$(x_{i-1}^{plate}, y_{i-1}^{plate})$
F_i^{11}	anterior plate damper	$(x_i^{plate}, y_i^{plate})$	$(x_{i+1}^{plate}, y_{i+1}^{plate})$
F_i^{12}	anterior plate spring	$(x_i^{plate}, y_i^{plate})$	$(x_{i+1}^{plate}, y_{i+1}^{plate})$

* If *i=1*, this attachment point is the anchor $(x_0^{\text{int}}, y_0^{\text{int}})$.

Several components in our model attach to immobile anchor points. We use the subscripts *0* and *N+1* to designate anchors that lie posterior or anterior to the row of vibrissae, respectively. The extrinsic muscles and the elastic tissue at either end of the row of vibrissae have attachment points external to the pad, represented by posterior and anterior walls. The separation of these walls is the measured length of the face, *w*. The depth of these attachment points is set so that the attached components lie horizontally when the vibrissae are at their rest angle, θ_i^{rest}. Additionally, the intrinsic muscles at either end of a row of vibrissae have an attachment point embedded within the pad (Figs. 3.1C and 3.8C). We placed the caudal intrinsic muscle anchor, $(x_0^{\text{int}}, y_0^{\text{int}})$, at the level of the skin and the anterior intrinsic muscle anchor, $(x_{N+1}^{\text{int}}, y_{N+1}^{\text{int}})$, at the level of the plate. Horizontally, the intrinsic muscle anchor points are positioned a distance of 2*s* from the rest position of their respective follicle attachment points.

Specification of visco-elastic forces

Damped restoring forces are generated by a parallel combination of a spring with a damper (Fig. 3.8C). A spring (F_i^2, F_i^5, F_i^9, and F_i^{12}) produces a force proportional to its displacement from its rest position. The distance between the two attachment points associated with spring force F_i^j is:

(7) $$d_i^j = \sqrt{\left(A_x^{i,j} - B_x^{i,j}\right)^2 + \left(A_y^{i,j} - B_y^{i,j}\right)^2}$$

Therefore, the magnitude of the force generated by a spring is:

(8) $$\left\| F_i^j \right\| = \kappa_i^j \left| d_i^j - d_i^{j,rest} \right|$$

where κ_i^j is a proportionality constant and $d_i^{j,rest}$ is the rest length of the spring. The sign of the force opposes displacement from rest. The constants κ_i^j were determined from the results of muscle stimulation experiments (Figs. 3.7C to 3.7E). The rest length of each spring was set so that the springs have no tension when the vibrissa/follicle units are in their rest state. This corresponds to: (*i*) all of the vibrissae are at the angle θ_i^{rest}; (*ii*) adjacent vibrissae are separated by the distance *s*; and (*iii*) the entire row of vibrissae is centered between the anterior and posterior walls. The rest position of the center of mass for the i^{th} vibrissa is therefore:

(9) $$x_i^{rest} = si + \frac{w - sN}{2}.$$

The springs lie horizontally when the vibrissae are at their rest angle, so that the rest length of a spring that connects two follicles is *s.* Springs that have an attachment point on an anchor have a rest length chosen to center the row of vibrissae between the two walls (Table 3.7).

Table 3.7: Rest lengths of model springs.

Attachment points	Symbol	Rest length
Two follicles at skin	$d_i^{2,rest}$; $d_{i-1}^{5,rest}$ for $2 \le i \le N$	s
Two follicles at plate	$d_i^{9,rest}$; $d_{i-1}^{12,rest}$ for $2 \le i \le N$	s
Follicle to posterior skin anchor	$d_1^{2,rest}$	$\frac{w-2(N-1)s}{2}+C\cos(\theta^{rest})$
Follicle to anterior plate anchor	$d_N^{12,rest}$	$\frac{w-2(N-1)s}{2}+C\cos(\theta^{rest})$
Follicle to posterior plate anchor	$d_1^{9,rest}$	$\frac{w-2(N-1)s}{2}-C\cos(\theta^{rest})$
Follicle to anterior skin anchor	$d_N^{5,rest}$	$\frac{w-2(N-1)s}{2}-C\cos(\theta^{rest})$

A damper (F_i^3, F_i^4, F_i^{10}, and F_i^{11}) produces a force proportional to the velocity at which it changes length. The speed at which the attachment points associated with damper force F_i^j are moving with respect to each other is:

(10) $$\left|\dot{x}_i^j\right| = \sqrt{\left(\dot{A}_x^{i,j} - \dot{B}_x^{i,j}\right)^2 + \left(\dot{A}_y^{i,j} - \dot{B}_y^{i,j}\right)^2}$$

These derivatives are calculated for follicle attachment points and are zero for anchor points (Table 3.4). The force generated by a damper is then:

(11) $$\left\|F_i^j\right\| = \zeta_i^j \left|\dot{x}_i^j\right|$$

where ζ_i^j is a proportionality constant associated with this damper and the sign is chosen to oppose motion.

We assume the visco-elastic properties of the mystacial pad are homogeneous. The individual spring and damper constants are normalized by rest length, *i.e.*,:

(12) $$\kappa_i^j = \kappa \frac{w}{d_i^{j,rest}}$$

(13) $$\zeta_i^j = \zeta \frac{w}{d_i^{j,rest}}$$

As a result, the relatively short springs and dampers between follicles are much stiffer than the relatively long springs and dampers between the follicles and the ends of the pad. The overall scale factors, *i.e.*, κ for the spring constants and ζ for the damper constants, are fit to muscle stimulation experiments (Figs. 3.7C to 3.7E). The results from these measurements imply that the mystacial pad is over-damped, so that:

(14) $$\frac{\zeta^2}{4\kappa} > N(M_h + M_f)$$

A linear over-damped system is not greatly sensitive to the exact value of this ratio, so we arbitrarily chose:

(15) $$\frac{\zeta^2}{4\kappa} = 4N(M_h + M_f).$$

This leaves only a single free parameter $\tau^{relaxation}$ which is the time constant of the exponential decay to rest. Its value is given by:

(16) $$\tau^{relaxation} = \frac{2N(M_h + M_f)}{\zeta - \sqrt{\zeta^2 - 4\kappa N(M_h + M_f)}}$$

Specification of muscle forces

The force output of the muscles (F_i^1, F_i^6, F_i^7, and F_i^8) is a function of its electrical activation. We denote the electrical activity of a particular muscle as $\left|\nabla \mathrm{EMG}^{\gamma}\right|(t)$ where γ identifies the muscle type and we assume each muscle of the same type activates identically.

Each muscle is at its rest length when the vibrissae are in their rest position. We calculate the length-dependent variation in force in terms of the muscle's length as a fraction of its rest length:

(17) $$z_i^j = \frac{d_i^j}{d_i^{j,rest}}.$$

We scale the muscle's force by a function, $f\left(z_i^j\right)$, which is a simplified piece-wise linear function for the length-dependence in type 2B fibers in rats (Galler et al., 1996), the fiber type that predominates in the mystacial pad (Jin et al., 2004). Thus:

(18) $$f(z)=\begin{cases}0 & \text{if } z<0.55\\ 4(z-0.55) & \text{if } 0.55\le z<0.80\\ 1 & \text{if } 0.80\le z<1.20\\ -4(z-1.45) & \text{if } 1.20\le z<1.45\\ 0 & \text{if } z>1.45\end{cases}$$

The force output of a given muscle is:

(19) $$|F_i^j(t)|=g^\gamma f\left(z_i^j\right)\left|\nabla \text{EMG}^\gamma\right|(t)$$

where the scale-factor, g^γ, is chosen to fit to the vibrissa motion data from the concurrently recorded |∇EMG| data (Fig. 3.11). Note that we ignored the velocity-dependence of the muscle force.

Equations of motion

The dynamics are expressed in terms of the A-P translation of each center of mass, x_i^C, and the angle of each vibrissa, θ_i. Translation is found from summing the horizontal component of each of the 12 individual forces that act on the *i*th follicle at each time step. The direction of a force F_i^j is along the line connecting its two attachment points. This angle with respect to the A-P axis is:

(20) $$\angle F_i^j=\arctan\left(\frac{A_y^{i,j}-B_y^{i,j}}{A_x^{i,j}-B_x^{i,j}}\right).$$

The center of mass for each vibrissa responds to the component of each force along the A-P axis (Fig. 3.8B), *i.e.*:

(21) $$(M_h + M_f)\ddot{x}_i = \sum_{j=1}^{12} F_i^j \cos(\angle F_i^j)$$

Angular motion is determined by the net torque about the center of mass of the follicle/vibrissa unit (Figs. 3.8A and 3.8C). The torque is the product of the moment arm and the component of the force that lies perpendicularly to the follicle (Figs. 3.8B and 3.11A), *i.e.*:

(22) $$I\ddot{\theta}_i = \sum_{j=1}^{12} r_i^j F_i^j \sin(\theta_i - \angle F_i^j)$$

where r_i^j is the distance between center of mass $(x_{i,}^C 0)$ and the point where F_i^j acts on the vibrissa, A_i^j. The attachment points move with the vibrissae and are recalculated at each time step (Table 3.4). This movement, in turn, determines the magnitude and direction of each force at the next time step.

Initial conditions

The vibrissa start from rest, with initial displacements and velocities given by:

(23) $$x_i^C(t_0) = x_i^{rest}$$

(24) $$\dot{x}_i^C(t_0) = 0$$

(25) $$\theta_i(t_0) = \theta^{rest}$$

(26) $$\dot{\theta}_i(t_0) = 0$$

Recall that the y-position of the center of mass is fixed at 0.

Parameter estimation and sensitivity analysis

The time constant $\tau^{\text{relaxation}}$ and muscle gain parameters g^{γ} were optimized to fit motion data from stimulation experiments and head-fixed whisking as described in the text. The optimal values were chosen to minimize the normalized sum of the RMS error of the simulated angle E^{θ_2} and the RMS error of the simulated pad translation E^{x_2}:

(27) $$E = \frac{E^{\theta_2}}{\sqrt{\left\langle \left(\theta_{measured} - \theta_{rest}\right)^2 \right\rangle}} + \frac{E^{x_2}}{\sqrt{\left\langle \left(x_{measured} - x_{rest}\right)^2 \right\rangle}}$$

where $\theta_{measured}$ and $x_{measured}$ are the observed vibrissa angle and pad translation, respectively, and $\langle \cdot \rangle$ denotes an average over the entire whisking bout. A global numerical search of parameter space verified that there was only one minimum in the error (Eq. 27) for each bout, which was found exactly through gradient descent. A detailed inspection of the parameter space suggests that increases in error subsequent to a change in one gain parameter can be partially offset by a change in another. For example, an increase in g^{INT} is partially offset by an increase in g^{RET}.

To assess the sensitivity of the model to a change in a single gain parameter g^{γ} we estimated the quantities:

(28) $$\frac{\Delta E^{\theta_2}}{\Delta g^{\tau}} \cong \sqrt{\frac{1}{2}\frac{\partial^2 E^{\theta_2}}{\partial (g^{\tau})^2}\frac{(g^{\tau}_{opt})^2}{E^{\theta_2}_{opt}}}$$

and

(29) $$\frac{\Delta E^{x_2}}{\Delta g^{\tau}} \cong \sqrt{\frac{1}{2}\frac{\partial^2 E^{x_2}}{\partial (g^{\tau})^2}\frac{(g^{\tau}_{opt})^2}{E^{x_2}_{opt}}}$$

where the subscripted variables are the values found during optimization. The expressions on the right are the square root of the normalized second-order term of the Taylor expansion of the error function. The first-order term is zero because the parameters are optimal. Values for Equations 28 and 29 were estimated by first varying the optimal parameters by $\pm$ 10 % and $\pm$ 20 % and then using a spline to estimate the second derivative of E^{θ_2} and E^{x_2} as a function of g^{γ} (Table 3.3).

Comparison with observed pad translation

Our experimental measurement of translation of the mystacial pad refers to points where the vibrissa exits the skin. Therefore, we report the estimated translation at a height, h, above the center of mass (Fig. 3.8C):

(30) $$x_i^{pad} = x_i^C + h / \tan(\pi - \theta_i)$$

The value of h is approximately the height of the skin anchor points, but was adjusted by up to 0.25 mm in order to fit the measured translation.

Chapter 4 - Cortical representation of whisking in the behaving rat

Sensory organs are commonly subject to motor control. In such cases, the convergence of sensory and motor signals in the nervous system is required to form stable percepts from moving sensors. Furthermore, the convergence of sensory and motor signals is required to inform behavioral strategies for active sensing. Here we examine how self-generated motion of tactile hairs is represented in the vibrissa region of primary motor cortex (vM1) in rats. We ask how accurately the trajectories of vibrissa motion can be reconstructed from neural activity and whether such information originates from sensory or motor signals. We recorded spike trains of single units in vM1 concurrently with facial muscle activity and vibrissa position in head-restrained and free-ranging rats that are freely whisking. Neural activity was found to correlate with whisking behavior on both fast (*i.e.,* whisk cycle phase) and slow (*i.e.,* amplitude and angular midpoint) timescales. We quantify how well this activity reports vibrissa position in terms of an ideal observer analysis of neural population activity. The trajectories of vibrissa motion can be reconstructed accurately from populations of less than 500 neurons in vM1 in real time. We then compare the representation of self-motion in vM1 to that in the barrel cortex region of primary somatosensory cortex (S1). We find that phase is preferentially encoded in S1 while midpoint and amplitude are preferentially encoded in vM1. The presence of self-

motion signals in vM1 indicates this area may be involved in feedback control of whisking behavior and that it may act as a source of efferent copy signals for other areas of the brain.

4.1 Introduction

Active sensing necessitates the nervous system represent self-generated motion. This is required to form stable percepts from moving sensors and to allow the correction of improperly executed motor commands. Information about self-motion arrives from both sensory and motor sources and how the nervous system represents and integrates thee information from these sources remains an open issue. An understanding of these processes is of vital interest to prosthetics research and in the development of therapies for impairments of motor control.

The rat vibrissa system offers an ideal model for the study of active sensing. Rhythmic whisking behavior has a single degree of freedom (Bermejo et al., 2005) with a limited behavioral repertoire (Knutsen et al., 2008) and a well-defined set of mechanical constraints (Hill et al., 2008). Anatomically, the system is composed of a hierarchy of sensory-motor loops (Kleinfeld et al., 1999) that allow the investigation of sensory-motor transformations at many levels of neural processing. The muscles involved in

rhythmic whisking lack spindles so that there is a single source of sensory feedback into the system via the infra-orbital branch of the trigeminal nerve (Rice and Arvidsson, 1991). There exist several sensory behavioral paradigms in both mice and rats (Knutsen et al., 2006b; Mehta et al., 2007; Curtis and Kleinfeld, 2009) that provide for the use of advanced opto-genetic physiological techniques in awake, behaving animals (Aronoff and Petersen, 2006).

Despite the advantages of this system, relatively little is known about the representation of self-motion in the vibrissa region of primary motor cortex (vM1). This region is somatotopically organized into a coarse vibrissa map (Hoffer et al., 2003; Brecht et al., 2004) and highly interconnected with the corresponding region in primary sensory cortex (S1) (Miyashita et al., 1994a; Izraeli and Porter, 1995a; Zhang and Deschenes, 1997; Veinante and Deschenes, 2003; Alloway et al., 2004; Rocco and Brumberg, 2007) to make it an obvious candidate circuit for the study of sensory-motor transformations in cortex. Most of our knowledge of vM1 comes from a series of stimulation and ablation experiments that demonstrate whisking persists in the presence of unilateral (Gao et al., 2003b) and bilateral (Semba and Komisaruk, 1984b) ablation of vM1. In addition, rhythmic (Berg and Kleinfeld, 2003b) and tonic (Haiss and Schwarz, 2005a; Cramer and Keller, 2006a) stimulation of vM1 can generate rhythmic vibrissa deflections in anesthetized rats. The local

field potential in vM1 can lock to whisking behavior (Ahrens and Kleinfeld, 2004) and can also predict the initiation of a whisking bout (Friedman et al., 2006b), but to our knowledge, there has been only one study to compare spiking activity in vM1 to whisking behavior in an awake rate (Carvell et al., 1996a). This study found a limited relationship between neural spike trains and the activation of a particular set of muscles involved in whisking, but this study preceded the advent of numerous techniques to perform videographic vibrissa tracking (Bermejo and Zeigler, 2000; Knutsen et al., 2005; Hill et al., 2008; Voigts et al., 2008), and so a definitive characterization of self-motion signals in vM1 is lacking.

Here we revisit the issue of representation of rhythmic whisking behavior in vM1 by comparing single unit spike trains to both vibrissa motion and muscle activity. We ask the following. (1) Do spikes from units in vM1 correlate with the kinetic parameters of whisking behavior? (2) How well do single units and populations of units predict the trajectories of vibrissa motion in real time? (3) How does the representation of self-motion in primary motor cortex compare to the corresponding representation in primary somatosensory cortex?

4.2 Methods

Subjects

We report data from 10 adult female Long-Evans rats (Charles River) weighing 200 to 300 g in mass. Five of these rats were trained to whisk on a raised platform for their home cage (Fig. 4.1A) while the other five were acclimated to head-restraint (Fig. 4.1B) as described previously (Hill et al.). In either paradigm, the training period typically lasted one to two weeks.

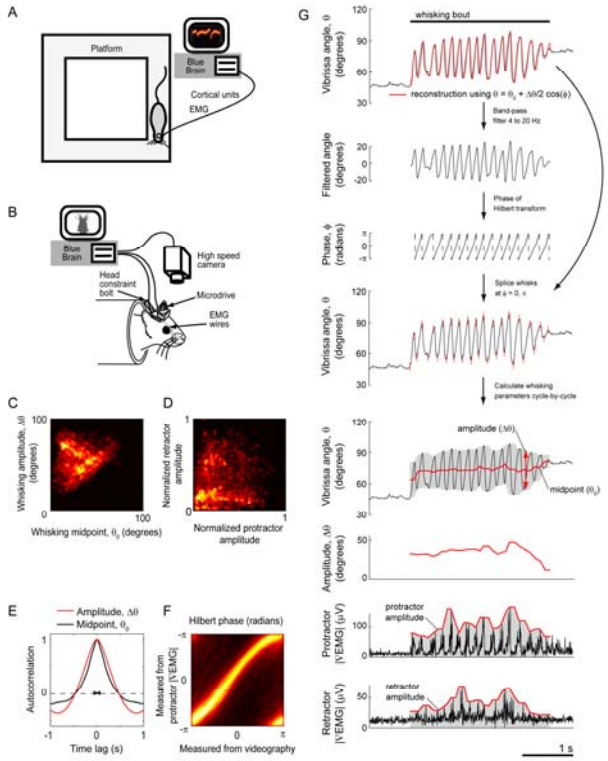

Figure 4.1: Experimental setups and data acquisition
A. Free ranging apparatus**.** The rat freely explores a raised platform. Whisking is evoked by placing the home cage just out of reach from the platform. Cortical and EMG signals are recorded. **B.** Head-constrained apparatus. The animal's head is held in place via a bolt embedded in its head mount. A high-speed camera is used to track vibrissa motion. The rat is trimmed down to a single row of vibrissae. **C.** 2D histogram of whisking amplitude versus midpoint measured on a cycle-by-cycle basis from a single behavioral session. **D.** 2D histogram of protractor and retractor $|\nabla EMG|$ amplitude measured on a cycle-by-cycle basis from a single behavioral session. Values are normalized on maximum amplitude recorded for that session. **E.** Autocorrelation of amplitude and midpoint parameters measured from a single behavioral session. Autocorrelation decreases to zero at 500 ms. Reference bar is 120 ms to indicate duration of a single whisk. **F.** 2D histogram of phase estimated from videography of vibrissa angle versus phase estimated from protractor EMG data for a single session. Relationship is approximately a constant phase lag of 0.6 radians. **G.** Flowchart of data processing to estimate phase of whisking of a motion trace for a single whisking bout. Top panel shows unprocessed daya with reconstruction of motion from kinetic parameters. Red ticks in bottom panel shows time points where phase is equal to 0 or π. The fifth and sixth panels show the estimation of midpoint and amplitude from individual whisk cycles. Double-headed arrow in top panel indicates the amplitude which is plotted in the bottom panel. The amplitude is defined as the range of angles swept out on a single cycle which is shaded in gray. Bottoms two panels show estimation of amplitude of $|\nabla EMG|$ for protractor and retractor muscles on a cycle-by-cycle basis.. Amplitude is defined as the maximum value of the signal on each cycle which is shaded in gray.

Successful training of either of the above paradigms was followed by chronic implantation of a microdrive (Ventakachalam et al., 1999) above the area of cortex stereotaxically identified as the vibrissa region of primary motor cortex (vM1) at coordinates 2.5 mm anterior and 1.5 mm lateral of bregma. The headstage was secured in place with bone screws and dental acrylic. Each headstage contained four stereotrodes fabricated from a twisted, beveled pair of .001" tungsten microwires. A vacuum was applied to the lower chamber of the microdrive as each stereotrode was advanced through the dura to prevent damage to the upper layers of cortex. Additionally the contralateral facial muscles were implanted with pairs of .002" tungsten microwires to record the selectromyogram (EMG). The extrinsic muscle *m. nasolabialis* and the intrinsic muscles of the mystacial pad were implanted as described previously (Hill et al., 2008). In animals conditioned to head-restraint, a restraining bolt was implanted posterior to the microdrive. Animals that underwent head-restraint were also routinely subject to vibrissa trimming and application of a chemical depilatory to the fur of the mystacial pad in order to facilitate videography. All vibrissae and fur are removed from the mystacial pad except for the C-row macrovibrissae. All procedures were performed under isoflurane anesthesia. The care and experimental manipulation of our animals were in strict accord with guidelines from the US National Institutes of Health and have been reviewed and approved by the

Institutional Animal Care and Use Committee of the University of California, San Diego.

Data acquisition

Continuous time series from the cortical and EMG microwires were band-pass filtered from 1 Hz to 10 kHz. All data was sampled at 36 kHz and acquired in trials of 10 to 30 s in duration. In head-restrained animals, a high-speed camera was used to monitor vibrissa position. The video frame rate was 300 Hz at 150 μm spatial resolution. The TTL exposure line of the camera was acquired to synchronize image and data acquisition. Vibrissa position was obtained from each frame using a semi-automated algorithm written in Matlab using a previously described algorithm (Hill et al., 2008). The angle was measured as the anterior-posterior angle between the skin at the base of the vibrissa and the initial 5 millimeters of the vibrissa shaft that is approximately straight. In all cases, the vibrissa that was tracked was either C1 or C2.

The cortical recordings were digitally band-pass filtered between 600 Hz and 6 kHz in order to isolate the spectral power of extracellular spike waveforms. The two EMG channels from each implanted muscle were digitally subtracted, band-pass filtered between 400 Hz and 3 kHz, and rectified using the absolute value. Finally, this signal was low-pass filtered at

250 Hz and down-sampled to 1 kHz to form the differential rectified EMG signal (|∇EMG|). The vibrissa angle signal was low-pass filtered at 40 Hz and up-sampled to 1 kHz.

Analysis

Vibrissa motion and |∇EMG| signals were decomposed into separate phase, offset, and amplitude signals by use of the Hilbert transform (Fig. 4.1G). In brief, whisking epochs were isolated and the motion data was band-pass filtered between 4 and 20 Hz. To calculate the Hilbert transform, the Fourier transform was computed, the power at negative frequencies was set to zero, and a complex-valued time series was generated via the inverse Fourier transform. The angle of this signal in polar coordinates was taken as the phase of the whisking cycle where a phase of 0 corresponds to the end of protraction and a phase of +/-π corresponds to the end of retraction. The time points of maximum retraction and protraction were used to define the amplitude and midpoint of individual whisks where amplitude is defined as the range of angles swept out during a single whisk cycle and the midpoint is the bisecting angle of this range. The amplitude of the |∇EMG| was defined as it maximum value on an individual cycle. These amplitude and midpoint parameters were linearly interpolated for phase values between 0 and +/-π. In data sets where vibrissa position was not tracked, the Hilbert transform was applied to the intrinsic muscle |∇EMG| to calculate whisking phase. This

signal was delayed by 20 ms to account for the delay between muscle activity and motion (Berg and Kleinfeld, 2003a).

To obtain single-unit spike trains, cortical recordings were spike sorted with an offline non-Gaussian cluster analysis algorithm (Fee et al., 1996). Putative single units were accepted for analysis if the number of inter-spike intervals les than the absolute refractory period of 3 ms was consistent with less than 10% contamination of the spike train by a Poisson process. Further, the waveforms of the units were checked for separation from background noise levels and other waveform clusters obtained in the same recordings. To estimate the firing rate of a unit as a function of a whisking parameter, first the histogram of the parameter at the time of individual spikes was calculated. These values were then normalized by a histogram of the parameter taken at all times. The 95% confidence interval on these functions was estimated by bootstrapping the spike-conditioned histogram using 1000 iterations. The significance of firing rate modulation was determined by comparing the distributions of the spike-conditioned parameter and the unconditioned parameter using a 2-sample Kolmogorov-Smirnov test. Alternatively, a 2-sample Kuiper test was used for the phase parameter because this test is more appropriate for cyclically distributed variables.

The linear phase predictor was derived from the linear transfer function between the single-unit spike train and the angular motion. The transfer function H(f) is calculated from the Fourier transform of the spike train S(f) and the Fourier transform of the motion data E(f) as

$$(1)\quad H(f) = \frac{\left\langle S(f)E^{*}(f)\right\rangle_{trial}}{\left\langle S(f)^{2}\right\rangle_{trial}}$$

where the angular brackets denote averaging over trials. Each trial was taken from a 1 s epoch of whisking comprising 90% of the total number of records for that unit. The measured transfer function was then applied to the remaining 10% of trials to calculate the Fourier transform of the predicted motion as

$$(2)\quad E_{pred}(f) = H(f)S(f).$$

This function was then inverse Fourier transformed and the phase was calculated with the Hilbert transform for comparison to the measured transform.

Simulations

Populations of simulated, independent Poisson spike trains were used to estimate amplitude and midpoint parameters from neuronal response properties recorded from vM1. The simulations were performed on two types of populations. In the first case, the simulated population was derived from

the entire set of neurons that were significantly modulated by the parameter being estimated. In order to increase the simulated population size, *p*, above the number of recorded neurons, the entire set of neurons was duplicated. Thus, the value of *p* was always an integer multiple of the size of the original number of neurons. In these simulations, the integration time τ was held constant at 250 ms. In the second set of simulations, only one neuron from our data set but τ was varied between 250 ms and 125 s.

In order to estimate a parameter value with the simulated neuronal population, first a parameter value $\mu = x$ u was selected as input for all neurons. The mean firing rate for the i^{th} neuron, denoted λ_I, is then calculated as $\lambda_I = f_i(x)$ where the response function $f_i(x)$ is determined using the histogram method described above. Next the number of spikes generated by the i^{th} neuron was drawn from a Poisson process with a mean equal to the firing rate, λ_I, and integration time τ, given by

$$(3)\quad P(N_i = k \mid \lambda = \lambda_i) = \frac{e^{-\lambda_i \tau}(\lambda_i \tau)^k}{k!}$$

where N_I is the number of spikes generated by the i^{th} neuron. The posterior distribution of the parameter μ given the spike counts from all simulated neurons was calculated using Bayes rule and the principle of independence to give the equation

$$(4)\ P(\mu = x \mid N_1, N_2, ..., N_p)$$

$$= \prod_{i=1}^{p} P(\mu = x \mid N_i)$$

$$= \prod_{i=1}^{p} \frac{P(N_i \mid \mu = x)P(x)}{P(N_i)}$$

$$= \prod_{i=1}^{p} \frac{P(N = N_i \mid \lambda = f_i(x))P(\mu = x)}{P(N = N_i)}$$

.

The prior distribution *P(μ =x)* is taken from the histogram of parameter values recorded from during behavioral session. The range of parameter values varied from session to session (Fig. 4.4C and D), so the response functions $f_i(x)$ were aligned on the central 90% of data points. The prior distribution $P(N = N_i)$ is a normalization term and does not need to be computed directly. The estimate of the parameter μ was taken as the maximum value of the distribution $P(\mu = x \mid N_1, N_2, ..., N_p)$ which yields the maximum a posterior estimate.

Simulation were run for 1000 trials for each of 50 equally spaced parameter values. The mean absolute difference between the estimate and input was recorded as the error. Here we report the expected value of this error by weighting the individual errors by the prior distribution *P(μ =x)*.

4.3 Results

Rats were trained to either whisk while free-ranging on a raised platform (Fig. 4.1A) or while head-fixed (Fig. 4.1B). In both paradigms, rats typically spent greater than 25% of each session engaged in rhythmic whisking, providing more than 1000 whisks per session. Animals that were successfully trained underwent surgery to implant a microwire head stage (Ventakachalam et al., 1999) over the stereotaxically-identified vibrissa region of primary motor cortex (vM1) (Hoffer et al., 2003; Haiss and Schwarz, 2005a) to record extracellular neuronal spike waveforms. Pairs of microwires were also implanted in the facial muscles that drive rhythmic protraction and retraction of the vibrissae to obtain the differential rectified electromyogram ($|\nabla EMG|$) (Hill et al., 2008). Extracellular cortical data recorded during behavioral sessions was sorted offline into putative single unit spike trains based on consistency of waveform and lack of interspike intervals less than 3 ms in duration. In rats trained to whisk while head-fixed, the anterior-posterior angle of the vibrissa with respect to mystacial pad was measured from video recordings from a high-speed camera mounted above the animal's head.

To aid comparison of spike trains in vM1 to the kinetic parameters of whisking behavior, epochs of rhythmic whisking were manually labeled and then algorithmically decomposed into a set of fast and slowly varying signals (Fig. 4.1G). The anterior-posterior angle of the vibrissa over time $\theta(t)$ was decomposed according to the equation $\theta(t) = \theta_0(t) + (\Delta\theta(t)/2) \cos(\phi(t))$ where θ_0 is an offset parameter that corresponds to the midpoint between the two extreme angles of vibrissa position during a single whisk cycle, $\Delta\theta$ is an amplitude parameter equal to the angle swept out during the whisk cycle, and ϕ is the phase of the whisk cycle where a value of 0 corresponds to the time of maximum protraction and a value of π corresponds to the time of maximum retraction. The phase parameter was estimated by applying the Hilbert transform to the band-pass filtered signal $\theta(t)$. The amplitude was calculated as the range of angles swept out on a single whisk cycle while the midpoint was calculated as the middle angle of this range. By substituting these signals into the above equation for $\theta(t)$, we were able to reconstruct the original motion faithfully (Fig. 4.1G). Note that this decomposition creates a nearly independent basis set to describe whisking behavior as amplitude and midpoint have little correlation (Fig. 4.1C). A cubic regression analysis revealed that on average 13% of the variance in the amplitude signal can be predicted from variance in the midpoint signal. In addition, both of these parameters have autocorrelation on a much larger timescale (~500 ms) than phase (Fig. 4.1E) which completely cycles during each whisk (~120 ms).

Finally, the amplitude of the EMG activity of the protractor and retractor muscles was calculated on each cycle as the maximum value of the rectified signal (Fig. 4.1D). In behavioral sessions without videography, the phase of whisking was estimated from the rectified protractor EMG signal using the same algorithm as above. The resulting signal was found to closely correspond to the phase signal estimated from videography with a phase-advance of 0.6 to 1.0 radians due to the lag between muscle activity and vibrissa motion (Fig. 4.1F).

Relationship between spike rate and whisking epochs

We recorded 114 units from vM1 cortex in 10 rats, 86% of which responded to whisking in air. A previous study reported that units in vM1 nearly universally increase in firing rate during whisking behavior(Carvell et al., 1996a), but here we find that individual units could either increase or decrease their firing rate during epochs of rhythmic whisking when compared to background rates (Fig. 4.2). The mean change in firing rate was +/- 30%, with individual units showing as much as a 190% increase or 80% decrease in firing rate during rhythmic whisking. The number of units that were excited versus inhibited by whisking was statistically identical and the population rate showed only a small increase in firing rate from 6.3 Hz during non-whisking epochs to 6.5 Hz during whisking epochs. This result is similar to findings in

the vibrissa region of primary sensory cortex where the change in firing rate during whisking behavior is negligible (Curtis and Kleinfeld, 2009).

Local-field potential recordings in vM1 have shown that a transient increase in low-frequency electrical activity precedes some whisking bouts by about 300 ms (Friedman et al., 2006b). Here we ask whether spike rates also transiently increase in the period immediately prior to transitions between whisking and non-whisking epochs. The exact time of a transition is often ambiguous in spontaneous behavior, so transitions were identified as the time points showing the greatest change in total EMG activity between the previous and subsequent 500 ms periods (Fig. 4.2C). While we found individual units that exhibited increases in firing rate that preceded the onset or offset of whisking, the total population of recorded units did not show any transient increase in firing rate.

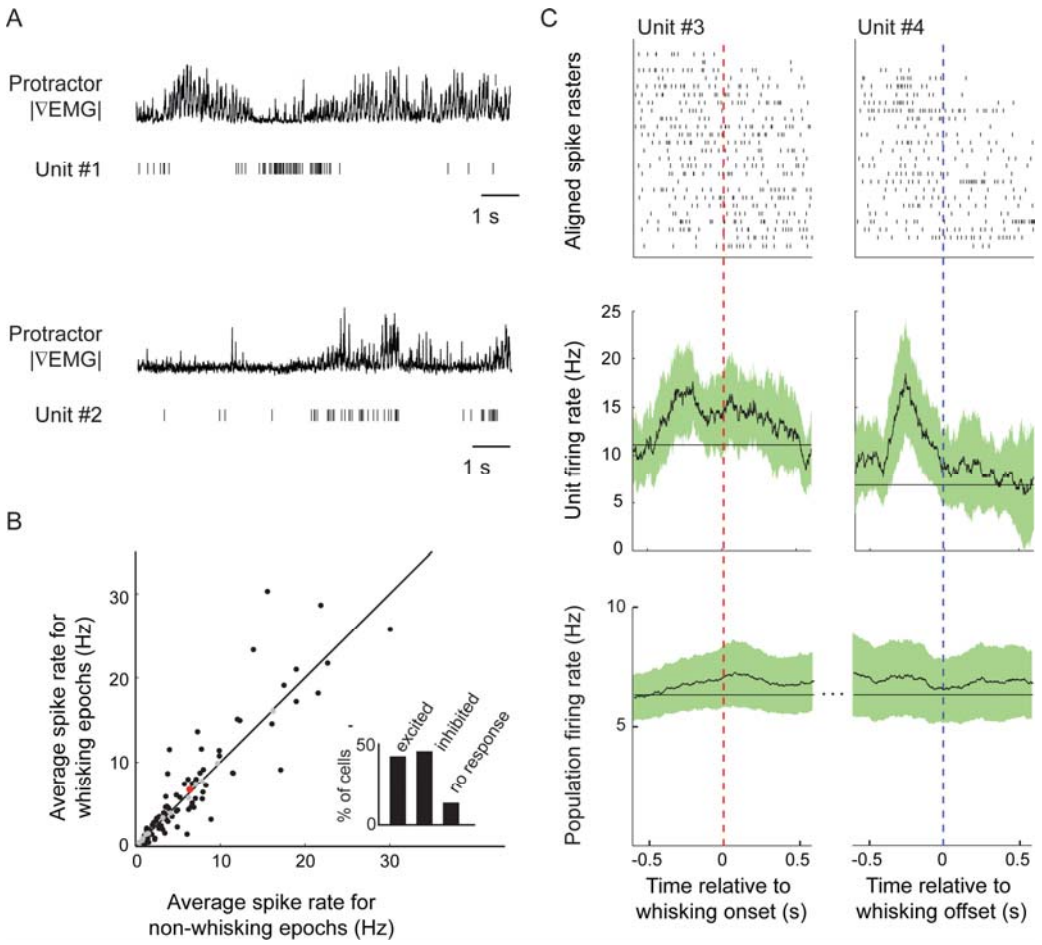

Figure 4.2: Comparison of firing rates during whisking and non-whisking epochs
A. Example data from a unit that is inhibited by whisking and one that is excited. **B.** Scatter plot of firing rates during whisking and non-whisking epochs for all units in this study. Diagonal line denotes equal firing rate between two conditions. Black dots show a significant difference in firing rate while the gray dots are not significant. Red dot indicates population average of 6.5 Hz for whisking epochs and 6.3 Hz for all other times. Inset shows percent of cells that are excited, inhibited, or show no change in firing rate during whisking. **C.** Example and population firing rates around onset and offset of whisking. Top panels show raster of spikes fired around onset (*left)* and offset (*right)* of whisking for 25 events for units that fired bursts prior to these events. Middle panels show firing rate as a function of time. Traces were smoothed with a 100 ms boxcar window. Bottom panels show firing rate as a function for population as a whole where 25 onset and offset events were chosen for unit. As a population average, there is no prominent increase in firing rate at the onset or offset of whisking. Green shading on all traces represents +/-2 jackknife standard deviations.

Single units in vM1 reliably encode the phase of whisking

We next explored the ability of units in vM1 to track the motion of the vibrissae in terms of the kinetic parameters of phase, amplitude, and midpoint. To detect a significant modulation of firing rate with one of these parameters, the distribution of values for a given parameter condition on a spie event was compared to the distribution of values taken at all times (Fig. 4.3B). A significanct difference in distributions ($p<0.05$) was determined with a 2-sample Kuiper's test for the phase parameter or with a 2-sample Kolmogorov-Sminnov test for all other parameters. To quantify the degree of modulation of firing rate with a specific parameter, we used the quantity

$$\text{Modulation depth} \equiv \frac{\text{Maximum Spike Rate - Minimum Spike Rate}}{\sqrt{\text{Mean Spike Rate for Whisking in Air}}}.$$

This value roughly corresponds to a signal-to-noise ratio comparing the change in firing rate to be detected to the standard deviation of a Poisson process with the same mean firing rate.

We observed a significant modulation of firing rate with whisking phase in 22% of neurons (Fig. 4.3C). The mean modulation depth was 1.6 with a maximum of 4.5. While the preferred phase of units extended over the full range of the whisk cycle, 70% of units fired preferentially during retraction. To quantify how well a single unit can encode phase of whisking, we calculated the linear transfer function between the spike trains of the most

modulated cell and the concurrently recorded vibrissa angle (Fig. 4.3A) using all but one whisking epoch. The transfer function was then applied to the spike train in the single unused whisking epoch. The phase of the predicted motion was then compared to the actual phase of whisking using a linear regression analysis. The mean absolute error of the phase predictor for this trial is 0.4 radians or +/- 6% of the whisk cycle. When the linear transfer function was applied to the entire data set the mean error was 1.1 radians or +/- 18% of the whisk cycle. We thus conclude that single units in vM1 are sufficiently modulated by whisking to accurately report whisking phase.

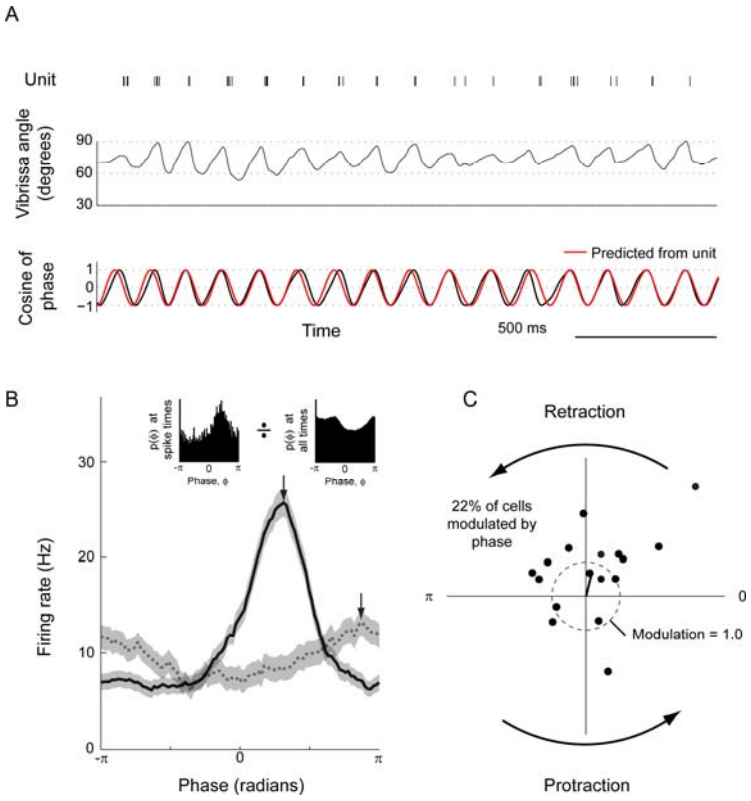

Figure 4.3: Relation of phase in whisking cycle to spike arrival time
A. Example spike train and vibrissa motion during a whisking epoch for a phase-modulated cell. Bottom panel plots the cosine of whisking phase versus the cosine of phase predicted from the unit activity. The transfer function between the single unit and vibrissa motion was calculated from a separate set of 85 whisking epochs, and this linear predictor was applied to the displayed spike train to calculate the predicted motion and its phase. The prediction had an average error of 1.1 radians over the entire data set for this unit. **B.** Plot of firing rate versus phase for two phase-modulated units. The trace with greater modulation is same as in A. Traces were smoothed with a boxcar having a width of □/4 radians. Shaded region is a 95% confidence interval calculated from 1000 iterations of the bootstrap method. Arrowheads indicate location of preferred phase. The modulations of the two units are 1.5 and 4.5. Inset illustrates procedure of normalizing the probability distribution of phase at spike times by the probability distribution of phase at all times. Inset data also corresponds to unit from A. Note that the Hilbert transform does not produce a uniform distribution of phases for whisking behavior. **C.** Scatter polar plot of preferred phase versus modulation for each of the 17 units that exhibited significant phase modulation. The whisk cycle advances forward in time as coordinates move counterclockwise about the origin. Distance from the origin corresponds to degree of modulation. Black line segment indicates the average location of all significant data points. This indicates an overall bias of 1.3 radians, indicating an overall phase preference toward retraction.

Populations of units encode amplitude and midpoint of whisking in their firing rate

We next explored the ability of single units to encode the slowly-varying parameters of whisking. We found that 79% of units in vM1 showed significant modulation with either amplitude or midpoint (Fig. 4.4). In general, individual units were found to have a monotonic relationship between the parameter value and their firing rate, although this relationship could be either increasing or decreasing (Fig. 4.4A and B). Firing rate traces were not directly comparable between units because of differences in the range of amplitudes and midpoints in different behavioral sessions (Figs. 4.4C and D) as a result of differences in behavior between animals or because tracking was performed on vibrissae from different arcs. Therefore the firing rate curves were remapped onto the “typical” range of motion averaged over all sessions. The mean of the remapped firing rates showed only minor fluctuations in population firing rate over different amplitudes and midpoints (Fig. 4.4C and D). Therefore roughly as many spikes are generated as are dropped as the rat changes behavior. Finally we note that 34% of neurons showed correlation with both parameters (Fig. 4.4E) although there was no strong correlation between the modulation depths (Fig. 4.4F).

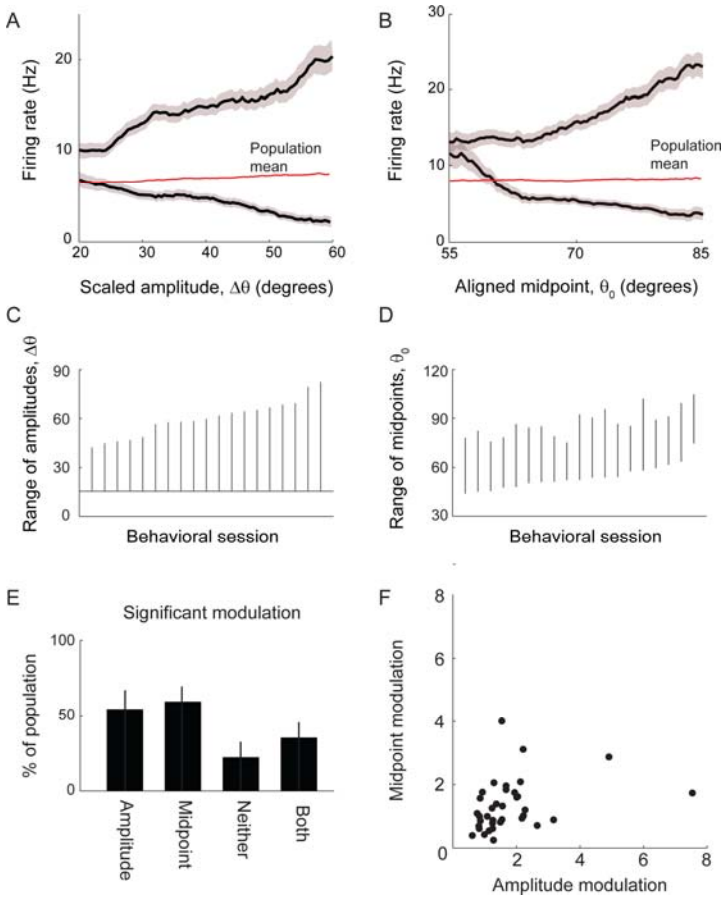

Figure 4.4: Relation of firing rate to slowly-varying parameters of whisking
A. Firing rate versus amplitude for 2 representative cells (black traces) and the population mean (red trace). Cells typically showed a monotonic change in firing rate with a change in amplitude, either increasing or decreasing over the full range, but the population average shows a marginal trend. The ranges of amplitudes swept out in different behavioral sessions were not equal, so plots were scaled onto the average range of amplitude. The shaded area represents 95% confidence interval on mean firing rate obtained from bootstrapping for 1000 iterations. **B.** Firing rate versus midpoint for 2 representative cells (black traces) and the population mean (red trace). Shaded region is same as in A. Individual traces are remapped onto the average range of midpoints observed across sessions. **C.** Range of amplitudes swept out in all behavioral sessions. Black line represents the central 90% of whisking amplitudes observed during that session. The black horizontal line represents an arbitrary cutoff of 15^{o} that was used to eliminate small movements from analysis that may not represent typical whisking behavior. **D.** Range of midpoints observed in all behavioral sessions. Sessions are sorted by minimum value and do not correspond to order used in C. Some variation in midpoint is expected depending on which arc was tracked during the session. All tracked vibrissae were either C1, C2, or C3. **E.** Bar graph of percentage of units in this study that were significantly modulated with amplitude and midpoint. Total number of units tested for significance was 46. Black lines represent 95% confidence interval. **F.** Scatter plot of amplitude and midpoint modulation. The 22% of units that were not found to be significantly modulated by either parameter were excluded from this plot.

In principle the precise timing of spikes in vM1 may convey information about amplitude and midpoint, but since these parameters vary over a timescale of 500 ms (Fig. 4.1E) we used this as the relevant time scale for analysis of firing rates. We developed an ideal observer model for simulated populations of spike trains in order to estimate the amount of integration time required to accurately decode the amplitude or midpoint of whisking behavior (Fig. 4.5A). The model assumes that neurons fire independently from each other and fire as a Poisson process with a mean firing rate characterized by its input-output curve. We chose an integration time of 250 ms for our analysis since this is the width at half-max of the auto-correlation for amplitude and midpoint. However, our model makes use of Poisson spike trains so that a change in integration time can be traded proportionately for the number of units used to perform the computation. We found that separate populations of less than 300 neurons would need 250 ms to decode amplitude and midpoint to a precision of less than 2.5^{o} (Fig. 4.5B and C). However, our data indicate that the neuronal populations are overlapping, so that the combined population need only be 400 neurons rather than 600. To characterize the contribution of single units to the estimate, we determined the error of populations consisting of identical copies of a single neuron from our data, or equivalently a single copy with a large integration time. We find that most but not all neurons perform worse than the heterogeneous population.

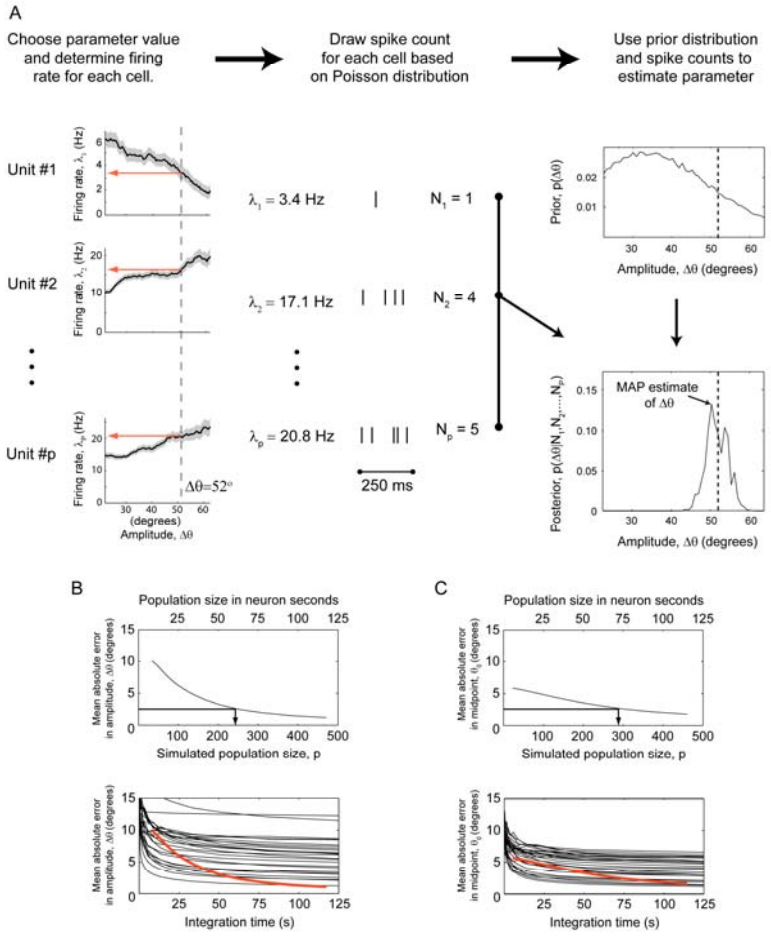

Figure 4.5: Simulations of population activity to estimate amplitude and midpoint of whisking
A. Schematic of procedure for neural simulations. A population of p independent simulated neurons was created by drawing uniformly from the set of neurons significantly modulated by either amplitude or midpoint. The case for amplitude is illustrated. The parameter space was divided into 50 bins, and for a given bin the firing rate of each neuron was taken from the curve of firing rate versus parameter for that cell. Traces (black lines) were smoothed and 95% confidence intervals (shaded area) were estimated as described in the text. The firing rate from each cell was used to generate a spike count for an integration window of 250 ms using the Poisson distribution. Vertical dashed lines indicate the value of the parameter used for this example. Right upper panel shows prior distribution for amplitudes. Probabilities were calculated from all data that was aligned as described above. Right lower panel shows posterior probability of amplitude given spike counts. The prior distribution and the number of spikes from each simulated neuron were used to calculate a posterior probability. The maximum value of the posterior was chosen to generate the maximum a posteriori estimator of the amplitude. The error in this estimate is the absolute difference between this value and the actual one. **B.** Accuracy of simulations as a function of simulated population size. Top panel is result of using all neurons significantly modulated by amplitude. An integration time of 250 ms was used in the simulations, but theoretically in a Poisson distribution time can be traded off against more units. The top abscissa reports the population sizes in units of neuron seconds. The bottom panel shows the result of simulations using individual units but varying the integration time. There exist units exist that perform better or worse than when the entire population is used. **C.** Same as B but with analysis for midpoint parameter.

Relation between firing rate and muscle activation

Single units in vM1 were also found to vary their firing rates monotonically with muscle activation (Fig. 4.6A). The distribution of responses was heterogeneous among units with examples of significance with the retractor muscles, the protractors, neither, or both (Fig. 4.6B and C). It was also observed that a unit could be positively correlated with one muscle and negatively correlated with the other (Fig. 4.6A). It is possible that the abundance of correlations is due to correlations between the activation of muscles themselves rather than to heterogeneous encoding. In order to account for this, a partial correlation analysis was performed where the two muscle signals were de-correlated from each other using a 5^{th} order polynomial regression before correlation analysis with a unit's spike train. The analysis demonstrated that some units encode independent information about the activation of both muscles while others are correlated with only a single muscle (Fig. 4.6C).

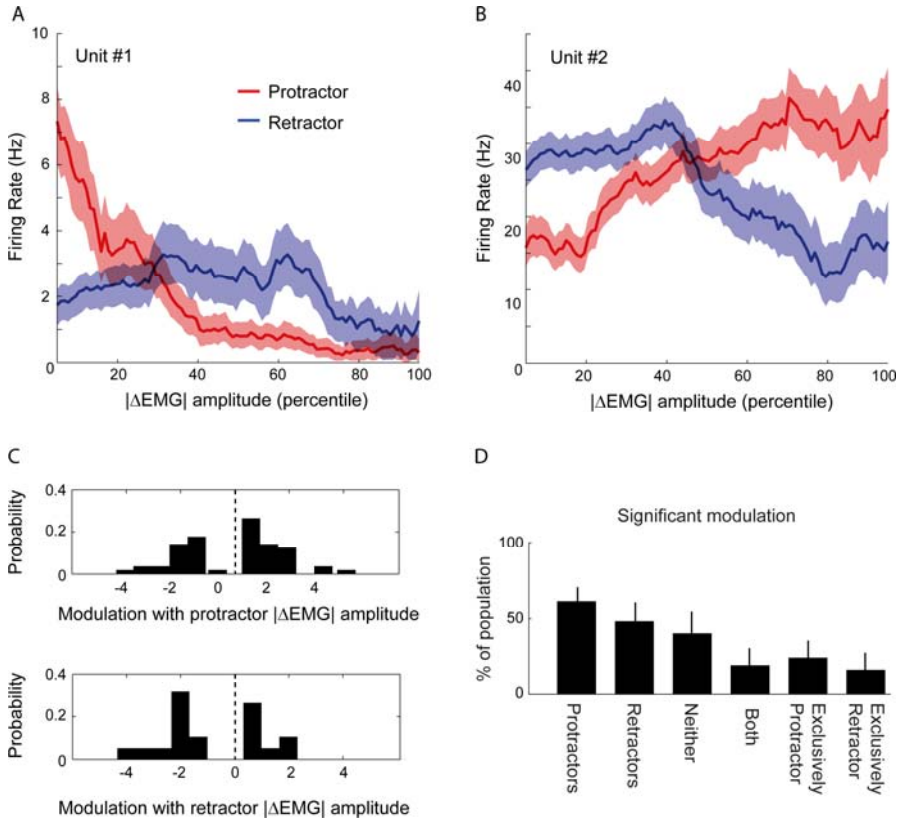

Figure 4.6: Relation of firing rate to amplitude of retractor and protractor muscle activity
A. Firing rate versus amplitude of protractor and retractor muscle activity for 2 representative cells. The ranges of muscle activity amplitudes for different muscles were not equal, so plots were scaled onto a percentile range. The shaded area represents 95% confidence interval on mean firing rate obtained from bootstrapping for 1000 iterations. **B.** Histogram of modulation depth for all cells significantly modulated by either the protractor or retractor muscles. **C.** Bar graph of percentage of units in this study that were significantly modulated by amplitude of muscle activity. Black lines represent 95% confidence interval. A negative value indicates that the firing rate was negatively correlated with muscle activity. **F.** Scatter plot of amplitude and midpoint modulation. The 22% of units that were not found to be significantly modulated by either parameter were excluded from this plot.

Comparison of motion encoding by S1 and vM1

The primary sensory and motor cortices are highly interconnected in rats (Miyashita et al., 1994a; Izraeli and Porter, 1995b; Zhang and Deschenes, 1997; Veinante and Deschenes, 2003; Alloway et al., 2004; Rocco and Brumberg, 2007), so it is likely that they communicate information about vibrissa position. Further, differences in representation of self-motion in the two areas may lead to insights in sensorimotor transformations in active sensing. To this end, we applied our analysis technique (Fig. 4.1G) to a data set of single units recorded in barrel cortex from a previously published study in our lab (Curtis and Kleinfeld, 2009). This data set included simultaneously recorded vibrissa position for 78 units and simultaneously recorded protractor EMG signals for 152 units using identical recording techniques to the present study. Rats were either freely exploring a raised platform or held in a body-constraint tube. They were trained to whisk against a piezo-electric sensor for reward, but data sets contained trials taken both during the task and unconditioned spontaneous whisking. We found that units in S1 are significantly modulated by amplitude, midpoint, and phase (Fig. 4.7A). This result is consistent with previous findings that units in S1 encode the phase and amplitude of protractor muscle activity (Fee et al., 1997). In comparison to vM1, we find that units in S1 are less likely to encode the slowly-varying signals of amplitude and midpoint than vM1, but that S1 has a more frequent occurrence of phase modulation. We also found that the phase bias in vM1 is

delayed by 0.8 radians relative to S1 (Fig. 4.7B). Assuming 8 Hz whisking, this is consistent with a 15 ms delay between vM1 and S1 activation as identified recently in mouse cortex (Ferezou et al., 2007).

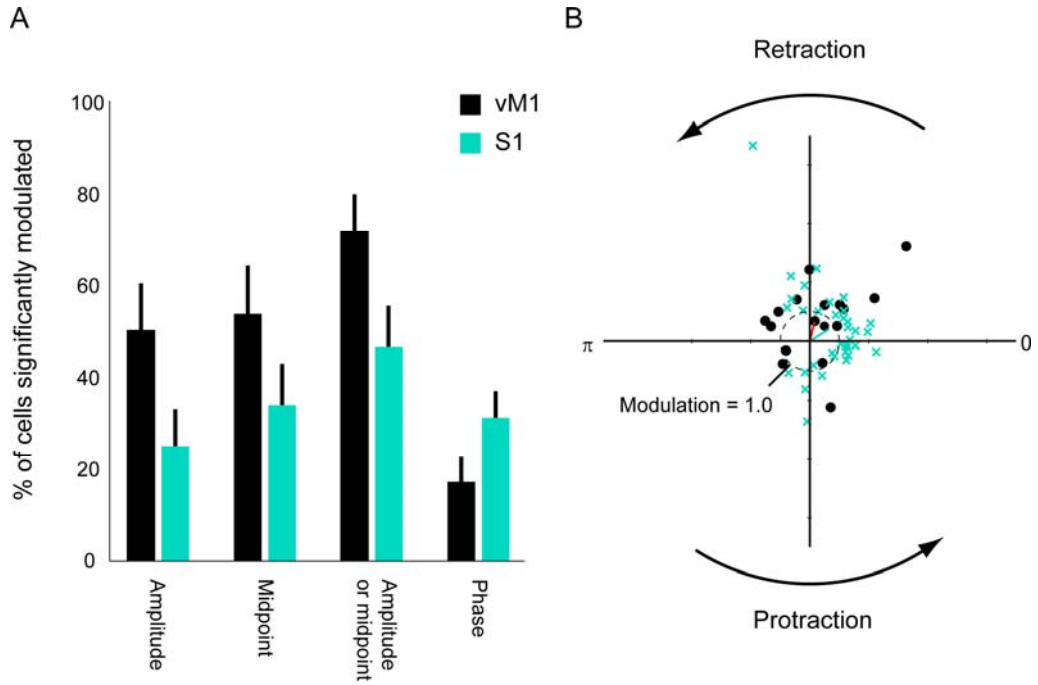

Figure 4.7: Comparison of S1 and vM1 units for modulation by kinetic parameters of whisking.
A. Bar graph of percentage of cells significantly modulated by each parameter. Black lines represent 95% confidence interval. Units in vM1 are modulated by the slowly-varying parameters amplitude and midpoint significantly more often than units in S1. In contrast, units in S1 modulated by phase significantly more often than units in vM1. **B.** Scatter polar plot of preferred phase versus modulation for significantly modulated units in S1 and vM1. The whisk cycle advances forward in time as coordinates move counterclockwise about the origin. Distance from the origin corresponds to degree of modulation. Red and cyan line segments indicate the average location of all data points for vM1 and S1, respectively. The bias in vM1 represents a 0.8 radian lag from units in S1, or approximately 15-20 ms on the timescale of a whisk cycle.

4.4 Discussion

We report the correlates of single unit spike trains in vM1 of the rat to the parameters of rhythmic whisking behavior. We find that populations of a few hundred cells can accurately report whether the animal is whisking and the specific trajectory of vibrissa motion. The presence of whisking is encoded by changes in firing rate observed in most cells and bursts of activity preceding a change in behavioral state in a few cells (Fig. 4.2). A minority of cells locks rhythmically to whisking, but some units show enough rhythmic modulation to report the precise phase of the whisk cycle (Fig. 4.3). And while many cells vary their firing rate with slower changes in the amplitude and midpoint of whisking, a population of a few hundred cells is required to decode these parameters from spike activity on the relevant timescale of 250 ms (Fig .4.4 and 4.5). Finally, we find that this representation of self-motion in vM1 differs significantly from that of barrel cortex of S1 with vM1 exhibiting a decreased representation of the rhythmic component of whisking and an increased representation of the slow-varying amplitude and midpoint parameters (Fig. 4.7).

Role of vM1 in control of whisking

Although physiological studies of motor cortex during whisking behavior are few in number, several lines of evidence point to the role of vM1 in controlling both the rhythmic and slowly-varying parameters of whisking.

First, stimulation experiments in anesthetized rats demonstrate that a rhythmic whisking bout can be initiated by non-rhythmic stimulation of vM1 (Cramer and Keller, 2006a). Further, the local field potential recordings from vM1 in awake, behaving rats exhibit an increase in the amount of field activity in the few hundred ms before a whisking bout (Friedman et al., 2006b). Our data extend this result by showing that individual units can burst in the time period just before the onset or offset of a whisking epoch (Fig. 4.2). Furthermore, units show sustained increases or decreases in firing rate during whisking even in the absence of rhythmic locking to vibrissa motion. These data indicate that vM1 may be responsible for the initiation and maintenance of a whisking epoch, but this role is not a necessary one as whisking behavior persists in animals with cortical lesions (Semba and Komisaruk, 1984a; Gao et al., 2003b). Therefore, the role of vM1 in the initiation of whisking may be a strictly intermittent one.

There is also evidence that controls whisking behavior on a much faster time scale. Rhythmic stimulation of vM1 at 10 Hz in both anesthetized and awake rates can produce 10 Hz rhythmic movement of the vibrissae at a 15 ms time delay (Berg and Kleinfeld, 2003b). An anatomical substrate for fast activation of musculature exists as vM1, quite unusually, directly projects to the motor neurons of the lateral aspect of the facial nucleus that drive the protractor muscles (Grinevich et al., 2005). The local field potential of vM1

has been measured to coherently lock to whisking behavior albeit weakly (Ahrens and Kleinfeld, 2004). Our data extend these results by showing that individual units of vM1 also lock to the whisking cycle. Regardless of whether this signal represents a re-afferent sensory signal or efference, the components necessary for fast control our available in vM1.

With rhythmic and slow means of control possible in vM1, it may be the case that both forms of control are expressed in a behavioral-state dependent way. As evidence toward this state-dependence of control in vM1, the effect of rhythmic stimulation on vM1 is qualitatively changed from rhythmic to slow control by the switch between a sessile and awake state or by the activation of nucleus basalis (Berg et al., 2005).

Our data also bears on the segregation of the control of individual muscles. It has been previously reported that control of retraction and protraction is spatially segregated in vM1 (Haiss and Schwarz, 2005a). However, recordings of the electrical activity of the protractor and retractor muscles showed that both are excited by stimulation at single locations in vM1 (Berg and Kleinfeld, 2003b). In our recordings, we found units that strictly correlated with the activity of one muscle or the other, and many that correlated with both (Fig. 4.6). If these units are reporting gross parameters of the motion such as midpoint and amplitude, then it is likely that they will also

correlate with the activity of both muscles. In systems such as motor control of arm movements, where there are a large number of degrees of freedom, it is difficult to disentangle correlation with an individual motion from a correlation with a movement parameter. Whisking behavior presents a unique opportunity to disentangle muscle control from high-level behavioral control because the system contains a single degree of freedom with two independently controlled muscles. We cannot conclude from our data whether vM1 is acting to control individual muscles or gross aspects of the behavior because we do not know whether the signals we recorded are proprioceptive or efferent, but this issue can be resolved with additional experiments involving transaction of the sensory nerve.

Coordinate systems for representation of vibrissa motion

Here we propose the Hilbert transform as a useful tool for decomposing rhythmic vibrissa motion into a fast-varying phase parameter and two slow-varying kinetic parameters, the amplitude and midpoint (Fig. 4.1). The advantages of this coordinate system are that these three parameters are largely statistically independent of each other and together they can faithfully reconstruct the original vibrissa motion. For each parameter, we found examples of cells with significant modulation by only that parameter and not the other two which suggests that the animal may organize its representation along these dimensions. Finally, eidence for a

similar segregation of representation into fast and slow components has been documented in S1 (see below).

This is not the only possible coordinate system for representation of whisking motion. Most notably, whisking behavior contains a third slowly-varying parameter of frequency. The frequency of whisking is known to remain stable over many seconds, rivaling the regularity of a perfect sine wave (Berg and Kleinfeld, 2003a). The amplitude and midpoint vary on the a time scale of 500 ms (Fig. 4.1), so frequency may represent a third, slower time scale. We excluded the frequency variable from our analysis since it is not necessary to reconstruct vibrissa motion and because it is correlated with whisking amplitude (Berg and Kleinfeld, 2003b). However, frequency is necessary to construct other kinetic variables such as velocity since velocity is proportional to both amplitude and frequency. Therefore, the relevant coordinate system for representation of the velocity of the vibrissa may be phase, amplitude, and frequency. The animal may separately encode the velocity of its vibrissae, for example, in order to normalize the intensity of a contact event with an external object. We emphasize that vibrissa motion and velocity are related by a simple linear transform, the derivative, so that any analysis of position encoding versus velocity encoding must establish the presence or absence of modulation by the midpoint parameter.

Role of vM1 in encoding of self-motion

Two prior studies give evidence for a segregation of phase and amplitude parameters in cortical encoding of vibrissa motion. The first by (Fee et al. 1997) found that phase encoding in S1 was disrupted but amplitude encoding persisted after temporary block of the motor nerve for the whisking musculature. Here, the unblocked muscle activity on the ipsilateral side of the face was used as a surrogate for the unobserved motor command on the contralateral side. One conclusion from this result is that the representation of amplitude in S1 is derived from motor copy, at least in part. More recently it was observed by (Curtis and Kleinfeld 2009) that a subset of cells in S1 encode touch events in phase coordinates so that amplitude and midpoint are largely normalized out of the response. It was suggested that this normalization may be useful to maintain an equal dynamic range of neural activity during all behavior. What is the source of the efferent copy of amplitude in barrel cortex and how is this information re-integrated into the phase-coordinate system of object localization? Our data demonstrate the viability of vM1 as the source of amplitude and midpoint signals in S1, but it is as of yet unclear whether these signals represent an efferent copy. This issue can be resolved by recording from units in vM1 under conditions of nerve block in order to disrupt re-afferent signaling of vibrissa position. The necessity of vM1 for amplitude encoding in S1 can be directly assessed

through recordings of S1 under disruption of vM1 function, such as by application of the GABA agonist muscimol.

4.5 Acknowledgments

The content of this chapter is a manuscript that is currently under preparation for submission and will include J. C. Curtis as middle author and D. Kleinfeld as last author. We thank J. C. Curtis for training in the fabrication and implantation of the cortical microdrive and for providing the S1 electrophysiological data. We also thank J. Lee for training of the head-fixed animals as well as M. Brecht, P. L. Strick, H. J. Karten, and J. Moore for critical comments. This study was supported by grants from the Human Frontiers for Scientific Progress (RGP43/2004 to DK), the United States-Israeli Binational Science Foundation (2003222 to DK), and the National Institute of Neurological Disease and Stroke (NS37263 to HPZ and NS058668 to DK) and fellowships to DH through the National Science Foundation Integrative Graduate Education and Research Traineeship and National Research Service Award programs.

Chapter 5 – Conclusion

Here we have seen how the biomechanical properties of an active sensing system define a sensorimotor control problem and constrain the animal's behavioral repertoire. We have also seen how the motor cortex, nominally a high-level controller for this system, encodes the parameters of behavior differentially from sensory cortex. These data grant insight into how an organism represents interacting sensory and motor processes while highlighting that concepts such as "sensory" and "motor" are not and cannot be neatly delineated within the nervous system. Animals interact dynamically with their environment, which by necessity creates a closed-loop system with sensory stimuli and behavioral outputs reciprocally depending on one another.

Despite our limited understanding of how sensorimotor processes work to coordinate movement and perception, progress can be made via studies of sensation in the full context of active sensing under ethologically relevant conditions. As an example, it is not apparent how the data from the present study could be inferred from in vitro or anesthetized experimentation. Fortunately the tools for awake, behaving physiology are developing rapidly

and will expedite the elucidation of the neural circuits underlying sensorimotor processing.

References

Ahissar E, Sosnik R, Haidarliu S (2000) Transformation from temporal to rate coding in a somatosensory thalamocortical pathway. Nature 406:302-306.

Ahrens KF, Kleinfeld D (2004) Current flow in vibrissa motor cortex can phase-lock with exploratory rhythmic whisking in rat. J Neurophysiol 92:1700-1707.

Alloway KD (2007) Information Processing Streams in Rodent Barrel Cortex: The Differential Functions of Barrel and Septal Circuits. Cereb Cortex.

Alloway KD, Zhang M, Chakrabarti S (2004) Septal columns in rodent barrel cortex: functional circuits for modulating whisking behavior. J Comp Neurol 480:299-309.

An K, Conney WP, Linscheid RL, Chao EY (1989) Biomechanics of the Hand: A Basic Research Study. Teaneck: World Scientific.

Andermann ML, Ritt J, Neimark MA, Moore CI (2004) Neural correlates of vibrissa resonance: Band-pass and somatotopic representation of high-frequency stimuli. Neuron 42:451-463.

Arabzadeh E, Zorzin E, Diamond ME (2005) Neuronal encoding of texture in the whisker sensory pathway. Public Library of Science Biology 3:155-165.

Aronoff R, Petersen CC (2006) Controlled and localized genetic manipulation in the brain. J Cell Mol Med 10:333-352.

Berg RW, Kleinfeld D (2003a) Rhythmic whisking by rat: Retraction as well as protraction of the vibrissae is under active muscular control. Journal of Neurophysiology 89:104-117.

Berg RW, Kleinfeld D (2003b) Vibrissa movement elicited by rhythmic electrical microstimulation to motor cortex in the aroused rat mimics exploratory whisking. J Neurophysiol 90:2950-2963.

Berg RW, Kleinfeld D (2003c) Rhythmic whisking by rat: retraction as well as protraction of the vibrissae is under active muscular control. J Neurophysiol 89:104-117.

Berg RW, Whitmer D, Kleinfeld D (2006) Exploratory whisking by rat is not phase-locked to the hippocampal theta rhythm. Journal of Neuroscience 26:6518–6522.

Berg RW, Friedman B, Schroeder LF, Kleinfeld D (2005) Activation of nucleus basalis facilitates cortical control of a brain stem motor program. J Neurophysiol 94:699-711.

Bermejo R, Zeigler HP (2000) "Real-time" monitoring of vibrissa contacts during rodent whisking. Somatosensory and Motor Research 17:373-377.

Bermejo R, Houben D, Zeigler HP (1996) Conditioned whisking in the rat. Somatosensory and Motor Research 13:225-234.

Bermejo R, Vyas A, Zeigler HP (2002) Topography of rodent whisking I. Two-dimensional monitoring of whisker movements. Somatosensory and Motor Research 19:341-346.

Bermejo R, Friedman W, Zeigler HP (2005) Topography of whisking II: interaction of whisker and pad. Somatosens Mot Res 22:213-220.

Brecht M, Krauss A, Muhammad S, Sinai-Esfahani L, Bellanca S, Margrie TW (2004) Organization of rat vibrissa motor cortex and adjacent areas according to cytoarchitectonics, microstimulation, and intracellular stimulation of identified cells. J Comp Neurol 479:360-373.

Brown AWS, Waite PME (1974) Responses in the rat thalamus to whisker movements produced by motor nerve stimulation. Journal of Physiology 238:387-401.

Carvell GE, Simons DJ (1995) Task-and subject-related differences in sensorimotor behavior during active touch. Somatosensory and Motor Research 12:1-9.

Carvell GE, Miller SA, Simons DJ (1996a) The relationship of vibrissal motor cortex unit activity to whisking in the awake rat. Somatosensory and Motor Research 13:115-127.

Carvell GE, Miller SA, Simons DJ (1996b) The relationship of vibrissal motor cortex unit activity to whisking in the awake rat. Somatosens Mot Res 13:115-127.

Carvell GE, Simons DJ, Lichtenstein SH, Bryant P (1991) Electromyographic activity of mystacial pad musculature during whisking behavior in the rat. Somatosensory and Motor Research 8:159-164.

Castro-Alamancos MA (2006) Vibrissa myoclonus driven by resonance of excitatory networks in motor cortex. Journal of Neurophysiology in press.

Chakrabarti S, Alloway KD (2006) Differential origin of projections from SI barrel cortex to the whisker representations in SII and MI. J Comp Neurol 498:624-636.

Cramer NP, Keller A (2006a) Cortical control of a whisking central pattern generator. J Neurophysiol 96:209-217.

Cramer NP, Keller A (2006b) Cortical control of a whisking central pattern generator. Journal of Neurophysiology 96:209-217.

Cramer NP, Li Y, Keller A (2007) The whisking rhythm generator: a novel mammalian network for the generation of movement. J Neurophysiol 97:2148-2158.

Crochet S, Petersen CCH (2006) Correlating membrane potential with behaviour using whole-cell recordings from barrel cortex of awake mice. Nature Neuroscience 9:608-609.

Curtis J, Kleinfeld D (2005) Cortical neurons that code vibrissa contact in face-centered coordinates. In: Barrels (Hartmann M, ed), p in press.

Curtis JC, Kleinfeld D (2009) Phase-to-rate transformations encode touch in cortical neurons of a scanning sensorimotor system. Nat Neurosci 12:492-501.

Dorfl J (1982) The musculature of the mystacial vibrissae of the white mouse. Journal of Anatomy 135:147-154.

Dorfl J (1985) The innervation of the mystacial region of the white mouse. A topographical study. Journal of Anatomy 142:173-184.

Fee MS, Mitra PP, Kleinfeld D (1996) Automatic sorting of multiple unit neuronal signals in the presence of anisotropic and non-Gaussian variability. Journal of Neuroscience Methods 69:175-188.

Fee MS, Mitra PP, Kleinfeld D (1997) Central versus peripheral determinates of patterned spike activity in rat vibrissa cortex during whisking. Journal of Neurophysiology 78:1144-1149.

Ferezou I, Haiss F, Gentet LJ, Aronoff R, Weber B, Petersen CC (2007) Spatiotemporal dynamics of cortical sensorimotor integration in behaving mice. Neuron 56:907-923.

Friedman WA, Jones LM, Cramer NP, Kwegyir-Afful EE, Zeigler HP, Keller A (2006a) Anticipatory activity of motor cortex in relation to rhythmic whisking. Journal of Neurophysiology 95:1274-1277.

Friedman WA, Jones LM, Cramer NP, Kwegyir-Afful EE, Zeigler HP, Keller A (2006b) Anticipatory activity of motor cortex in relation to rhythmic whisking. J Neurophysiol 95:1274-1277.

Galler S, Hilber K, Pette D (1996) Force responses following stepwise length changes of rat skeletal muscle fibre types. Journal of Physiology 493:219-227.

Ganguly K, Kleinfeld D (2004) Goal-directed whisking behavior increases phase-locking between vibrissa movement and electrical activity in primary sensory cortex in rat. Proceedings of the National Academy of Sciences USA 101:12348-12353.

Gao P, Bermejo R, Zeigler HP (2001) Vibrissa deaffentation and rodent whisking patterns: Behavioral evidence for a central pattern generator. Journal of Neuroscience 21:5374-5380.

Gao P, Ploog BO, Zeigler HP (2003a) Whisking as a "voluntary" response: operant control of whisking parameters and effects of whisker denervation. Somatosensory and Motor Research 179:179-189.

Gao P, Hattox AM, Jones LM, Keller A, Zeigler HP (2003b) Whisker motor cortex ablation and whisker movement patterns. Somatosens Mot Res 20:191-198.

Gao P, Hattox AM, Jones LM, Keller A, Zeigler HP (2003c) Whisker motor cortex ablation and whisker movement patterns. Somatosensory and Motor Research 20:191-198.

Grant RA, Mitchinson B, Fox CW, Prescott TJ (2009) Active touch sensing in the rat: anticipatory and regulatory control of whisker movements during surface exploration. J Neurophysiol 101:862-874.

Grinevich V, Brecht M, Osten P (2005) Monosynaptic pathway from rat vibrissa motor cortex to facial motor neurons revealed by lentivirus-based axonal tracing. J Neurosci 25:8250-8258.

Haiss F, Schwarz C (2005a) Spatial segregation of different modes of movement control in the whisker representation of rat primary motor cortex. J Neurosci 25:1579-1587.

Haiss F, Schwarz C (2005b) Spatial segregation of different modes of movement control in the whisker representation of rat primary motor cortex. Journal of Neuroscience 25:1579-1587.

Hartmann MJ, Johnson NJ, Towal RB, Assad C (2003) Mechanical characteristics of rat vibrissae: Resonant frequencies and damping in isolated whiskers and in the awake behaving animal. Journal of Neuroscience 23:6510-6519.

Haslwanter T (2002) Mechanics of eye movements: Implications of the "orbital revolution". Annuals of the New York Academy of Sciences 956:33-41.

Hattox A, Li Y, Keller A (2003a) Serotonin regulates rhythmic whisking. Neuron 39:343-352.

Hattox AM, Priest CA, Keller A (2002) Functional circuitry involved in the regulation of whisker movements. J Comp Neurol 442:266-276.

Hattox AM, Li Y, Keller A (2003b) Serotonin regulates rhythmic whisking. Neuron 39:343-352.

Herfst LJ, Brecht M (2008) Whisker movements evoked by stimulation of single motor neurons in the facial nucleus of the rat. J Neurophysiol 99:2821-2832.

Hill DN, Bermejo R, Zeigler HP, Kleinfeld D (2008) Biomechanics of the vibrissa motor plant in rat: rhythmic whisking consists of triphasic neuromuscular activity. J Neurosci 28:3438-3455.

Hoffer ZS, Alloway KD (2001) Organization of corticostriatal projections from the vibrissal representations in the primary motor and somatosensory cortical areas of rodents. J Comp Neurol 439:87-103.

Hoffer ZS, Hoover JE, Alloway KD (2003) Sensorimotor corticocortical projections from rat barrel cortex have an anisotropic organization that facilitates integration of inputs from whiskers in the same row. J Comp Neurol 466:525-544.

Izraeli R, Porter LL (1995a) Vibrissal motor cortex in the rat: connections with the barrel field. Exp Brain Res 104:41-54.

Izraeli R, Porter LL (1995b) Vibrissal motor cortex in the rat: Connections with the barrel field. Experimental Brain Research 104:41-54.

Jin TE, Witzemann V, Brecht M (2004) Fiber types of the intrinsic whisker muscle and whisking behavior. Journal of Neuroscience 24:3386-3393.

Kamen G, Caldwell GE (1996) Physiology and interpretation of the electromyogram. Journal of Clinical Neurophysiology 13:366-384.

Khatri V, Bermejo R, Brumberg JC, Keller A, Zeigler HP (2009) Whisking in air: encoding of kinematics by trigeminal ganglion neurons in awake rats. J Neurophysiol 101:1836-1846.

Klein B, Rhoades R (1985) The representation of whisker follicle intrinsic musculature in the facial motor nucleus of the rat. Journal of Comparative Neurology 232:55-69.

Kleinfeld D, Berg RW, O'Connor SM (1999) Anatomical loops and their relation to electrical dynamics in relation to whisking by rat. Somatosensory and Motor Research 16:69-88.

Kleinfeld D, Ahissar E, Diamond ME (2006) Active sensation: Insights from the rodent vibrissa sensorimotor system. Current Opininions in Neurobiology 16:435-444.

Kleinfeld D, Sachdev RNS, Merchant LM, Jarvis MR, Ebner FF (2002) Adaptive filtering of vibrissa input in motor cortex of rat. Neuron 34:1021-1034.

Knutsen PM, Derdikman D, Ahissar E (2005) Tracking whisker and head movements in unrestrained behaving rodents. J Neurophysiol 93:2294-2301.

Knutsen PM, Pietr M, Ahissar E (2006a) Haptic object localization in the vibrissal system: Behavior and performance. Journal of Neuroscience 26:8451-8464.

Knutsen PM, Pietr M, Ahissar E (2006b) Haptic object localization in the vibrissal system: behavior and performance. J Neurosci 26:8451-8464.

Knutsen PM, Biess A, Ahissar E (2008) Vibrissal kinematics in 3D: tight coupling of azimuth, elevation, and torsion across different whisking modes. Neuron 59:35-42.

Kopell N, Ermentrout GB (1986) Symmetry and phaselocking in chains of weakly coupled oscillators. Communications on Pure and Applied Mathematics 39:623-660.

Leiser SC, Moxon KA (2006) Relationship between physiological response type (RA and SA) and vibrissal receptive field of neurons within the rat trigeminal ganglion. Journal of Neurophysiology in press.

Leiser SC, Moxon KA (2007) Responses of trigeminal ganglion neurons during natural whisking behaviors in the awake rat. Neuron 53:117-133.

Masri R, Bezdudnaya T, Trageser JC, Keller A (2008) Encoding of stimulus frequency and sensor motion in the posterior medial thalamic nucleus. J Neurophysiol 100:681-689.

Mehta SB, Whitmer D, Figueroa R, Williams BA, Kleinfeld D (2007) Active spatial perception in the vibrissa scanning sensorimotor system. PLoS Biol 5:e15.

Melzer P, Sachdev RN, Jenkinson N, Ebner FF (2006) Stimulus frequency processing in awake rat barrel cortex. Journal of Neuroscience 26:12198-12205.

Mitchinson B, Martin CJ, Grant RA, Prescott TJ (2007) Feedback control in active sensing: rat exploratory whisking is modulated by environmental contact. Proc Biol Sci 274:1035-1041.

Mitchinson B, Gurney KN, Redgrave P, Melhuish C, Pipe AG, Pearson M, Gilhespy I, Prescott TJ (2004) Empirically inspired simulated electro-mechanical model of the rat mystacial follicle-sinus complex. Proceedings of the Royal Society: Bioilogical Sciences 271:2509-2516.

Miyashita E, Keller A, Asanuma H (1994a) Input-output organization of the rat vibrissal motor cortex. Exp Brain Res 99:223-232.

Miyashita E, Keller A, Asanuma H (1994b) Input-output organization of the rat vibrissal motor cortex. Experimental Brain Research 99:223-232.

NIH (1985) Guide for the Care and Use of Laboratory Animals, Publication 85-23. Bethesda: National Institutes of Health.

O'Connor SM, Berg RW, Kleinfeld D (2002) Coherent electrical activity along vibrissa sensorimotor loops during free whisking in rat. Journal of Neurophysiology 87:2137-2148.

Percival DB, Walden AT (1993) Spectral Analysis for Physical Applications: Multitaper and Conventional Univariate Techniques. Cambridge: Cambridge University Press.

Press WH, Flannery BP, Teukolsky SA, Vetterling WT (1988) Numerical Recipies: The Art of Scientific Computing. Cambridge: Cambridge University Press.

Rice FL, Arvidsson J (1991) Central projections of primary sensory neurons innervating different parts of the vibrissae follicles and intervibrissal skin on the mystacial pad of the rat. Journal of Comparative Neurology 309:1-16.

Rice FL, A. Mance A, Munger BL (1986) A Comparative light microscopic analysis of the sensory innervatuion of the mystacial pad. I. Innervation of vibrissal follicle-sinus complexes. Journal of Comparative Neurology 252:154-174.

Rocco MM, Brumberg JC (2007) The sensorimotor slice. J Neurosci Methods 162:139-147.

Sachdev RN, Sellien H, Ebner FF (2000) Direct inhibition evoked by whisker stimulation in somatic sensory (S1) barrel field cortex of the awake rat. Journal of Neurophysiology 84:1497-1504.

Sachdev RN, Sato T, Ebner FF (2002) Divergent movement of adjacent whiskers. Journal of Neurophysiology 87:1440-1448.

Sachdev RNS, Berg RW, Champney G, Kleinfeld D, Ebner FF (2003) Unilateral vibrissa contact: Changes in amplitude but not timing of rhythmic whisking. Somatosensory and Motor Research 20:162-169.

Semba K, Komisaruk BR (1984a) Neural substrates of two different rhythmical vibrissal movements in the rat. Neuroscience 12:761-774.

Semba K, Komisaruk BR (1984b) Neural substrates of two different rhythmical vibrissal movements in the rat. Neuroscience 12:761-774.

Simons DJ, Carvell GE, Lichtenstein SH (1990) Responses of rat trigeminal ganglion neurons to movements of vibrissae in different directions. Somatosensory and Motor Research 7:47-65.

Solomon JH, Hartmann MJ (2006) Biomechanics: Robotic whiskers used to sense features. Nature 443:525.

Szwed M, Bagdasarian K, Ahissar E (2003a) Coding of vibrissal active touch. Neuron 40:621-630.

Szwed M, Bagdasarian K, Ahissar E (2003b) Encoding of vibrissal active touch. Neuron 40:621-630.

Szwed M, Bagdasarian K, Blumenfeld B, Barak O, Derdikman D, Ahissar E (2006) Responses of trigeminal ganglion neurons to the radial distance of contact during active vibrissal touch. Journal of Neurophysiology 95:791-802.

Thomson DJ (1982) Spectral estimation and harmonic analysis. Proceedings of the IEEE 70:1055-1096.

Towal RB, Hartmann MJ (2006) Right-left asymmetries in the whisking behavior of rats anticipate head movements. J Neurosci 26:8838-8846.

Travers JB, Dinardo LA, Karimnamazi H (1997) Neuroscience and Biobehavioral Reviews. Motor and premotor mechanisms of licking 21:631-647.

Urbain N, Deschenes M (2007a) A new thalamic pathway of vibrissal information modulated by the motor cortex. J Neurosci 27:12407-12412.

Urbain N, Deschenes M (2007b) Motor cortex gates vibrissal responses in a thalamocortical projection pathway. Neuron 56:714-725.

Veinante P, Deschenes M (2003) Single-cell study of motor cortex projections to the barrel field in rats. J Comp Neurol 464:98-103.

Ventakachalam S, Fee MS, Kleinfeld D (1999) Ultra-miniature headstage with 6-channel drive and vacuum-assisted micro-wire implantation for chronic recording from neocortex. Journal of Neuroscience Methods 90:37-46.

Vincent SB (1912) The function of the vibrissae in the behavior of the white rat. Behavior Monographs 1:7-81.

Voigts J, Sakmann B, Celikel T (2008) Unsupervised whisker tracking in unrestrained behaving animals. J Neurophysiol 100:504-515.

von Holst E (1954) Relations between the central nervous system and the peripheral organ.

. Br J Anim Behav 2:89-94.

Waite PME, Jacquin MF (1992) Dual innervation of the rat vibrissa: Responses of trigeminal ganglion cells projecting through deep or superficial nerves. Journal of Comparative Neurology 322:233-245.

Weiss DS, Keller A (1994) Specific patterns of intrinsic connections between representation zones in the rat motor cortex. Cereb Cortex 4:205-214.

Welker WI (1964) Analysis of sniffing of the albino rat. Behaviour 12:223-244.

Welzl H, Bures J (1977) Lick-synchronized breathing in rats. Physiological Behavior 18:751–753.

Wineski LE (1985) Facial morphology and vibrissal movement in the golden hamster. Journal of Morphology 183:199-217.

Wolfe J, Hill DN, Pahlavan S, Drew PJ, Kleinfeld D, Feldman DE (2008) Texture coding in the rat whisker system: slip-stick versus differential resonance. PLoS Biol 6:e215.

Zhang ZW, Deschenes M (1997) Intracortical axonal projections of lamina VI cells of the primary somatosensory cortex in the rat: a single-cell labeling study. J Neurosci 17:6365-6379.

Zucker E, Welker WI (1969) Coding of somatic sensory input by vibrissae neurons in the rat's trigeminal ganglion. Brain Research 12:134-156.